

**AD-A258 981**



(13)

The Pennsylvania State University  
**APPLIED RESEARCH LABORATORY**  
P.O. Box 30  
State College, PA 16804

**ESTIMATION OF THE DIRECT ACOUSTIC RADIATION  
FROM TURBULENT SPOTS, USING BOUNDARY  
LAYER VELOCITY MEASUREMENTS**

by

M. H. Krane  
W. R. Pauley

Technical Report No. TR 92-11  
November 1992

**DTIC**  
**S ELECTE D**  
**E DEC 17 1992**

Supported by:  
Office of Chief of Naval Research

L.R. Hettche, Director  
Applied Research Laboratory

Approved for public release; distribution unlimited

**92-31511**



152

**92 12 15 076**

# REPORT DOCUMENTATION PAGE

Form Approved  
OMB No. 0704-0188

Public reporting burden for this collection of information is estimated to average 1 hour per response, including the time for reviewing instructions, searching existing data sources, gathering and maintaining the data needed, and completing and reviewing the collection of information. Send comments regarding this burden estimate or any other aspect of this collection of information, including suggestions for reducing this burden, to Washington Headquarters Services, Directorate for Information Operations and Reports, 1215 Jefferson Davis Highway, Suite 1204, Arlington, VA 22202-4302, and to the Office of Management and Budget, Paperwork Reduction Project (0704-0188), Washington, DC 20503.

1. AGENCY USE ONLY (Leave blank)		2. REPORT DATE November 1992		3. REPORT TYPE AND DATES COVERED	
4. TITLE AND SUBTITLE Estimation of the Direct Acoustic Radiation From Turbulent Spots, Using Boundary Layer Velocity Measurements				5. FUNDING NUMBERS N00014-90-J-1365	
6. AUTHOR(S)  M. H. Krane, W. R. Pauley					
7. PERFORMING ORGANIZATION NAME(S) AND ADDRESS(ES) Applied Research Laboratory The Pennsylvania State University P.O. Box 30 State College, PA 16804				8. PERFORMING ORGANIZATION REPORT NUMBER  TR-92-11	
9. SPONSORING / MONITORING AGENCY NAME(S) AND ADDRESS(ES) Office of Chief of Naval Research Department of the Navy 800 North Quincy Street Arlington, VA 22217-5000				10. SPONSORING / MONITORING AGENCY REPORT NUMBER	
11. SUPPLEMENTARY NOTES					
12a. DISTRIBUTION / AVAILABILITY STATEMENT  Unlimited				12b. DISTRIBUTION CODE	
13. ABSTRACT (Maximum 200 words) To provide an understanding of the acoustic source characteristics of the boundary layer transition region, unsteady velocity field measurements of an isolated, artificially generated turbulent spot were made in a zero-pressure gradient laminar boundary layer. These measurements were performed in a water channel, using a laser-Doppler velocimeter. They provide quantitative information describing the large-scale unsteady displacement thickness fluctuations due to the passage of a turbulent spot. Fluctuations of the displacement thickness are related to the radiated noise through the Liepmann acoustic analogy. The description of the large-scale velocity field is based on ensemble-averaged unsteady velocity data, from which the displacement thickness is calculated. These results are used to calculate the velocity normal to the plate, as well as the characteristic rise times, $t_1$ , of the displacement thickness. Comparison of the results at different streamwise stations shows that the rise time and the mass flux deficit peak amplitudes of the normal velocity increase early in the spot development, but level off. For all these parameters, the rate of spatial growth is greatest in the stations closest to the generation point.					
14. SUBJECT TERMS acoustic radiation, turbulent spots, boundary layer transition region, velocity field, zero pressure gradient, displacement thickness fluctuations				15. NUMBER OF PAGES 139	
				16. PRICE CODE	
17. SECURITY CLASSIFICATION OF REPORT UNCLASSIFIED	18. SECURITY CLASSIFICATION OF THIS PAGE UNCLASSIFIED	19. SECURITY CLASSIFICATION OF ABSTRACT UNCLASSIFIED	20. LIMITATION OF ABSTRACT UNLIMITED		

## GENERAL INSTRUCTIONS FOR COMPLETING SF 298

The Report Documentation Page (RDP) is used in announcing and cataloging reports. It is important that this information be consistent with the rest of the report, particularly the cover and title page. Instructions for filling in each block of the form follow. It is important to *stay within the lines* to meet optical scanning requirements.

**Block 1. Agency Use Only (Leave blank).**

**Block 2. Report Date.** Full publication date including day, month, and year, if available (e.g. 1 Jan 88). Must cite at least the year.

**Block 3. Type of Report and Dates Covered.**

State whether report is interim, final, etc. If applicable, enter inclusive report dates (e.g. 10 Jun 87 - 30 Jun 88).

**Block 4. Title and Subtitle.** A title is taken from the part of the report that provides the most meaningful and complete information. When a report is prepared in more than one volume, repeat the primary title, add volume number, and include subtitle for the specific volume. On classified documents enter the title classification in parentheses.

**Block 5. Funding Numbers.** To include contract and grant numbers; may include program element number(s), project number(s), task number(s), and work unit number(s). Use the following labels:

C - Contract	PR - Project
G - Grant	TA - Task
PE - Program Element	WU - Work Unit Accession No.

**Block 6. Author(s).** Name(s) of person(s) responsible for writing the report, performing the research, or credited with the content of the report. If editor or compiler, this should follow the name(s).

**Block 7. Performing Organization Name(s) and Address(es).** Self-explanatory.

**Block 8. Performing Organization Report Number.** Enter the unique alphanumeric report number(s) assigned by the organization performing the report.

**Block 9. Sponsoring/Monitoring Agency Name(s) and Address(es).** Self-explanatory.

**Block 10. Sponsoring/Monitoring Agency Report Number.** (If known)

**Block 11. Supplementary Notes.** Enter information not included elsewhere such as: Prepared in cooperation with...; Trans. of...; To be published in.... When a report is revised, include a statement whether the new report supersedes or supplements the older report.

**Block 12a. Distribution/Availability Statement.**

Denotes public availability or limitations. Cite any availability to the public. Enter additional limitations or special markings in all capitals (e.g. NOFORN, REL, ITAR).

DOD - See DoDD 5230.24, "Distribution Statements on Technical Documents."

DOE - See authorities.

NASA - See Handbook NHB 2200.2.

NTIS - Leave blank.

**Block 12b. Distribution Code.**

DOD - Leave blank.

DOE - Enter DOE distribution categories from the Standard Distribution for Unclassified Scientific and Technical Reports.

NASA - Leave blank.

NTIS - Leave blank.

**Block 13. Abstract.** Include a brief (Maximum 200 words) factual summary of the most significant information contained in the report.

**Block 14. Subject Terms.** Keywords or phrases identifying major subjects in the report.

**Block 15. Number of Pages.** Enter the total number of pages.

**Block 16. Price Code.** Enter appropriate price code (NTIS only).

**Blocks 17. - 19. Security Classifications.** Self-explanatory. Enter U.S. Security Classification in accordance with U.S. Security Regulations (i.e., UNCLASSIFIED). If form contains classified information, stamp classification on the top and bottom of the page.

**Block 20. Limitation of Abstract.** This block must be completed to assign a limitation to the abstract. Enter either UL (unlimited) or SAR (same as report). An entry in this block is necessary if the abstract is to be limited. If blank, the abstract is assumed to be unlimited.

## ABSTRACT

To provide an understanding of the acoustic source characteristics of the boundary layer transition region, unsteady velocity field measurements of an isolated, artificially generated turbulent spot were made in a zero-pressure gradient laminar boundary layer. These measurements were performed in a water channel, using a laser-Doppler velocimeter. They provide quantitative information describing the large-scale unsteady displacement thickness fluctuations due to the passage of a turbulent spot. Fluctuations of the displacement thickness are related to the radiated noise through the Liepmann acoustic analogy. The description of the large-scale velocity field is based on ensemble-averaged unsteady velocity data, from which the displacement thickness is calculated. These results are used to calculate the velocity normal to the plate, as well as the characteristic rise times,  $t_r$ , of the displacement thickness. Comparison of the results at different streamwise stations shows that the rise time and the mass flux deficit peak amplitudes increase with distance from the generation point, while the peak amplitudes of the normal velocity increase early in the spot development, but level off. For all these parameters, the rate of spatial growth is greatest in the stations closest to the generation point. The normalized rise time,  $t_r U_c / \Delta x$  was found to span a range of values  $0.06 < t_r U_c / \Delta x < 0.74$  over the locations measured, where  $U_c$  is the spot convection speed and  $\Delta x$  is a transition zone length obtained from a correlation. The lowest values of this parameter were found to exist in the upstream end of the transition zone. A scaling analysis using these experimental results suggests that the sound radiated by the large-scale motion due to

an isolated turbulent spot increases as the spot grows and has a dipole character. Extrapolation to a natural transition zone indicates that sound radiation from the large-scale intermittent motion is highest in the middle part of the transition zone because the spot density is highest there. To estimate the effect of turbulent spot interaction on the sound radiation from a single spot, measurements were carried out for two turbulent spots generated at the same location with a fixed time delay. The second spot partially merged with the first at the furthest downstream station. The spot interaction was not found to alter the isolated spot results significantly.

Accession For	
NTIS CRA&I	<input checked="" type="checkbox"/>
DTIC TAB	<input type="checkbox"/>
Unannounced	<input type="checkbox"/>
Justification .....	
By .....	
Distribution /	
Availability Codes	
Dist	Avail and/or Special
A-1	

ALL INFORMATION CONTAINED HEREIN IS UNCLASSIFIED

## TABLE OF CONTENTS

LIST OF FIGURES . . . . .	vii
LIST OF TABLES . . . . .	x
NOMENCLATURE . . . . .	xi
 CHAPTER 1 INTRODUCTION . . . . .	 1
1.1 OVERVIEW . . . . .	1
1.2 BOUNDARY LAYER TRANSITION FLOWS . . . . .	3
1.3. ACOUSTICS OF BOUNDARY LAYER TRANSITION . . . . .	8
1.4 PROJECT GOALS . . . . .	15
 CHAPTER 2 ANALYTICAL FOUNDATIONS . . . . .	 18
2.1 THE ACOUSTIC BOUNDARY VALUE PROBLEM . . . . .	19
2.2 BOUNDARY CONDITION FOR ACOUSTIC EQUATION . . . . .	24
2.2.1 The Displacement Thickness . . . . .	24
2.2.2 Calculating Normal Velocity from the Displacement Thickness . . . . .	26
2.2.3 Transfer of the Boundary Condition to the Wall . . . . .	30
2.3 BOUNDARY CONDITION FOR A TURBULENT SPOT . . . . .	31
 CHAPTER 3 EXPERIMENTAL APPARATUS . . . . .	 36
3.1 WATER CHANNEL FACILITY . . . . .	36
3.1.1 Test Section . . . . .	38
3.1.1.1 Floor and Walls . . . . .	38
3.1.1.2 Flat Plate Test Model . . . . .	39
3.1.1.3 First and Second Corners . . . . .	41
3.1.2 Pump . . . . .	41
3.1.3 Return Leg . . . . .	43
3.2 DATA ACQUISITION . . . . .	51
3.2.1 Laser Doppler Velocimeter . . . . .	51
3.2.2 Data Acquisition . . . . .	53
3.3 SPOT GENERATOR . . . . .	59
3.4 WATER CHANNEL QUALIFICATION . . . . .	61
3.4.1 Water Quality . . . . .	61
3.4.2 Baseline Flow . . . . .	62
3.4.3 Suggested Improvements . . . . .	62

<b>CHAPTER 4 EXPERIMENTAL RESULTS AND DISCUSSION</b>	<b>68</b>
4.1 EXPERIMENTAL CONDITIONS AND DATA PROCESSING	68
4.1.1 Experimental Plan	68
4.1.2 Data Processing	73
4.2 SINGLE SPOT MEASUREMENTS	74
4.2.1 Spot Growth	74
4.2.2 Unsteady Mass Flux Deficit, Normal Velocity	77
4.2.3 Rise Time Estimates	95
4.3 INTERACTING SPOT MEASUREMENTS	100
4.3.1 Unsteady Mass Flux Deficit, Normal Velocity	100
4.3.2 Rise Time Estimates	104
<b>CHAPTER 5 ESTIMATION OF SOUND RADIATION</b>	<b>108</b>
5.1 SOUND RADIATION FROM AN ISOLATED TURBULENT SPOT	108
5.2 INTERMITTENCY-WEIGHTING OF DISPLACEMENT THICKNESS	113
5.3 NOISE FROM A NATURAL BOUNDARY LAYER TRANSITION	116
<b>CHAPTER 6 CONCLUSIONS</b>	<b>122</b>
6.1 DISCUSSION	122
6.2 SUMMARY	127
6.3 SUGGESTIONS FOR FURTHER WORK	128
<b>REFERENCES</b>	<b>131</b>

## LIST OF FIGURES

Figure 1.1	Basic source types . . . . .	12
Figure 2.1	Geometry of the acoustic boundary value problem. . . . .	21
Figure 2.2	Intermittency-weighted form of unsteady displacement thickness . . . . .	34
Figure 3.1	Water Channel Facility . . . . .	37
Figure 3.2	Flat plate test model. . . . .	40
Figure 3.3	Detail of water channel pump. . . . .	42
Figure 3.4	Detail showing propeller shaft feedthrough and how it is sealed. . . . .	44
Figure 3.5	Detail of the compound diffuser . . . . .	48
Figure 3.6	Diffuser source-point displacement (Feil, 1964) . . . . .	48
Figure 3.7	Schematic of filtration inlet/outlet . . . . .	49
Figure 3.8	Schematic of LDA setup . . . . .	52
Figure 3.9	Convergence of the ensemble average. . . . .	56
Figure 3.10	Ensemble mean and variance of streamwise component of velocity at $x=1.53\text{m}$ , $y=0.8\text{ mm}$ , $z=0\text{ m}$ , $U=40.6\text{ cm/s}$ . . . . .	57
Figure 3.11	Spot generator disturbance signature . . . . .	60
Figure 3.12	Boundary layer profiles in similarity coordinates . . . . .	63
Figure 3.13	Schematic of test plate flow regimes, showing the sidewall contamination. . . . .	64
Figure 3.14	Position of intersection of sidewall contamination wedges . . . . .	65



Figure 4.1	Top view of locations for unsteady velocity measurements . . . . .	69
Figure 4.2	Turbulent spot envelope in similarity coordinates . . . . .	76
Figure 4.3	Mass flux deficit and normal velocity fluctuations . . . . .	78
Figure 4.4	Spanwise distribution of mass flux deficit at $x=1.13$ m . . . . .	79
Figure 4.5	Mass flux deficit and normal velocity ( $v_n$ ) fluctuations . . . . .	82
Figure 4.6	Comparison of velocity perturbation contours with mass flux deficit time series, $x=1.13$ m. . . . .	83
Figure 4.7	Comparison of normal velocity . . . . .	86
Figure 4.8	Contour plot of perturbation velocity . . . . .	87
Figure 4.9	Contour plot of $v_p$ at $x=1.13$ m, $U=40.6$ cm/s . . . . .	88
Figure 4.10	Contour plot of $v_p$ for $x=1.53$ m, $U=40.6$ cm/s . . . . .	89
Figure 4.11	Streamwise variation of unsteady mass flux deficit . . . . .	91
Figure 4.12	Peak values of $\Delta MFD/\rho U_\infty$ shown in Fig. 7 . . . . .	92
Figure 4.13	Celerity diagram for $MFD/\rho U$ shown in Fig. 7 . . . . .	94
Figure 4.14	Streamwise variation of peak values of $v_n$ . . . . .	96
Figure 4.15	Nondimensional rise time . . . . .	98
Figure 4.16	Streamwise variation of unsteady $\Delta MFD/\rho U$ for interacting spots . . . . .	101
Figure 4.17	Comparison of the velocity field inside the interacting turbulent spots . . . . .	102
Figure 4.18	Comparison of velocity traces with mass flux for interacting spots . . . . .	103

Figure 4.20	Celerity diagrams for interacting spot cases . . . . .	105
Figure 4.20	Nondimensionalized rise times for the interacting spot case . . .	106
Figure 5.1	Spatial distribution of instantaneous $v_x$ . . . . .	110
Figure 5.2	Order of magnitude estimates of the radiated pressure . . . . .	114
Figure 5.3	Comparison of measured $MFD/\rho U_\infty$ and intermittency-weighted $\delta^+(t)$ assumed by Lauchle (1981) . . . . .	115
Figure 5.4	Extrapolation of single spot radiation estimate to natural transition zone . . . . .	120

**LIST OF TABLES**

<b>Table 4.1</b>	<b>List of isolated spot u-profile experiments. . . . .</b>	<b>70</b>
<b>Table 4.2</b>	<b>List of isolated spot direct normal velocity measurements. . . . .</b>	<b>71</b>
<b>Table 4.3</b>	<b>List of interacting spot u-profile measurements. . . . .</b>	<b>72</b>

# **NOMENCLATURE**

<b>c</b>	speed of sound, m/s
<b>C,n</b>	constants used in transition zone length correlation
<b>D</b>	dipole strength per unit area, Pa/m <sup>2</sup>
<b>H</b>	height of measured boundary layer profiles, m
<b>I(x,t)</b>	Libby's indicator function
<b>M</b>	Mach number
<b>MFD</b>	mass flux deficit, kg/s
<b>N</b>	turbulent spot passage rate (Hz)
<b><math>\hat{N}</math></b>	turbulent spot density $\sim N/U$ (1/m)
<b>p</b>	pressure, Pa
<b>p<sub>d</sub></b>	dipole radiated pressure, Pa
<b><math>\mathcal{P}</math></b>	acoustic power, W
<b>Q</b>	simple source strength, kg/s
<b>r</b>	$=  \mathbf{x}' - \mathbf{x} $ , distance from source point to observer
<b>R</b>	radius describing size of $V \cup V_0$
<b>Re<sub>x</sub></b>	Reynolds number based on length scale x
<b>S</b>	surface bounding V at distance R from origin
<b>S<sub>0</sub></b>	surface above boundary layer on which boundary condition for the Liepmann analogy is defined
<b>t</b>	time coordinate, s

$t_i$	characteristic time of displacement thickness fluctuation, s
$t^+, t^-$	time for MFD to rise from 0 to maximum (+) and fall from its maximum to minimum (-)
$T$	non-dimensionalized rise time, $t_i U_c / \Delta x$
$u, v, w$	velocity components in the x, y, z directions, respectively, m/s
$u_i$	undisturbed laminar flow velocity, m/s
$u_p$	$= u(x, y, z, t) - u_i$ , m/s
$U_c$	turbulent spot convection speed, m/s
$U$	freestream velocity, m/s
$V$	volume containing inviscid portion of flow, where acoustic equation holds
$V_\theta$	volume containing boundary layer (acoustic source region)
$v_n$	normal velocity fluctuation, m/s
$v_p$	potential flow velocity perturbation normal to the wall, m/s
$x_{tr}$	x-coordinate at which sidewall contamination wedges merge, m
$x, y, z$	streamwise, normal, and spanwise coordinates, respectively
$x_0, y_0, z_0$	coordinates of spot generation point, m
$\beta_i, \beta_j$	directivity factors
$\gamma$	intermittency parameter
$\delta$	boundary layer thickness, m
$\delta^*$	boundary layer displacement thickness, m

$\Delta\delta^*$	$= \Delta\delta_T^* - \Delta\delta_L^*$
$\Delta\text{MFD}/\rho U$	instantaneous MFD/ $\rho U$ minus undisturbed displacement thickness
$\Delta x$	transition zone length
$\epsilon$	source separation in spot source model
$\nu$	kinematic viscosity, $\text{m}^2/\text{s}$
$\zeta$	non-dimensional streamwise coordinate measured from the beginning of the transition zone
$\eta, \xi$	similarity coordinates
$\rho$	fluid density, $\text{kg}/\text{m}^3$
$\phi$	acoustic potential, $\text{m}^2/\text{s}$

# **CHAPTER 1**

## **INTRODUCTION**

### **1.1 OVERVIEW**

Although the production of sound by unsteady fluid motion has been a topic of interest for nearly four decades, the pioneering work of Lighthill (1952, 1954) remains the point of reference for much of our current understanding of the subject. The focus of Lighthill's early work in this area was the production of sound by jets. He was motivated by the needs of jet propulsion which was in its early stages. It was realized that the presence of solid bodies could substantially alter, even increase, the aerodynamic production of sound (see, *e.g.*, Curle, 1955). Sound generated by a flow interacting with a solid surface may be classified into two categories according to how the flow unsteadiness is generated. If the dominant noise generation mechanism is unsteady flow impinging on a solid body, the sound produced is referred to as "interaction noise." This type of noise production occurs when helicopter blades interact with the blade-tip vortices that they generate and in a jet engine compressor stage due to rotor/stator interaction. When the unsteady flow responsible for the sound production results from viscous action at a solid body it is called "self-noise." Examples include sound from a turbulent boundary layer on a wall or from the wake of a circular cylinder.

Another example of "self-noise" is the noise produced by a boundary layer undergoing transition from laminar to turbulent flow. The principle noise generation is thought to occur in the "intermittent region," where the final stage of the transition

between laminar and turbulent flow causes large fluctuations in the velocity and pressure fields. Not only are these fluctuations large, but they are thought to occur such that the flow is an efficient acoustic radiator (Lauchle, 1981, 1989; Sornette and Lagier, 1984a, b; Lagier and Sornette, 1986; and Audet *et al.* 1989a, b). Lauchle (1981), Sornette and Lagier (1984a, b), Lagier and Sornette (1986), and Audet *et al.* (1989) predicted a monopole type source. Lauchle (1989) showed later, using scaling arguments, that a naturally transitioning boundary layer radiates sound power proportional to  $U^{7.5}$ , only slightly more efficiently than a fully turbulent boundary layer. In flows of low Mach number, a monopole source is the most efficient at radiating sound and would therefore be expected to dominate the generated sound field. If boundary layer transition is an efficient sound source, the importance to the silencing of underwater vehicles is immediately apparent.

There is some experimental evidence which suggests the predominance of transition as a noise source. Perraud (1989) conducted measurements of wall pressure on a body of revolution in a wind tunnel. By placing wall-mounted microphones in the laminar portion of the boundary layer upstream of the transition region and by using conditional sampling triggered on spot arrivals at a downstream location he showed that the spots did radiate sound at appreciable levels. Perraud further showed that the limits set by Lauchle (1981) for the sound spectral levels bounded his own wall-pressure spectra. Attempts to repeat these experiments in a water towing tank were unsuccessful because of the mechanical noise from the towing mechanism.



Audet *et al.* (1989a, b) also demonstrated that transitional flow is an appreciable noise source. This work was a combined analytical/experimental study. Using a model based on the previous work of Sornette and Lagier (1984a, b) and Lagier and Sornette (1986), they clearly separated the wall pressure fluctuations into contributions due to (1) the effect of the turbulence in the turbulent spots and (2) the radiated sound caused by the large-scale fluctuations in the boundary layer flowfield. The analysis showed an appreciable contribution to the wall-pressure due to pressure fluctuations in the acoustic wavenumber domain. The confirmation of these results consisted of wall-pressure measurements in a transitional boundary layer which were corrected for the spatial filtering effects of the microphone size. These corrected RMS pressure measurements were shown to give good agreement with the sum of the contributions of the two parts of the wall-pressure, the acoustic contribution due to the intermittency, and the intermittency-weighted turbulent source.

## **1.2 BOUNDARY LAYER TRANSITION FLOWS**

A full description of the noise from a naturally occurring boundary layer transition requires a knowledge of the transition flowfield. Since this process is to some extent a "random" one, its description is generally given in statistical terms. A laminar boundary layer may undergo a transition to turbulent flow by many routes. The classical scenario begins with the laminar boundary layer exhibiting two-dimensional viscous Tollmien-Schlichting instability waves that grow exponentially

from their inception. This instability mode itself becomes unstable and is susceptible to disturbances with spanwise nonuniformity and thus it begins to develop a spanwise waviness. Up to this point the energy contained in the instability wave fluctuations is only a very small fraction of the total flow energy. The three-dimensional instability waves then interact to form local high-shear regions which cause the laminar flow to break down rapidly into turbulence. As these localized regions of turbulence, or turbulent spots, convect downstream, they grow by destabilizing the surrounding laminar boundary layer (Gad-el-Hak, *et al.*, 1981), causing it to become turbulent at the edges of the spot. The spots grow until they merge with each other and a turbulent boundary layer is formed. The streamwise extent of this region is small compared to the other regions of the flow.

The transition process need not proceed by this path, however. The process described above is based on the behavior of an unstable laminar boundary layer, driven by a low-turbulence outer flow, in the presence of infinitesimal disturbances. If the freestream turbulence level is high, or if there is some large disturbance to the boundary layer, then the early stages of transition may be bypassed. An example is a laminar boundary layer separation in which the laminar shear layer becomes turbulent before re-attaching to the body. A boundary layer subjected to an extreme adverse pressure gradient may also bypass the earlier stages of transition, even without separation.

By whatever means the final stage of transition is reached, it is characterized by its intermittent nature. Early studies of the transition zone (Dhawan and

Narasimha, 1958) characterized it as a region alternating locally between a fully-turbulent and a fully-laminar structure. By defining an intermittency parameter,  $\gamma$ , as the percentage of the time that the flow at a given point is turbulent, the time-averaged velocity profile and its integral parameters, such as displacement thickness, may be described using an intermittency-weighted form:

$$\bar{\delta}^*(x) = (1 - \gamma(x))\delta^*_L(x) + \gamma(x)\delta^*(x)_T, \quad (1.1)$$

where  $\delta^*_L$  is the fully-laminar (Blasius) displacement thickness and  $\delta^*_T$  is the fully turbulent time-averaged displacement thickness. The intermittency parameter has been shown to represent adequately the average properties of the flowfield for a zero-pressure gradient boundary layer transition. For flows with a significant pressure gradient, there does not appear to be such a universal scaling parameter (Narasimha, *et al.*, 1984).

The intermittent nature of the flow is shown in the ensemble-averaged velocity profile measurements of Wygnanski *et al.* (1976). The averaged profile is laminar upstream of the spot, but as the spot passes by, the near-wall regions of the flow undergo a rapid acceleration, and then a deceleration, corresponding to a change from a laminar velocity profile to a turbulent profile and back again. This event is accompanied by an injection of high-momentum fluid from the freestream, followed by an ejection of the low-momentum fluid from near the wall as the flowfield returns to its laminar state. The final return to the initial laminar state proceeds very slowly

and is characterized by a laminar "calming region" (Schubauer and Klebanoff, 1955).

The alternating appearance of laminar and turbulent flow causes velocity fluctuations normal to the plate which are larger in magnitude than those occurring in a fully turbulent layer.

The large-scale motion exhibited by an ensemble-averaged representation of the spot initially led some to view the spot as a large, arrowhead-shaped vortex tube (Coles and Barker, 1975; Cantwell *et al.*, 1978). This was shown to be an oversimplification by the flow visualization studies of Cantwell *et al.* (1978); Matsui (1980); Gad-el-Hak *et al.* (1981); and Perry *et al.* (1981), which indicated that no such large-scale structures existed -- instead, the spot is composed of small structures not unlike those found in a fully turbulent boundary layer. Later investigations (see, *e.g.*, Wygnanski *et al.*, 1981; Sankaran *et al.*, 1991) demonstrated that the ensemble averaged flowfield is a somewhat misleading representation of the unsteady flow in a turbulent spot. However, Van Atta *et al.* (1982) showed that the potential flow velocity responds to a spot passage as it would to a "bump" in a wall described by  $y = \delta^*(x, t)$ , where  $\delta^*$  is the local displacement thickness found from the ensemble-averaged unsteady velocity field. Furthermore, the scaling results obtained from an ensemble-averaged velocity field do provide accurate measurements of the overall scales of the spot such as the streamwise, spanwise, and normal growth rates, as well as the convection velocity of the spot (Sankaran, *et al.*, 1991). Thus, although the ensemble-averaged description of the velocity field is somewhat misleading in

describing the details of the boundary layer flow, it may be used to predict the effect of the unsteady boundary layer on the potential flow.

The displacement effect is an important one in considering sound generated by a viscous flow (Liepmann, 1954). It is well known that the effect of a boundary layer on the surrounding potential flow is equivalent to an inviscid flow over a wall of height equal to  $\delta^*$ . The displacement thickness is an integral parameter expressing the amount of mass flux lost to an incoming stream due to the presence of the boundary layer. The mass flux lost to the incoming stream may be directed either in the spanwise direction or away from the solid surface. Another important consideration is the range of temporal and spatial scales of the unsteady flow. In a naturally-occurring transition there are three length scales. The first is the characteristic size of the turbulent eddies of which the turbulent spots are composed. The next level is the size of the spots themselves. Lastly, there is the streamwise extent of the entire transition zone. Similarly, temporal scales exist at these same levels: the time for a turbulent eddy to pass a given location, the passage time for a turbulent spot, and the time between spot passages. The transition zone involves a range of scales that are larger than those found in a fully turbulent boundary layer. These scales can provide order-of-magnitude estimates for the frequencies of the sound that will be present in the farfield.

### 1.3. ACOUSTICS OF BOUNDARY LAYER TRANSITION

Given that any unsteady flow has the potential to cause sound generation, it is apparent that the various transitional flow structures are possible sources. The important distinction between the transitional and fully turbulent portions of the flow is that the transitional regimes are characterized by boundaries between the laminar (steady) and turbulent (unsteady) regions of the boundary layer. Because the volume of the unsteady regions grows as they convect downstream, the acoustic "source volume" increases with time. In the intermittent region, then, there is not only the mechanism by which a fully turbulent layer would radiate sound, but also an additional effect due to the localization and growth of the turbulent regions (Lauchle, 1980, 1981; Lagier and Sornette, 1984a, 1984b, 1986).

The problem of noise from a transitioning boundary layer did not receive much attention until the early 1980s. Most of the work on boundary layer noise has dealt with radiation from fully turbulent boundary layers. Sound radiation from a boundary layer was studied by Phillips (1955) and Powell (1960). Most of this early work used Curle's (1955) extension of Lighthill's (1952, 1954) analysis to include the effects of solid bodies. Specifically, it dealt with how to describe the acoustic sources in terms of distributions both of quadrupoles due to unsteady normal stresses in the boundary layer and of dipoles due to unsteady forces at the solid wall.

For a large plate ("large" being defined as the length scale of the plate being much larger than the acoustic wavelength of interest) Powell (1960) showed that the effect of the solid wall was to reflect the sources in the flow. He treated this

reflection by replacing the wall with a set of sources of equal strength but positioned so that there is a symmetry between a source and its opposite virtual number. The net effect of this reflection is that lateral quadrupoles become octupoles, longitudinal quadrupoles double in strength, and surface dipoles become quadrupoles. Based on this analysis the radiation from a turbulent boundary layer should have at most quadrupolar radiation characteristics.

The classification of aeroacoustic sources into monopoles, dipoles, etc., is useful if handled with care (Powell, 1990). If such a division of sources is meaningful, it can provide a straightforward means of ranking source mechanisms in terms of their efficiency, especially for flows at low Mach number. The efficiency of a compact monopole scales with Mach number, a dipole with Mach number cubed, a quadrupole with Mach number to the fifth power. For underwater flows this is especially useful, since the Mach number seldom goes above 0.01. This explains why so much effort has been expended in determining how the dipoles due to wall pressure fluctuations manifest themselves in turbulent boundary layer noise [see, *e.g.*, Phillips (1955); Tam (1975); and Hardin (1991)]. If wall pressure fluctuations behave as dipole sources, they would dominate the radiation field of a low Mach number flow and attention can be focussed on that particular mechanism.

Tam (1975) used a different approach to the study of turbulent boundary layer noise. Using an empirical wall-pressure spectrum developed by Maestrello (1965, 1967) he estimated the pressure fluctuations on a plane parallel to the flat plate, but just above the boundary layer. The pressure on this surface was then related to the

pressure at a point in the farfield using the method of stationary phase. This approach allowed Tam to show that the portion of the source spectrum that radiates sound is that for which the wavenumber components have supersonic phase speeds. Continuing this approach, Hardin (1991) demonstrated that localized structures are more likely to produce this kind of spectrum, precisely because of their localization in space. From this type of argument Hardin went on to hypothesize that in a turbulent boundary layer horseshoe vortices are the primary source of sound radiation.

Liepmann (1954) [see also Laufer *et al.*(1964)] had already anticipated such an approach. His particular method consisted of relating the radiation from a boundary layer to fluctuations in the velocity normal to the solid surface, which may be deduced by measuring the boundary layer displacement thickness,  $\delta^*$ .

If the boundary layer is unsteady, then it is expected that the mass flux normal to the wall is also unsteady and that these fluctuations give rise to sound radiation if they contain frequency components that possess supersonic phase speeds. The acoustic problem is then solved by specifying the behavior of the displacement thickness fluctuations from the known boundary layer velocity field and using the deduced normal velocity distribution as a boundary condition for the acoustic wave equation.

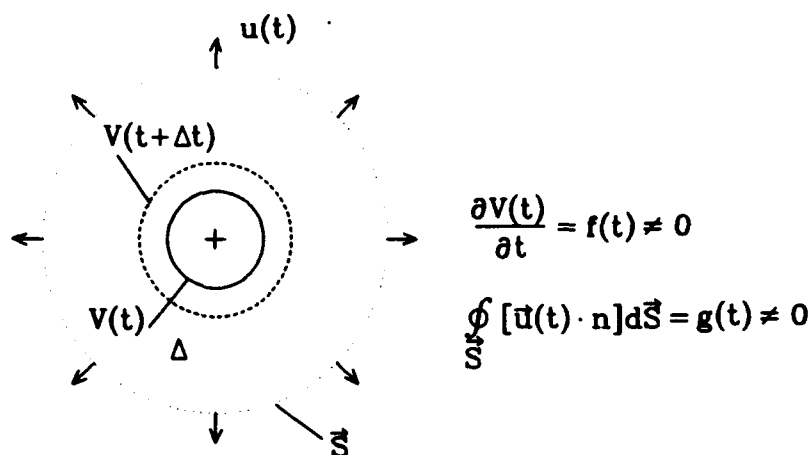
This situation is similar to the flow over a wavy wall of height  $y=\delta^*$ , as described by Van Atta *et al.*(1982). The radiation from a compact flow over a compact surface is given by Crighton (1975). The dominant source is a monopole caused by the rate of change at which the volume of fluid is displaced by the wall.



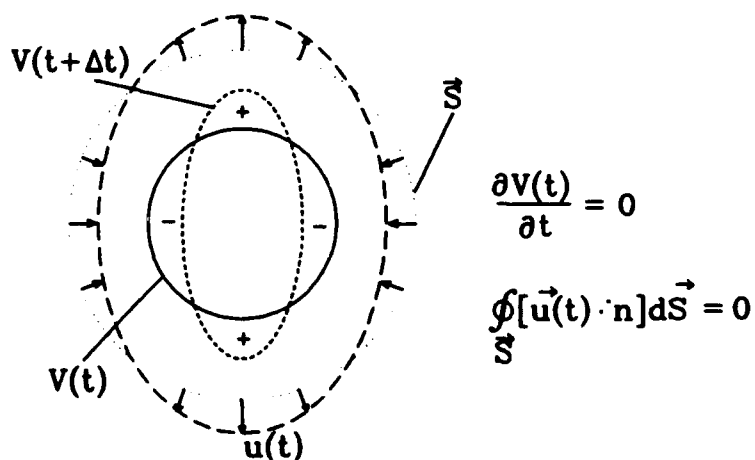
Crighton (1975) points out, however, that this source mechanism exists only if there is a net unsteady mass flux over the entire surface. If there is mass flux away from the wall in one location, but an equal amount towards the plate in another location, there is no net mass flux and there is no monopole radiation field as long as the positive and negative peaks are in close enough proximity to be considered a compact source distribution.

A physical system which behaves like a monopole is a sphere that undergoes spherically symmetric oscillations of its size, i.e., the motion of its surface is only radial (see Figure 1.1a). The sphere displaces the fluid uniformly in an amount equal to the rate of change of its volume. In addition, there is a net mass flux in the radial direction at any given time when the sphere is either expanding or contracting. For higher order sources the instantaneous net mass flux normal to the surface is identically zero. For example, a sphere whose surface deforms in a non-axially symmetric manner, but whose volume is conserved (see Figure 1.1b), radiates like a quadrupole. While the spatial distribution of the sphere's volume changes with time, the total volume does not. These non-symmetric spatial variations cause phase cancellations of the pressure which lead to a lower radiation efficiency. A boundary layer will produce monopole radiation if the volume, whose bounding surfaces are the solid wall and the surface  $y = \delta^*(x,t)$ , changes with time.

The Liepmann approach has not received as much attention as those based on a Lighthill formulation. Lauchle (1981), however, used the Liepmann analogy to describe the radiation from the intermittent zone of a flat plate boundary layer. He



(a) Small radially oscillating sphere models a monopole. A monopole is distinguished by a net volume displacement, reflected in a nonzero unsteady mass flux normal to the surface  $S$  surrounding the sphere.



(b) A quadrupole may be modelled by a sphere undergoing elliptical distortions. The quadrupole is distinguished by its conservation of volume, reflected in the constant zero net mass flux in the radial direction.

**Figure 1.1** Basic source types and their normal mass flux distributions.

hypothesized that the rapid fluctuations in displacement thickness at the edges of turbulent spots, which could be characterized by a time scale  $t_i$ , were a weak monopole source mechanism. Lacking information regarding the behavior of these fluctuations, he wrote an expression for the assumed behavior using a conditioned-signal approach (Libby, 1975) and assumed an intermittency-weighted form for the unsteady displacement thickness. Lauchle (1981) estimated the radiation intensity (power per unit area) and found it to be significantly greater than that radiated from a fully turbulent boundary layer covering the same surface area. He also found that the high frequency portions and peak values of the calculated farfield spectra were very sensitive to the value of  $t_i$ .

Later work by Lauchle (1989) modified his earlier conclusions and indicated that the intermittent flow is a monopole type source only for low frequencies. Another way to state this is that the source is no longer compact at high frequencies and as a result a classical aeroacoustics treatment does not necessarily apply. As stated above, a boundary layer producing monopole-like radiation will exhibit the following behavior: (1) the volume bounded by  $y=\delta^*$  and  $y=0$  should change with time and (2) the unsteady net mass flux normal to the wall is not identically zero. These requirements imply either that turbulent spots must grow in size or that the number of spots must increase in the downstream direction in order to radiate noise. Therefore, the monopole nature of the source may be determined by specifying the behavior of the unsteady mass flux normal to the wall as a function of position in the

intermittent region. If the normal mass flux is both unsteady and nonzero then a monopole does exist for low frequencies.

Another approach to the analysis of transition noise was that of Lagier and Sornette (1984a, 1984b, 1986). They hypothesized that in intermittent flows such as boundary layer transition, the transients caused by the intermittency would lead to an efficient source generation mechanism. This analysis proceeded by making use of an intermittency-weighted form of the Lighthill acoustic analogy. The intermittency-weighting assumption was justified by considering the transition region to be a mixture of two fluids, one laminar and one turbulent. The form of the acoustic source for boundary layer transition determined in this manner was found to include the large-scale noise source modeled by Lauchle (1981). This leading term was interpreted to be a monopole caused by the growth of the turbulent "phase" of the flow at the expense of the laminar "phase." The equivalence between the results of the two approaches is shown explicitly by Audet *et al.* (1989a, 1989b).

Previous analyses of the acoustic generation mechanisms have thus relied on assumptions concerning the behavior of the boundary layer flowfield. The present work is intended to supply measurements of the unsteady velocity field present in the principle feature of transition, the turbulent spot. From this data the time scale  $\tau$  and the acoustic source strength for a turbulent spot is estimated. A discussion of the implications of the measured flowfield behavior for existing models of transition noise, *e.g.*, the ranking of the source behavior in terms of monopoles, dipoles, *etc.*,

is also presented. Finally, the data is used to provide estimates of the sound radiated from a turbulent spot and to evaluate the assumptions of previous investigators.

#### **1.4 PROJECT GOALS**

The fluid mechanics issues that must be addressed in order to further the understanding of transition noise are:

1. The proper form for the displacement thickness fluctuation and its relation to the normal velocity derivative fluctuation.
2. The value of the time scale,  $t_i$ , and its variation with position.
3. The growth rate of the volume of sound-producing fluid (i.e., of the turbulent spot) and its variation with position.
4. The degree of attenuation of these parameters due to interaction between turbulent spots.

These questions have an important bearing on the relevant acoustics issues:

1. The radiation characteristics of a turbulent spot at different stages of its development.
2. The effect of the form of the displacement thickness fluctuation on the sound radiation estimate. Here the interest is in what effect the simplifying assumptions of Lauchle (1981) and Sornette and Lagier (1984) have on estimation of the sound.
3. The effect of spot interaction, which occurs in an actual natural transitional flow, on the sound produced by an individual turbulent spot.

In order to answer these questions the following investigation has been performed. A turbulent spot was generated in a laminar flat plate boundary layer by a vigorous impulsive mass injection from a small hole. Measurements were taken of the velocity field fluctuation caused by the passage of the spot for a freestream velocity  $U = 41$  cm/s. Specifically, measurements were made of the unsteady streamwise velocity profiles, both on and off the spot centerline, at five streamwise locations in the boundary layer. From these measurements the boundaries of the turbulent spot and its growth rates were determined. Using conservation of mass the local rate of change of mass flux over the span was also deduced. The rise time,  $t_r$ , was then determined using the local rate of change of the streamwise mass flux. The normal velocity at a location just above the maximum spot height was also measured directly for comparison with the integral analysis. This data set, then, provides information concerning the ensemble-averaged unsteady velocity profile over a significant portion of the development of the turbulent spot, along with the map of the potential flow perturbation velocity normal to the wall, for one set of conditions in one facility. Such a complete and consistent description of the flow quantities needed for the Liepmann acoustic analogy is not available in any previous experimental investigation of turbulent spots.

The effect of turbulent spot interaction on the spot growth rates was determined next. This was accomplished by generating a second spot at a given delay time after the first. The streamwise profiles on the centerline were measured in order to deduce the same streamwise growth parameters as in the baseline case. In addition,

the normal velocity was measured to obtain the normal mass flux distribution. These measurements, combined with the single spot case, allowed an assessment of the attenuation of the growth rates of a spot due to the presence of another spot.

Finally, the sound radiation from a turbulent spot was estimated. The behavior of the normal velocity seen in the measurements enabled the normal mass flux distribution of a turbulent spot to be described by a superposition of simple sources. This arrangement in turn led to a scaling analysis of the turbulent spot sound radiation. This analysis was used in conjunction with the experimental data to estimate how the spot generates sound as it grows. Using some simple assumptions, these results were then extended to the natural transition case.

## **CHAPTER 2**

### **ANALYTICAL FOUNDATIONS**

In order to estimate the sound radiated from a boundary layer flow, it is necessary to relate the farfield pressure radiation to motions which occur in the boundary layer. Information about the unsteady fluid motion in the boundary layer may be derived either from calculation or from experimental data. The relationship between the source and its effect on the farfield has been presented in two ways, the approach of Lighthill (1952) and the approach of Liepmann (1954). Lighthill (1952) treated the second derivatives of the fluctuating Reynolds stresses as quadrupole sources in the wave equation for the acoustic radiation (see Phillips (1955), Powell (1960), Hardin (1991)). This information is not easily accessible experimentally because it requires measurement of the second derivatives of second and higher order fluctuating velocity products simultaneously over the entire source field.

An alternative, but seldom used, approach is that of Liepmann (1954), which treats the potential flow fluctuations directly above the boundary layer as a boundary condition to the wave equation. A similar approach was later used by Tam (1975) to analyze the sound radiated from a turbulent boundary layer. Potential flow fluctuations may be derived from fluctuations in the boundary layer displacement thickness. Using concepts from slender body theory, a boundary condition for the acoustic wave equation may be constructed from the known unsteady displacement thickness behavior. It will be shown in this chapter that while the form for the farfield pressure is conveniently written in terms of the displacement thickness,



calculation of the displacement thickness from three-dimensional, unsteady velocity field data is not straightforward. This problem has motivated the use of a related quantity, the mass flux deficit. In this work, the unsteady boundary condition for the wave equation is constructed using the unsteady mass flux deficit obtained from the experimental data.

For a transitional boundary layer the intermittent nature of the source flow presents a situation where the Liepmann approach has advantages over that of Lighthill for predicting flow noise. The distinct changes in the flowfield which take place during the passage of a turbulent spot allow the large-scale fluctuations of the displacement thickness to be expressed in a simple form. This form of the unsteady displacement thickness includes parameters which may be derived from experimental data.

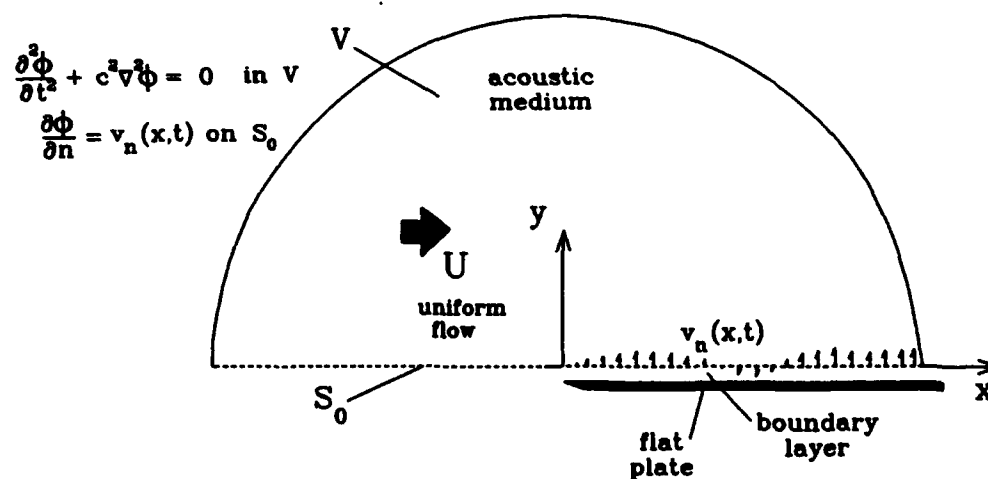
## 2.1 THE ACOUSTIC BOUNDARY VALUE PROBLEM

The physical system investigated here was a uniformly moving, viscous fluid flowing over a flat plate with a uniform velocity  $U \ll c$ , where  $c$  is the speed of sound for the fluid which is uniform throughout (see Figure 2.1a). The origin of the coordinate system is at the leading edge of the flat plate. In the region of the fluid near to the wall a laminar boundary layer is formed. A turbulent spot is generated by a point impulsive disturbance at a location  $x=x_0$ ,  $y=0$ ,  $z=0$  ( $z=0$  is subsequently referred to as the centerline). The acoustic source region is the portion of the boundary layer which is unsteady due to the presence of the turbulent spot. For

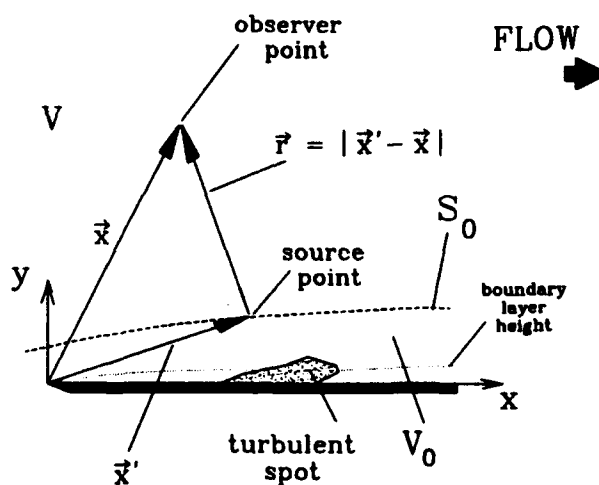
purposes of analysis the fluid region is divided into two portions, denoted  $V$  and  $V_0$ , as shown in Figures 2.1a and 2.1b. The inviscid part of the flow, denoted by  $V$ , is bounded on one side by the hemispherical surface  $S$  located at a radius  $R \gg \delta$ , and on the other by the surface  $S_0$ , which is located outside the boundary layer, *i.e.*,  $y > \delta(x, z, t)$ , where  $\delta$  is the boundary layer thickness. The viscous flow region,  $V_0$ , is the boundary layer itself, bounded by the surfaces  $y = 0$  and  $S_0$ . The radiation of sound from the boundary layer is determined by relating the "nearfield" disturbances on  $S_0$  to a farfield point in  $V$  through the wave equation. Experimental measurements inside  $V_0$  provide the information for constructing the boundary condition on  $S_0$ . The positions of an observer in  $V$  and a source point on  $S_0$  are denoted by  $x$  and  $x'$ , respectively, while the distance from a source point to an observer,  $r = |x' - x|$ , is the magnitude of the vector  $r = x' - x$ , as shown in Figure 2.1b.

For an observer anywhere in  $V$ , but far enough away from the boundary layer, the sound generated by the turbulent spot is described by the acoustic wave equation which has been linearized about the steady flow :

$$\frac{\partial^2 \phi}{\partial t^2} - c^2 \nabla^2 \phi = 0 \quad \text{in } V \quad (2.1)$$



(a) Geometry of the acoustic boundary value problem, showing the definitions of  $V$ ,  $V_0$ .



(b) Detail of geometry of acoustic boundary value problem showing the region near the source, applied to a transitional boundary layer flow.

**Figure 2.1** Geometry of the acoustic boundary value problem.

where  $\phi$  is the acoustic potential. The boundary condition for the acoustic potential is given by:

$$\frac{\partial \phi}{\partial y} = v_a(x, z, t) \quad \text{on } S_0 \quad (2.2)$$

where  $v_a$  is the potential flow perturbation velocity due to the presence of the boundary layer. In addition,  $\phi$  satisfies the Sommerfeld radiation condition on  $S$ . Note that the convected wave equation is not being used since  $M \ll 1$ .

Liepmann (1954) used this approach to describe the sound radiation from a turbulent boundary layer. He began his analysis with the solution to the boundary value problem just described :

$$\phi(x, t) = -\frac{1}{2\pi} \int \int_{S_0} v_a[x', t - \frac{|x - x'|}{c}] \frac{dS'}{|x - x'|} \quad (2.3)$$

where  $dS' = dx' dz'$  is the differential area on  $S_0$ . For the inviscid, moving portion of the flow in  $V$ , the perturbation pressure in the freestream is given by the Bernoulli equation linearized about the steady flow condition:

$$p(x, t) = -\rho \left[ \frac{\partial \phi}{\partial t} + U \frac{\partial \phi}{\partial x} \right] \quad (2.4)$$

Substituting Equation 2.3 into this relation, he obtained the expression for a subsonic

freestream over the planar surface  $S_0$  on which there is a prescribed normal velocity distribution:

$$p(x,t) = \frac{\rho}{2\pi} \int \int \frac{dS'}{|x-x'|} \left\{ \left[ \frac{\partial v_n}{\partial t} \right] - U [v_n] \frac{|x_1-x_1'|}{|x-x'|^2} \right\} \quad (2.5)$$

where the notation  $[ ]$  indicates a quantity evaluated at the source location  $x'$  and at the appropriate retarded time  $t - |x' - x|/c$ . At large  $r = |x' - x|$ , the second term is negligible compared to the first, so that it may be dropped when considering the farfield behavior. This reduces the expression for the farfield pressure to:

$$p(x,t) = \frac{\rho}{2\pi} \int \int \frac{dS'}{|x-x'|} \left[ \frac{\partial v}{\partial t} \right] \quad (2.6)$$

It should be pointed out that the second term in Equation 2.5 divided by  $-\rho U$  is identical to that used by Van Atta *et al.* (1982) to estimate the fluctuating potential flow velocity normal to the wall at a height just above the boundary layer.

If we move the density inside the integral in Equation 2.6, we may interpret the resulting equation as the time derivative of the unsteady mass flux through  $S_0$  for each point on  $S_0$  which contributes to  $v_n$ , evaluated at the appropriate retarded time. The radiation of sound from the boundary layer is then determined by the form which  $v_n$  takes. If  $v_n$  integrated over  $S$  changes with time, then the flow acts as a monopole type source. If, however, the integrated mass flux is identically zero, then the flow acts as a higher order source such as a quadrupole. The quantitative behavior of  $v_n$

may be found experimentally either by direct measurement or by measurements of the unsteady velocity in the boundary layer itself, making use of the continuity equation. To accomplish the latter, it is necessary to consider more closely the relationship between the unsteady displacement thickness and the potential flow disturbance.

## **2.2 BOUNDARY CONDITION FOR ACOUSTIC EQUATION**

By measuring the flow inside the boundary layer, it is possible to determine the behavior of the flow on  $S_0$ . As stated in Equation 2.2, the distribution of velocity normal to  $S_0$  constitutes a boundary condition for the acoustic potential. This is accomplished in one of two ways: First, the velocity component normal to the wall outside the boundary layer may be measured directly. Second, the instantaneous displacement thickness,  $\delta^*(x,z,t)$ , may be calculated at every point for every instant using the experimental data. By modeling the effect of the boundary layer on the outer flow as that of an additional wall thickness  $y = \delta^*(x,z,t)$ , it is possible to position  $S_0$  on this surface. Then, invoking concepts from slender body theory, the boundary condition may be "transferred" to the wall ( $y=0$ ).

### **2.2.1 The Displacement Thickness**

The displacement thickness,  $\delta^*$ , is a quantity that expresses the amount of streamwise mass flux that is lost to a uniform freestream due to the viscous action in

the boundary layer. The simplest example is a two-dimensional, steady laminar flat plate boundary layer. In this case the displacement thickness is given by:

$$\delta^*(x) = \int_0^{\infty} \left(1 - \frac{u(x,y)}{U}\right) dy \quad (2.7)$$

At any streamwise location in a flat plate boundary layer, the displacement thickness is the height that a streamline is displaced from its height  $H > \delta$  upstream of the plate. From the point of view of the potential flow, the displacement effect of the boundary layer is equivalent to a uniform inviscid flow slipping over a body whose shape is adjusted for the displacement thickness. For a three-dimensional boundary layer, the displacement thickness is a function of changes in both the streamwise and the spanwise mass flux in the boundary layer. These statements follow directly from the principle of conservation of mass for an incompressible flow. For example, a decrease in the streamwise mass flux will be reflected in an increase in the mass flux normal to the plate (for a two-dimensional flow). The product of the displacement thickness and the freestream velocity exactly equals the streamwise mass flux deficit, which is given by:

$$\text{mass flux deficit} = \rho \int_0^{\infty} (U - u(x,y)) dy \quad (2.8)$$

for a steady, two-dimensional boundary layer. If we extend this description of continuity to the unsteady flow in either transitional or turbulent boundary layers, we can see that fluctuations in the unsteady displacement thickness reflect the exchange

of mass flux between fluctuations in flow parallel to the body and fluctuations in flow normal to the body. These fluctuations in normal velocity are to be used as the boundary condition for the acoustic potential.

### **2.2.2 Calculating Normal Velocity from the Displacement Thickness**

While the displacement thickness is a useful quantity for constructing a boundary condition for the acoustic equation, it is not necessarily derived from velocity data in a straightforward way as Liepmann indicated. The analytical work that has proceeded on the basis established by Liepmann that is relevant to this work has continued to use the displacement thickness. Because of the difficulty in estimating the displacement thickness using data, the present analysis has been based on a related quantity, the mass flux deficit (MFD). This quantity relates the normal velocity perturbation to the unsteady boundary layer data in a direct manner, while the displacement thickness does not, as will be shown in this section.

Expressing the fluctuating normal velocity in terms of an unsteady displacement thickness proceeds according to the perturbation theory for slender bodies (Liepmann & Roshko, 1957). Within the framework of this theory, the component of velocity normal to the freestream flow direction of the flow over a body is the result of the body shape perturbing the inviscid, uniform flow. Liepmann & Roshko (1957) modeled this displacement effect as an effective piston motion imposed on steady, potential flows. In their discussion of the flow of viscous fluids, they note that the theory can be extended by simply changing the body shape by the addition of



the displacement thickness, assuming that there is no boundary layer separation on the body. For a steady, two-dimensional boundary layer, the normal perturbation velocity is entirely due to the effect of the displacement thickness and is given by:

$$v_n(x)|_{y=\delta} = U \frac{\partial \delta^*(x)}{\partial x} = U \frac{\partial}{\partial x} \int_0^{\delta(x)} \left(1 - \frac{u(x,y)}{U}\right) dy \quad (2.9)$$

where  $x$  is the streamwise coordinate,  $U$  is the freestream velocity,  $\delta(x)$  is the boundary layer thickness, and  $\delta^*(x)$  is the displacement thickness. Note that in the usual definition of displacement thickness the upper limit on the integral is infinity, while here the integral only goes up to the boundary layer height. Since the displacement thickness is defined in terms of the amount of mass flux lost to the incoming stream *due to motion in the boundary layer*, the upper limit on the integral is, strictly speaking, the boundary layer height. In a steady, two-dimensional flow, for which this definition is illustrated, the nature of the flow allows the limit of integration to be extended to infinity because the mass flux deficit in the freestream is entirely negligible. While the definition of  $\delta^*$  given in Equation 2.9 holds for situations other than a two-dimensional, steady boundary layer flow, the relationship between  $\delta^*$  and the mass flux deficit is not always so straightforward.

For an unsteady two-dimensional boundary layer with a uniform, steady potential flow upstream of the plate, the equation describing the normal velocity also

includes an unsteady term:

$$v_n(x,t)|_{y=\delta^*} = \frac{\partial \delta^*(x,t)}{\partial t} + U \frac{\partial \delta^*(x,t)}{\partial x} \quad (2.10)$$

$$v_n(x,t)|_{y=\delta} = U \frac{\partial}{\partial x} \int_0^{\delta(x)} \left(1 - \frac{u(x,y,t)}{U}\right) dy$$

The first equation was given by Laufer *et al.* (1964) and results from kinematic theory by enforcing the condition that the normal velocity of the fluid relative to the effective "wall" ( $y = \delta^*(x,t)$ ) is zero. The velocity of the fluid is tangent to the moving "wall" at any instant:

$$\frac{\partial f}{\partial t} + (\mathbf{U} \cdot \nabla) f = 0 \quad (2.11)$$

where  $f = \delta^*(x,t) - y$  is the surface describing the effective body shape due to the displacement effect and  $\mathbf{U}$  is the velocity vector  $\mathbf{U} = (U+u, v, w)^T$ . The potential flow perturbation velocities  $u$ ,  $v$ , and  $w$  due to the flow over the body are small such that:

$$\frac{u}{U}, \frac{v}{U}, \frac{w}{U} \ll 1 \quad (2.12)$$

The resulting unsteady term exhibits the motion of the flow streamlines. The second of Equations 2.10 has been derived by integrating the continuity equation for an incompressible flow. The relationship between the two approaches is complicated in two ways. First, the normal velocity from the viscous/inviscid interaction approach

is given for  $y=\delta^*$ , while the normal velocity obtained from integrating the continuity equation is evaluated at the edge of the boundary layer. Second, the ready identification of  $\delta^*U$  with the streamwise derivative of the mass flux deficit has been lost. However, at any instant the normal velocity at the edge of the boundary layer is still given by the streamwise gradient of the streamwise mass flux deficit.

The situation is complicated further in a three dimensional boundary layer where the freestream is uniform and steady upstream of the plate. In this case the normal velocity is also affected by spanwise flow:

$$v_n(x,z,t)|_{y=\delta} = U \left\{ \frac{\partial}{\partial x} \int_0^{\delta(x)} \left( 1 - \frac{u(x,y,z,t)}{U} \right) dy + \right. \\ \left. - \frac{\partial}{\partial z} \int_0^{\delta(x)} \frac{w(x,y,z,t)}{U} dy \right\}. \quad (2.13)$$

This relation was given by Lighthill (1958). The three-dimensional analog to the first of Equations 2.10 is given by:

$$v_n(x,\delta^*,z,t) = \frac{\partial \delta^*}{\partial t} + U \frac{\partial \delta^*}{\partial x} + w \frac{\partial \delta^*}{\partial z} \quad (2.14)$$

This expression includes the contribution of the spanwise mass flux to the normal velocity.

From this discussion it is apparent that deducing the unsteady normal velocity perturbation from unsteady boundary layer velocity measurements is unnecessarily

complicated by reference to the displacement thickness. Instead, it is more straightforward to proceed from velocity profile measurements to the normal velocity perturbation through integrating the continuity equation. For this reason the mass flux deficit is used here instead of the displacement thickness, as in Equation 2.13. The use of the displacement thickness may work well for a formal derivation but is not well suited for direct application to experimental data.

### 2.2.3 Transfer of the Boundary Condition to the Wall

The boundary condition for the acoustic equation (Equation 2.2) may be rewritten in terms of the velocity field in the boundary layer:

$$\begin{aligned} \frac{\partial \phi}{\partial y}(x, \delta, z, t) &= v_s(x, \delta, z, t) = \\ &= U \frac{\partial}{\partial x} \int_0^\delta \left(1 - \frac{u(x, y, z, t)}{U}\right) dy + \\ &\quad - \frac{\partial}{\partial z} \int_0^\delta w(x, y, z, t) dy \end{aligned} \quad (2.15)$$

for  $S_0$  defined as the surface  $y = \delta(x, z, t)$ . For simplicity in the analysis, the boundary condition may be transferred to  $y = 0$  using ideas from slender-body theory (Liepmann

and Roshko, 1957). This is accomplished by expanding  $v_a(x, \delta, z, t)$  in a Taylor series in  $y$  about  $y=0$ :

$$v_a(x, \delta, z, t) = v_a(x, 0, z, t) + \left(\frac{\partial v_a}{\partial y}\right)\bigg|_{y=0} \delta + \dots \quad (2.16)$$

By neglecting terms after the first, it is possible to state:

$$\begin{aligned} \frac{\partial \phi}{\partial y}(x, 0, z, t) &= v_a(x, 0, z, t) \approx \\ &\approx U \left( \frac{\partial}{\partial x} \int_0^\delta \left( 1 - \frac{u(x, y, z, t)}{U} \right) dy \right) - \frac{\partial}{\partial z} \int_0^\delta w(x, y, z, t) dy \end{aligned} \quad (2.17)$$

In slender body theory, this step is taken before the analysis is carried out but is confirmed after the solution is in hand. This involves showing that  $\lim_{y \rightarrow 0} (\partial v / \partial y) \rightarrow 0$ , as shown by Karamcheti (1966). Thus far a formal solution for the boundary layer noise problem has been developed using the Liepmann analogy. The next step is to supply the detailed behavior of the boundary layer velocity field so that the boundary condition 2.17 may be constructed and the acoustic equation solved.

### 2.3 BOUNDARY CONDITION FOR A TURBULENT SPOT

In this section, the formal expressions for the radiated sound which motivate the boundary layer measurements are presented. The details of the sound estimation based on these expressions using the data are presented in Chapter 5.

Lauchle (1981) analyzed the sound production from the transition region of a flat plate boundary layer by modeling the displacement thickness fluctuations. Using

the approach of Libby (1975), Lauchle (1981) wrote a description of the instantaneous displacement thickness as a weighted sum:

$$\delta^*(x,t) = I(x,t)\delta_T^*(x) + (1 - I(x,t))\delta_L^*(x) \quad (2.18)$$

where  $I(x,t)$  is the indicator function. This quantity is defined as follows: it takes two values, zero when the boundary layer at the location  $x$  is laminar at time  $t$ , and one when it is turbulent. Also, the time average of the indicator function is the equal to the intermittency :

$$\overline{I(x,t)} = \gamma(x) \quad (2.19)$$

From this definition it can be seen that the time average of Equation 2.17 yields the intermittency-weighted form of the displacement thickness established by Dhawan and Narasimha (1958):

$$\overline{\delta^*}(x) = \gamma(x)\overline{\delta_T^*} + (1 - \gamma(x))\overline{\delta_L^*} \quad (2.20)$$

This indicator function-weighting approach assumes that the displacement thickness has the value it would have in a turbulent boundary layer in the interior of a turbulent spot, and the value it would have in the undisturbed laminar boundary layer outside the spot. For any location  $x$  in the boundary layer, then, when a turbulent spot is over that location,  $\delta^*(x,t) = (\delta^*)_T$ , otherwise,  $\delta^*(x,t) = (\delta^*)_L$ . The instantaneous displacement thickness may be rewritten as:

$$\dot{\delta}(x,t) = \dot{\delta}_L(x) + I(x,t)\Delta\dot{\delta}(x) \quad (2.21)$$

where  $\Delta\dot{\delta}(x)$  is the difference between the values of the laminar and turbulent displacement thicknesses at a given location  $x$ . Lauchle further assumed that the transition between the laminar and turbulent states was not instantaneous, but consisted of an accommodation region at the edges of the spot which followed an exponential evolution, characterized by the rise time  $t_i$ , as shown in Figure 2.2. Spatial variations in  $t_i$  were not considered. The unsteady normal velocity was related to fluctuations in  $\dot{\delta}$  through:

$$\begin{aligned} v_n(x,t) &= \frac{\partial \dot{\delta}}{\partial t} = \\ &= \Delta\dot{\delta}(x) \frac{\partial I}{\partial t}(x,t) \end{aligned} \quad (2.22)$$

after Laufer, *et al.*, (1964), who considered the sound radiated from a turbulent boundary layer to an observer moving at  $U$ . Substituting this expression into Equation 2.6, we obtain for the sound radiation:

$$p(x,t) = \frac{\rho}{2\pi} \int \int \frac{dS'}{|x' - x|} \Delta\dot{\delta}(x') \left[ \frac{\partial^2 I}{\partial t^2} \right] \quad (2.23)$$

This result was also obtained by Audet *et al.* (1989) from a Lighthill analogy approach where they applied indicator function weighting to the Lighthill stress tensor,

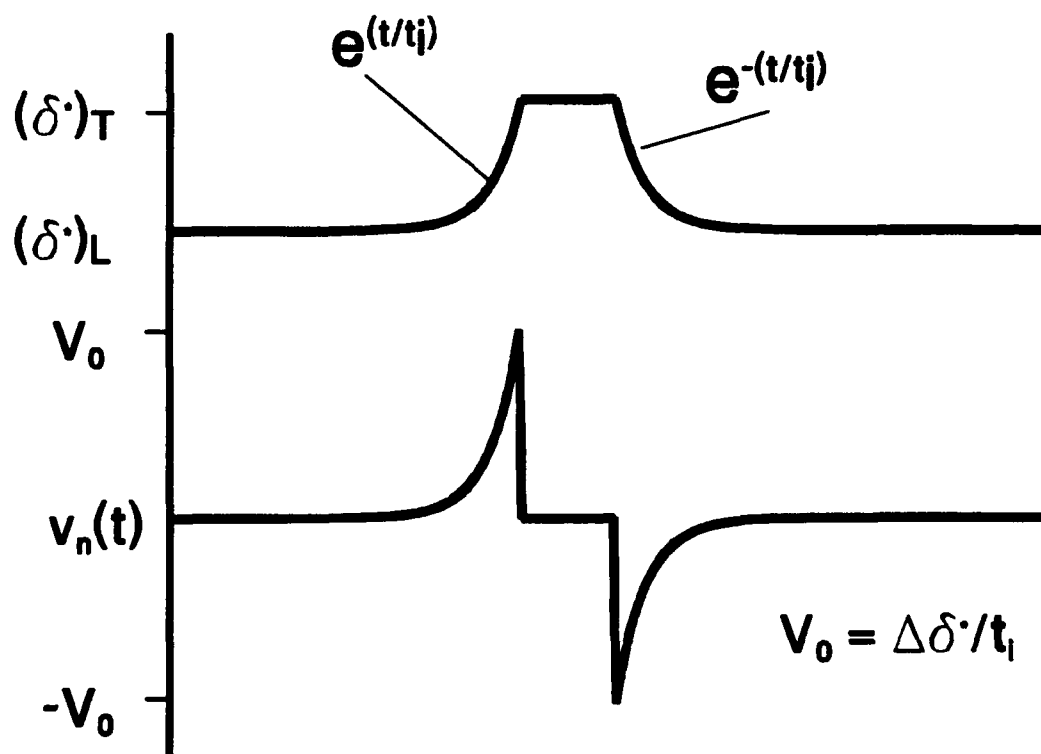


**Figure 2.2** Intermittency-weighted form of unsteady displacement thickness at a fixed location and the corresponding normal velocity.



using assumptions similar to those of Lauchle (1981). It should be mentioned that Lauchle's (1981) result was different than this result in that both the time derivative and the  $(1/r)$  term were outside the integral. These differences are consistent with the assumptions of source compactness made by Lauchle (1981).

Thus, using an indicator function-weighted description for the displacement thickness allows the sound radiation problem to be formulated in terms of a rise time,  $(t_i)$ , a function describing the change in displacement thickness at each streamwise location,  $\Delta\delta^*(x)$  (Lauchle (1981) neglected the variation in  $\Delta\delta^*$  because of the small streamwise extent of the transition zone), and the space-time behavior of the indicator function. Since Lauchle (1981) was interested in describing the acoustic emissions of the entire transition region, he constructed a space-time correlation function for  $I(x,t)$  to describe its behavior over the extent of the transition zone. A description of the indicator function for an isolated spot may be expressed in a more deterministic manner using measurements of the arrival times of the laminar/turbulent interfaces. Therefore, to implement this model using experimental data, it is necessary to measure  $\Delta\delta^*(x)$ ,  $t_i$ , and the space-time behavior of  $I(x,t)$ . This has been accomplished through measurements of the mass flux deficit from which these quantities have been calculated (see Chapter 4). The estimation of the sound radiation from transitional flows through the Liepmann analogy using the experimental data is presented in Chapter 5.

## **CHAPTER 3**

### **EXPERIMENTAL APPARATUS**

This section details the apparatus used to carry out the experiments. The design and construction of the Laminar Flow Water Channel and the measurement system are described. The performance of the facility and its components is discussed along with some suggested improvements.

#### **3.1 WATER CHANNEL FACILITY**

All of the experiments for this study took place in the Aerospace Engineering Laminar Flow Water Channel, a new facility constructed over a period of two and a half years for these experiments. The facility is located in the Department of Aerospace Engineering at Penn State. The flow loop is a closed circuit which holds approximately 3500 gallons. All but one of the experiments were carried out at a test section flow speed of 0.41 m/s, although the maximum speed is much higher. The important features of the flow loop may be seen in Figure 3.1. In this diagram the flow moves in a clockwise direction around the loop. The first important feature is the test section where the experiments took place. Downstream of the test section is the pump. Continuing in the flow direction, there is a return leg consisting of a system of diffusers, a turnaround duct, and a wide-angle diffuser. The return leg decelerates the flow so that the turbulence management causes minimal flow losses. Following the turbulence management there is the contraction leading into the test section.

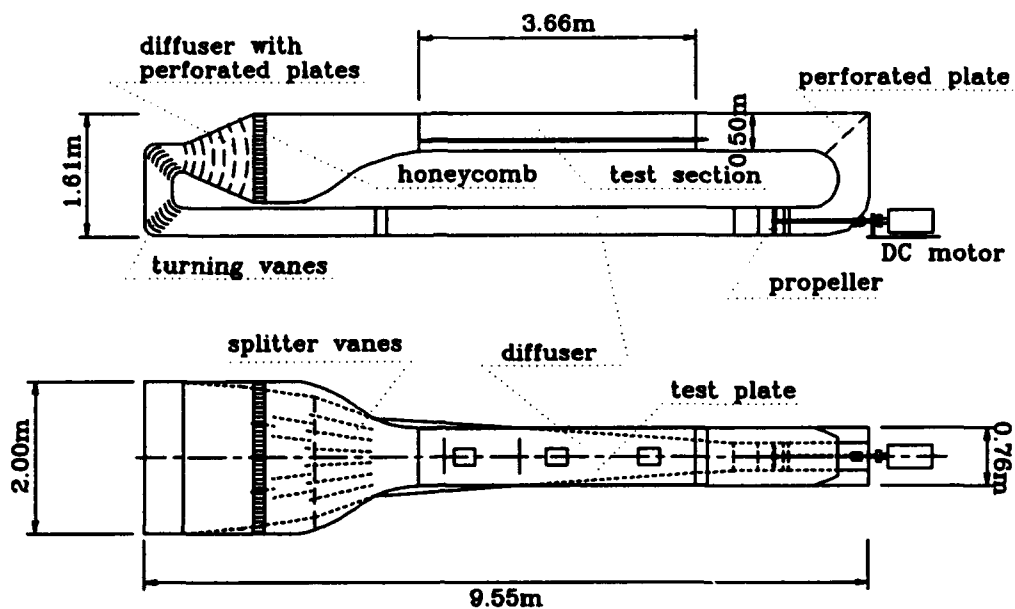


**Figure 3.1** Water channel facility. Flow moves clockwise around the loop.

### **3.1.1 Test Section**

#### **3.1.1.1 Floor and Walls**

The test section is 3.66 m long and has a nominal cross sectional area of 0.387 m<sup>2</sup>, which varies with water height in the test section. The test section bottom is made of 2.54 cm thick hard anodized aluminum and the walls are made of 3 sections of 50.8 cm x 1.22 m x 1.27 cm thick glass panes. The test section was constructed on a welded steel frame which is bolted fast to the laboratory floor. A one-piece gasket seals the joints not only between the base plate sections but also the glass walls of the test section. For access to the test section from beneath, each of the three base plate sections has a 27.9 cm x 21.6 cm plexiglass window insert which is bolted into the base plate and sealed with an O-ring.

On either side of the test section is welded a 3.66 m x 0.102 m C-beam, which supports a 2.54 cm diameter rail. These rails support an instrumentation rack which is constructed of 10.2 cm x 4.4 cm steel C-beam sections. The stand travels along the rails on sets of bearings. Movement along the rails may be restricted by tightening a bolt in the bearing mount which draws the bearing mount tight around the rail. Loosening these bolts allows the stand to move freely.

The test section is connected to the flow loop both upstream and downstream by aluminum flanges. These flanges are attached to the test section in two ways. Along the bottom of the test section, the flanges are bolted to the base plate, while the glass side walls are attached (and sealed) to the flanges using silicone rubber caulking. Rubber gaskets seal the joints between the flanges and their adjacent sections.

### 3.1.1.2 Flat Plate Test Model

The test plate which runs the length of the test section is constructed from three 1.22 m x 73.3 cm sections of 1.91 cm aluminum tool and jig plate. This plate is mounted in the test section on a series of rails at a height of 12.7 cm from the floor of the test section. This positions the test surface 14.6 cm above the test section floor, leaving as much as 31.1 cm of depth beneath the free surface. The support rails beneath the surface are streamlined on their leading and trailing edges to help reduce blockage beneath the test plate.

A 12:1 ellipse is machined into the leading edge of the model. In addition, a movable tail with a 15.2 cm chord length is attached to the trailing edge of the model to enable control of the leading edge stagnation point location. As shown in Figure 3.2, two dye slots are mounted in the model, one each in the first sections. These slots are fed from a manifold which is connected to four 0.635 cm copper tubing lines which lead to a head tank from which the dye is dispensed. The dye that was used in these experiments consisted of a Fluorescein Disodium Salt solution which emits green light when excited by blue light. Also machined in the test surface are 5.1 cm diameter circular ports for surface-mounted sensors and three 20.3 cm x 27.9 cm rectangular windows for optical access from below. Plexiglass inserts are machined and mounted into these ports flush to the test surface. The rectangular windows in the two upstream plate sections also have two 5.1 cm diameter circular ports machined into their centerlines and plexiglass inserts are available for these ports as well.

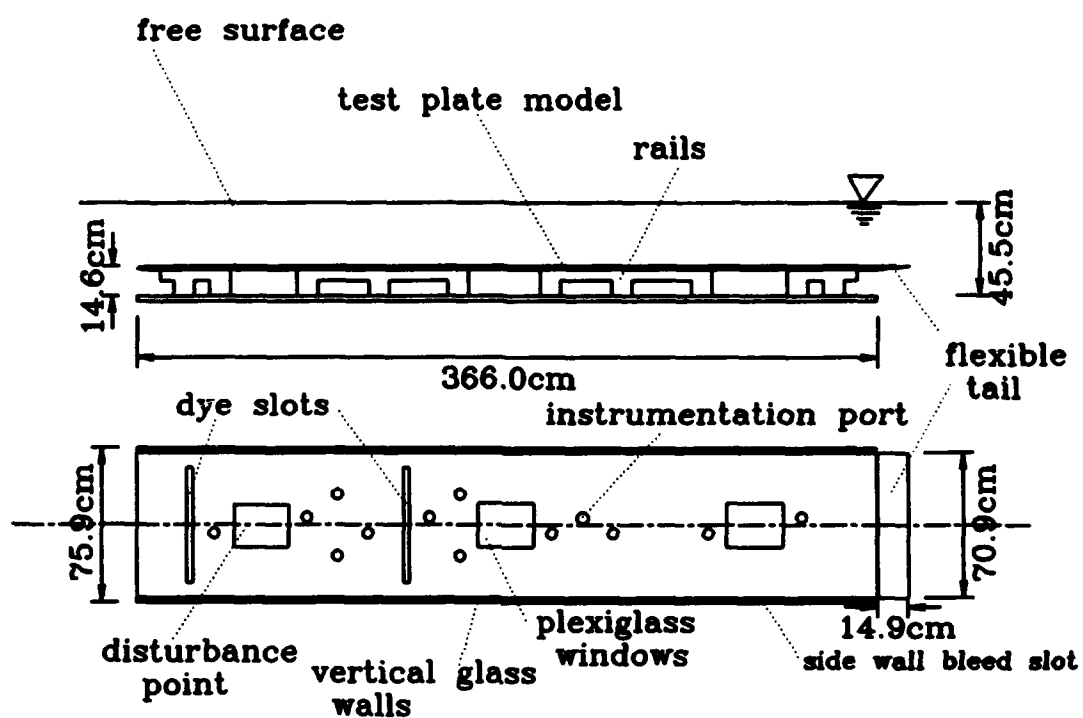


Figure 3.2 Flat plate test model.

A provision is available for control of the sidewall contamination of the laminar boundary layer by adjustable slots at the side edges of the plate. As shown by Motohashi and Blackwelder (1983), controlling the sidewall contamination should allow for a greater plate area exhibiting laminar flow. This is accomplished by causing a higher pressure on the upper side of the plate than on the lower side, which allows the turbulent boundary layers on the sidewalls to be bled away, delaying destabilization of the test surface laminar boundary layer. The gap between the edge of the plate and the sidewall is nominally 1.27 cm and is adjustable down to zero by using four nylon tabs on each side.

#### **3.1.1.3 First and Second Corners**

The test section is followed by a 1.22 m length of empty channel which acts as a buffer between the test section and the first corner. This section insures that any secondary flow induced by the turn will have a reduced influence on the flow in the test section. Next comes the first corner. The flow through the first corner is aided in turning by a 0.159 cm thick stainless steel perforated plate placed at a 45° angle to the oncoming flow. This plate has 0.32 cm perforations and a 64% open area ratio. Beyond this plate the cross sectional area is then reduced through the second corner to that of the pump (856 cm<sup>2</sup>).

#### **3.1.2 Pump**

The axial flow pump utilizes a propeller driven by a 7.5-HP DC electric motor. A schematic of the pump is shown in Figure 3.3. The power of the motor is transmitted to the propeller through a 157 cm long, 3.5 cm-diameter stainless steel

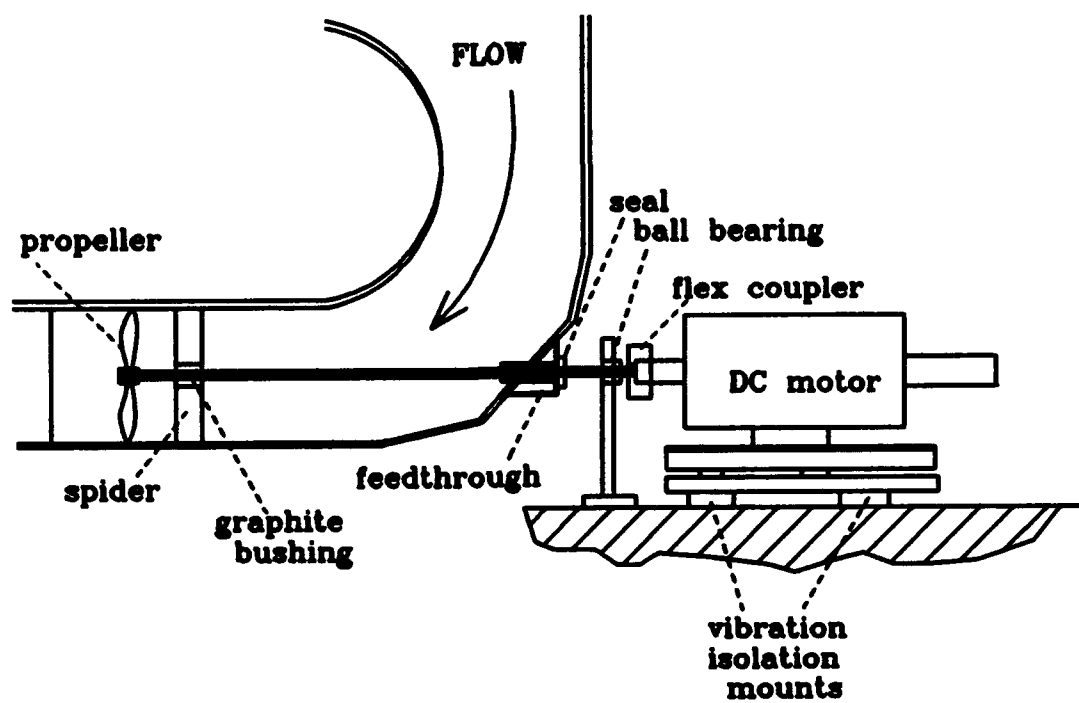


**Figure 3.3** Detail of water channel pump.



shaft. The shaft is connected to the motor using a flexible coupler. The propeller is a 41 cm brass boat propeller which has been "tipped" on a lathe to a nominal 30.5 cm diameter to fit in the 30.5 cm passage. The shaft is supported in two places: by a ball bearing mounted in a vibration-isolated bracket bolted directly to the floor, and by a self-lubricating graphite bushing located in the flow passage. The radial loads on these supports are minimal, and the outside ball bearing supports the approximately 45 N thrust load from the propeller. The shaft feedthrough, where the shaft passes through the wall of the flow passage, consists of a brass tube soldered to a brass plate which is mounted to the wall, as shown in Figure 3.4. Sealing this wall opening was accomplished by covering the brass plate and tube with fiberglass-reinforced epoxy resin. On the outside end of the brass tube a Chicago Rawhide CR-11171 seal is mounted. This seal has worked quite effectively in sealing this potentially troublesome joint. To prevent motor vibrations from transmitting through the laboratory floor into the water channel, the pump motor is mounted on a heavy steel base which in turn is mounted to the floor using Vlier CMB-7 vibration isolators.

### **3.1.3 Return Leg**

The return leg of the flow loop begins immediately downstream of the pump. This section was designed to increase the cross-sectional area of the flow passage from that at the pump to that of the settling chamber as efficiently as possible while keeping the flow in the test section steady. The design was constrained by the geometry of

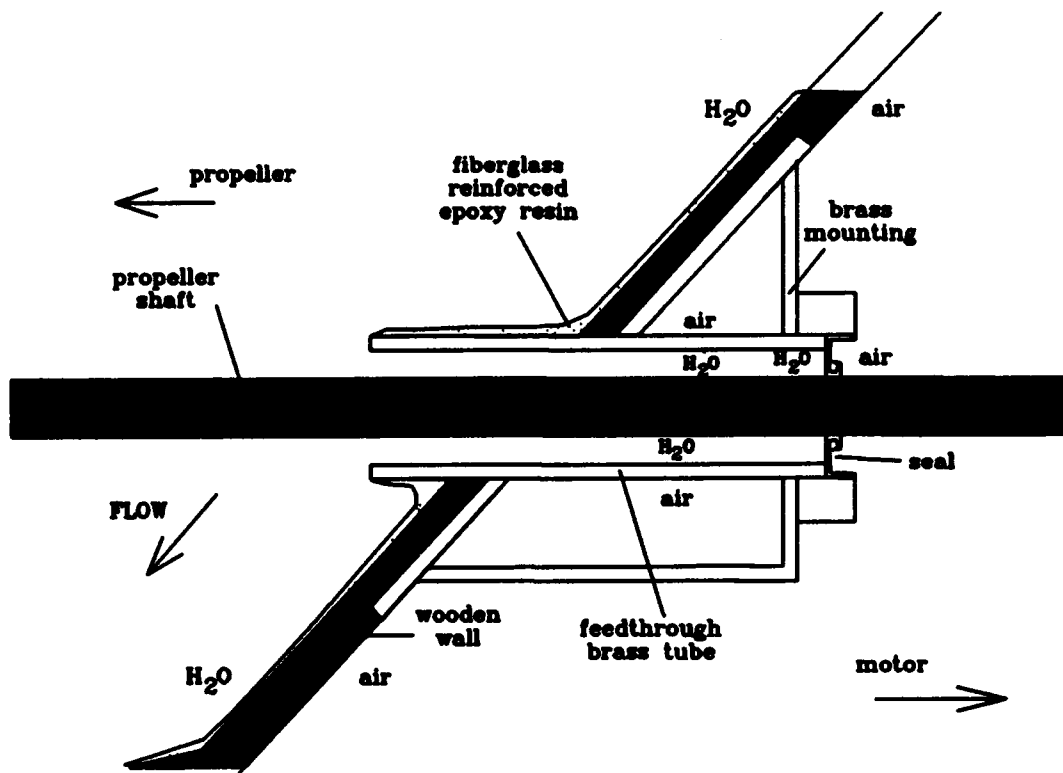


Figure 3.4 Detail showing propeller shaft feedthrough and how it is sealed.

both the room where the facility is located and the salvaged sections of the original settling chamber.

The first section is a 4.57 m long x 35.6 cm high, small-angle ( $8^\circ$ ) diffuser. This diffuser begins at a joint with the propeller housing which is made of two flanged PVC 30.5 cm pipes. One flange is connected to the pump and one to the diffuser. The joint between the PVC pipe lengths consists of a pipe clamp. At the inlet the diffuser has a 34.3 cm-diameter circular cross-section. This shape gradually changes to a rectangular cross section 220 cm downstream of the joint. The outside construction of the first diffuser is a rectangular cross section, with the internal shape formed by filling the corners of the rectangular duct with fiberglass-reinforced epoxy resin. The resin was used to seal the inside surface from leaks and to reinforce the corner joints in the wooden walls. The walls are also reinforced outside the flow passage by ribs made of 5.1 cm x 1.7 cm boards, spaced approximately every 30.5 cm in the axial direction.

The diffuser angle and length were based primarily on the performance data of Japikse (1984). This diffuser is not within the transitory stall regime. Transitory stall would be best for pressure recovery, but is unacceptable from a steady flow perspective. An analysis was carried out to estimate the locations of any flow separations in the diffuser using the STAN6 boundary layer code, developed by W.M. Kays. This is a finite difference code which uses a mixing length turbulence model. The procedure for locating flow separation was as follows: First, the pressure gradient given by a uniform inviscid flow through the diverging duct was used to

calculate the boundary layer up to separation (the point where the wall shear stress went to zero). Then, a correction for the wall shape based on the calculated displacement thickness distribution of the boundary layer was used to recalculate the pressure gradient distribution. This continued iteratively until the displacement thickness matched the adjustment to the duct incorporated in the code. This procedure did not account for any three-dimensional effects due to variations in duct cross sectional shape and did not account for inlet swirl induced by the propeller. The swirl, if significant, would aid in delaying separation, so it is believed that the calculation is conservative and that no large-scale, unsteady separations occur in the first stage of the diffuser. Experimental observation has not revealed any large-scale unsteadiness which would indicate transitory stall.

The second stage of the return leg is a wider angle diffuser, as shown in Figure 3.5. In its original configuration, the diffuser angle was  $60^\circ$ . This angle would result in a fully-separated "jet" flow, so the angle was reduced to  $40^\circ$  by installing wooden inserts to change the shape of the flow passage. In addition, six 80.6 cm long splitter vanes are positioned to divide the duct into seven passages. These vanes were manufactured from marine-grade plywood and coated with fiberglass-reinforced epoxy resin. The leading edges are rounded to prevent leading edge separation and the trailing edges are tapered to reduce the thickness of the trailing wakes.

The positions of these vanes was determined using the criterion set by Feil (1964). In general, splitter vanes are placed such that they divide the diffuser passage

evenly. In doing so, the vanes lie on rays emanating from the point of intersection of lines drawn extending the diffuser walls into the inlet duct (point O in Figure 3.6). Feil advocates placing the vanes on rays emanating from a "source-point" O' which is upstream of point O. This placement helps to prevent separation at the location most likely to separate, the inlet corner, where the flow curvature is the highest. This result reflects several factors. First, the vanes help to turn the flow around the corner. Second, the angle is smaller in the outside passages, which are more likely to separate because the boundary layer on the sidewall began growing far upstream of the corner where the vanes begin. In this way, a "crowding" of the potential flow in the diffuser due to the growing boundary layers (especially the sidewalls) helps to retard separation. Lastly, dividing the duct into smaller passages allows any separations that do occur to be contained. The corners at the diffuser joint were also rounded to further guard against separation.

A provision for boundary layer control was also added at the joint ahead of the wide-angle diffuser. Here two slots are placed in the wall. The filter intake was a simple slot, as shown in Figure 3.7. Suction at this location removes the low momentum fluid near the wall so that the boundary layer is less likely to separate at the corner. Just downstream of the suction slot a blowing slot (the filtration outlet) directs a jet along the wall, again, to re-energize the boundary layer. A filtration system has been installed to process the water through this loop.

In addition to the vanes just mentioned, two rows of vanes were placed just downstream of the first row. These vanes help to turn the flow through the

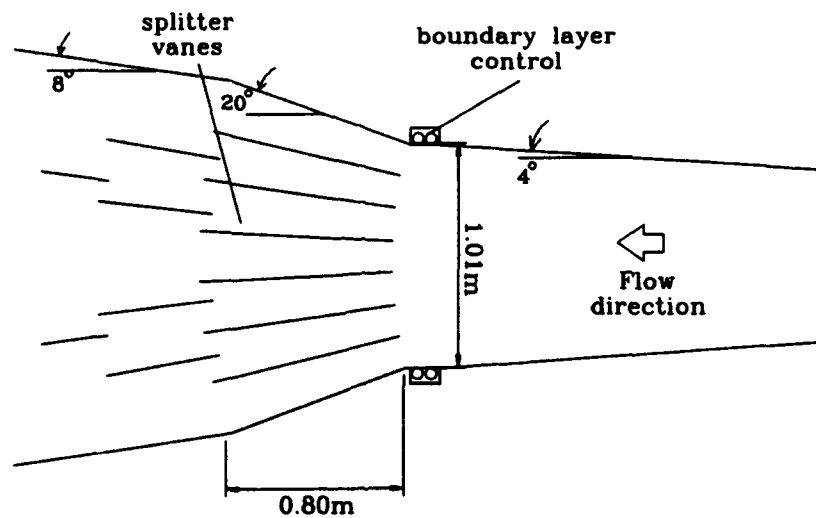


**Figure 3.5** Detail of the compound diffuser showing the location of the filtration intake/outlet and the splitter vane configuration.

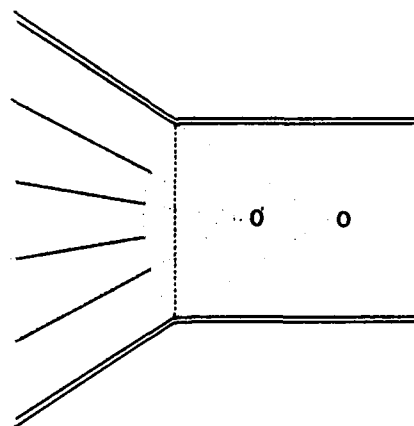


**Figure 3.6** Diffuser source-point displacement (Feil, 1964). Ideal flow in diffuser looks like flow from source at O. Vanes set on rays emanating from source at O' help retard separation at diffuser joint corners.

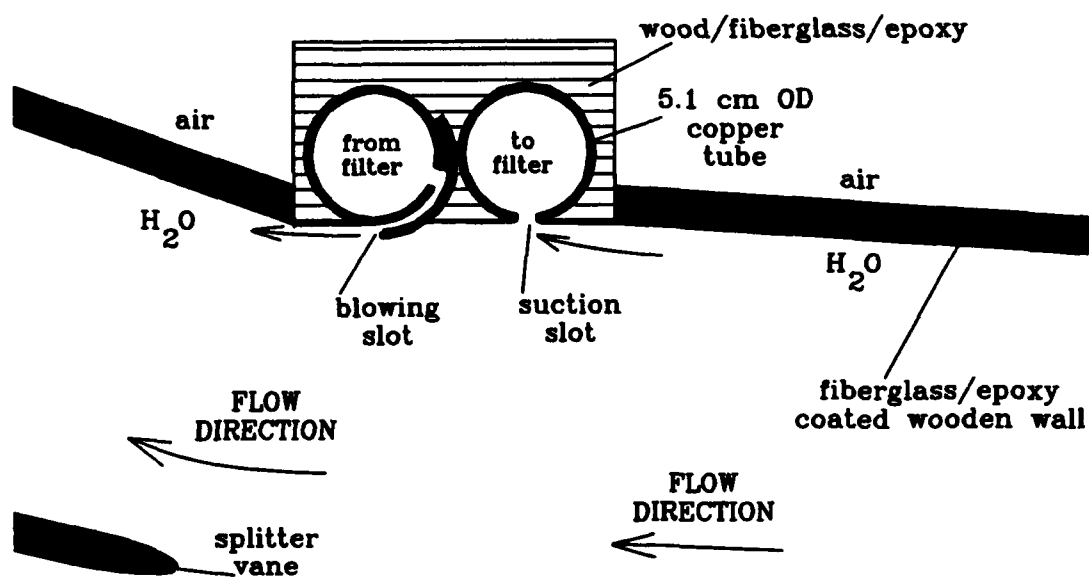


**Figure 3.7** Schematic of filtration inlet/outlet used as boundary layer control.

decreasing angle of the flow passage. It should be emphasized that the design of These diffusers optimizes the flow passage for steadiness, rather than for pressure recovery. Downstream of the diffuser the flow passes through two 90° corners. The flow passage at this location is 2 m wide and 35.6 cm high. The corners each have a 15.2 cm turning radius. To help prevent separation of the flow in the corners, six PVC turning vanes with a 1.27 cm nominal thickness and a 21.6 cm chord length are installed. The gaps between the vanes are 7.11 cm, so that the chord-to-gap ratio is approximately 3. The vanes themselves are made of quarter sections of a 30.5cm diameter PVC pipe cut lengthwise. The leading edges of the vanes were rounded and the trailing edges were tapered to improve the flow quality.

The final diffuser begins at the exit of the second corner. This diffuser increases the flow area from 0.356 m<sup>2</sup> to 1.14 m<sup>2</sup> in 1.14 m of streamwise distance. This rapid expansion decelerates the flow so that the flow conditioning devices in the settling section (a honeycomb and screens) will not cause a large head loss to the flow. The diffuser is equipped with seven perforated plates (0.159 cm thickness, 0.3175 cm perforations, 64% open area) which act to re-energize the wall boundary layers and prevent them from separating. These perforated plates also act to break up the wakes of the turning vanes so that the flow is uniform upon leaving the diffuser. The number of perforated plates was found by a calculation similar to that done for the lower diffuser. The STAN6 code was run until separation, and then the effect of a perforated plate was modeled by reducing the momentum thickness Reynolds number by 50% and the code was run iteratively again until the flow was



found to separate. The separation distance was found to increase with distance travelled along the diffuser axis. The choice of seven plates was a conservative estimate of plates necessary to prevent separation because the freestream turbulence introduced by the perforated plates also aids in preventing separation.

Following the diffuser is the settling section where the flow conditioning is installed. First, there is a 15.2 cm long honeycomb, which has 0.32 cm-diameter cells. The plastic honeycomb was manufactured by Plascore, Inc. Second, there is the provision for fine-mesh screens, which will be installed at a future date. The flow conditioning is completed by passing the flow through a 6:1 contraction before it enters the test section.

## **3.2 DATA ACQUISITION**

### **3.2.1 Laser Doppler Velocimeter**

The laser-Doppler Velocimeter used for all measurements was a Thermal Systems, Inc. (TSI) one-component system, based upon a 15 mW Helium-Neon laser. A schematic of the system components is shown in Figure 3.8. The laser is mounted vertically, pointing downwards, on the travelling instrumentation stand. A right-angle mirror, which moves with the optics, directs the laser beam into the optical train which is mounted in either forward or backscatter mode. The transmitting optics were mounted so that the beam splitter could be rotated to  $90^\circ$  in order to measure the vertical component of velocity directly. The optical axis is positioned so that when measuring the streamwise component of velocity the beams approach the test surface

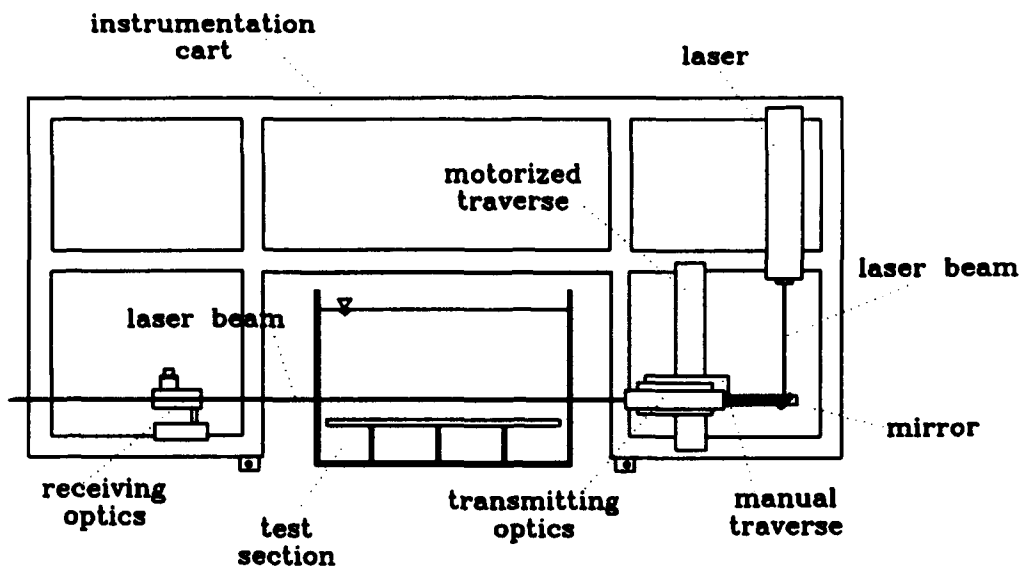


**Figure 3.8** Schematic of LDA setup. Laser and optics are mounted to the instrumentation stand. Flow is into the page.

at a slight angle and are not blocked when the probe volume was less than a beam diameter from the wall. The optical train is been mounted to a Velmex A4012 spanwise motion traverse that has 15.24 cm of available travel. This traverse is driven manually. The spanwise traverse and the right-angle mirror that directs the laser beam into the LDV optics were both attached to an aluminum plate which was translated vertically using a Velmex B4024 motorized traverse. The vertical traverse lead screw and stepper motor provide precise motion -- 1574 steps/cm. This motion is controlled by a Centroid Motion Controller. Commands are sent to the Centroid controller through the serial port of the lab computer, an IBM-PC AT. A Turbo Pascal program, which also controls the data acquisition, is used to send the commands. The combination of the streamwise travel of the instrumentation stand, the manual spanwise traverse and the motorized vertical traverse allows three-dimensional positioning capability for the LDA system.

### 3.2.2 Data Acquisition

The signal from the LDV photodetector was fed into to a TSI Model 1980B counter processor, equipped with a Model 1988 Analog Out Module. The counter was set to process Doppler bursts with at least 16 fringe detections. The time series velocity data were acquired using the frequency-out port, which delivered a signal between 0 and 10 volts proportional to the binary voltage mantissa of the last validated Doppler burst processed by the counter. Thus, the analog out module provided a random sample and hold representation of the velocity time series. Using the sample-

and-hold signal automatically corrects for velocity bias errors in the average velocity. The analog output from the frequency-out port was sampled at 250 Hz on a PC-based MetraByte DAS-16 analog-to-digital conversion board operating in the polled mode on a 0-10 v gain setting.

A Turbo Pascal program was used to control the measurement of the velocity profiles. First, the program asks for the streamwise and spanwise locations of the probe volume. Then, it asks the user to position the probe volume in the freestream so that the freestream velocity at that location can be measured. Next, the counter settings that will be used for the profile measurement are entered into a data file. Once the freestream velocity has been measured, the user is asked to position the probe at the wall and the program waits until the user tells the program that the probe is so positioned. The user positions the probe by telling the program how many steps and in what direction to move the traverse. This enables the user to position the probe at the wall as follows: First, a sharp-cornered block of known height is placed on the test plate. Second, the probe volume is brought down so that it just barely touches the corner of the block. Looking at the oscilloscope during this procedure allows the user to find the vertical position of the probe volume for which the maximum amount of light is scattered from the probe volume. This ensures a repeatable means of finding the location of the wall. Once the wall has been located, the program follows the procedure given in the previous paragraph for measuring the velocity profile using a predefined list of y-locations for measurement.

To measure the unsteady profiles, the data acquisition must be triggered based upon the generation of the turbulent spots. Details of the spot generation procedure are given in the next section. The profiles consisted of time series of velocities measured at 22 heights above the plate. The distance between heights was scaled on the thickness of the laminar boundary layer,  $\delta_L$ , at the location in question. The first 12 measurement heights were evenly spaced, separated by  $\delta_L/12$ . The last 10 were also evenly spaced, but separated by  $\delta_L/3$ . Thus, the extent of the vertical traverse was just over four laminar boundary layer heights. At each measurement location, 50 spot samples were taken. This number was found to be sufficient to achieve a convergence of an ensemble average. Figure 3.9 shows the convergence of the ensemble average. In this figure, the ordinate is the time-average of the absolute value of the difference between the average of  $n$  samples and the average of  $n-1$  samples. Figure 3.10 shows the ensemble-averaged time series for the mean and the variance of the streamwise component of velocity at  $y=0.8$  mm,  $x=1.53$  m,  $z=0$  m, and  $U=40.6$  cm/s. Note that the variance outside the portion of the time series corresponding to the turbulent spot is low, indicating that the measurement noise is a small part of the variance associated with the spot.

The process of generating spots, acquiring the time series, and then moving the traverse to the next station was controlled by the laboratory computer. The sequence

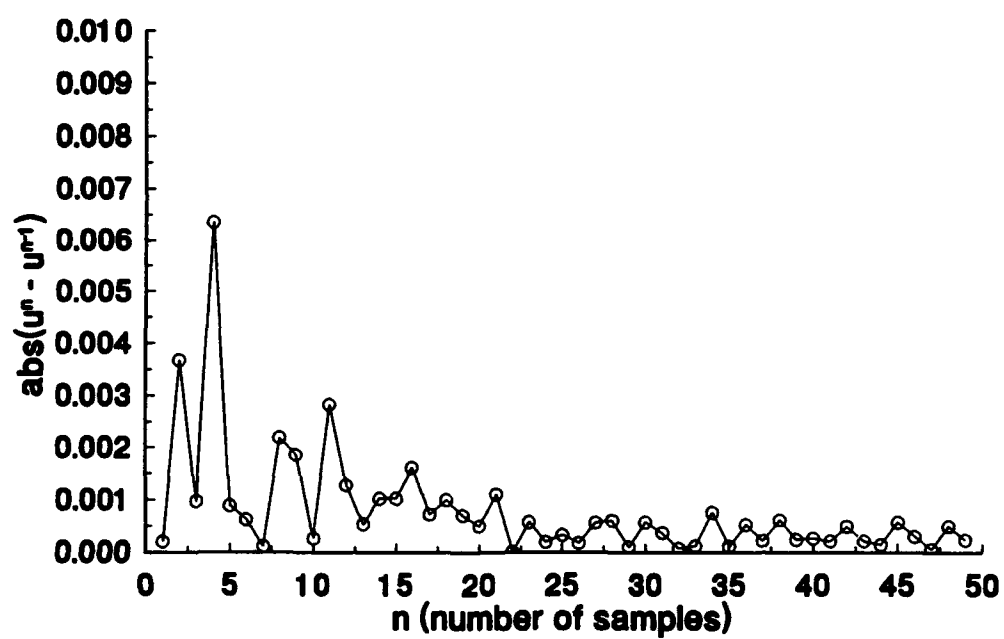


**Figure 3.9** Convergence of the ensemble average.

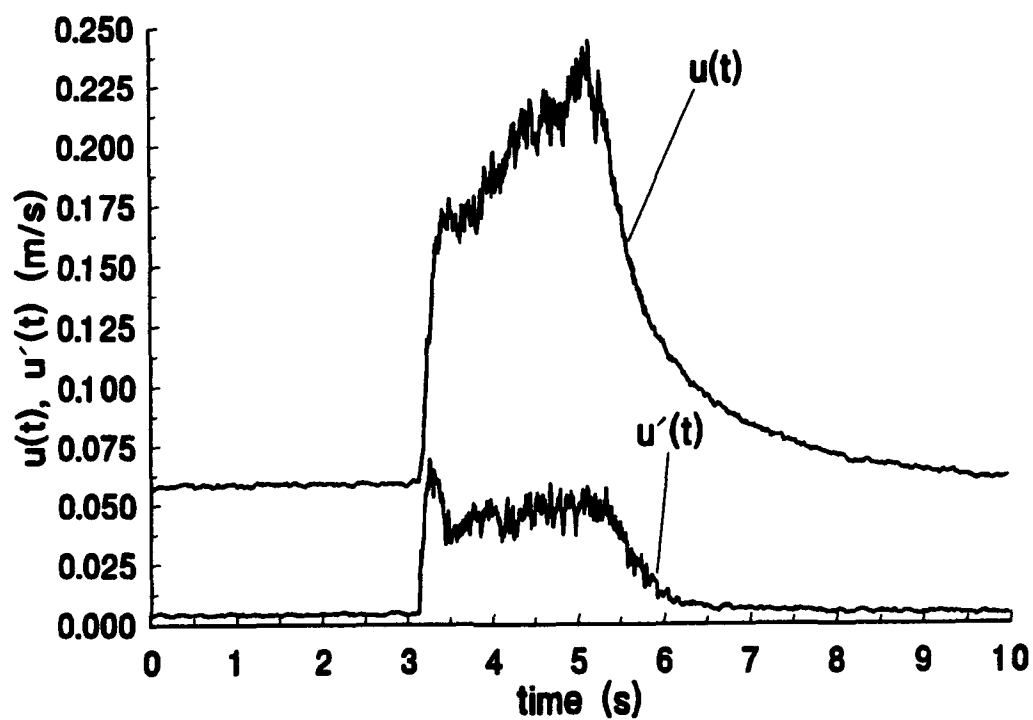


**Figure 3.10** Ensemble mean and variance of streamwise component of velocity at  $x=1.53\text{m}$ ,  $y=0.8\text{ mm}$ ,  $z=0\text{ m}$ ,  $U=40.6\text{ cm/s}$ .

for generating and acquiring velocity time series data from a single turbulent spot realization was as follows:

1. Pulse spot generator
2. Acquire analog out voltage for specified time (5-10 s) at 250 Hz
3. Reset spot generator (To ensure that the same pump motion was followed for each sample, the pump was reset after every generation event)
4. Allow flow to settle for 10 s so that the wake of the previous spot clears the measurement location in order to prevent spot interaction.

Each cycle took from 15 to 20 s.

A similar sequence of events was used to measure  $v_p$ , the potential flow velocity fluctuation normal to the wall. For this measurement the transmitting optics had to be rotated  $90^\circ$  so that the probe volume fringes were oriented parallel to the freestream. A Bragg cell was used to provide a frequency shift of 100 kHz in order to cause the interference fringe pattern to move vertically. This technique allowed the fluctuation of the normal component of velocity to be measured directly. The fluctuations in velocity were small (typically 1% of the freestream velocity) and individual realizations of the time series were noisy. The peak voltage fluctuation registered by the counter corresponding to the peak velocity amplitude was typically  $\pm 0.09$  volts from the DC value, or a fluctuation of  $\pm 32$  counts in the A/D conversion. Since the lowest fluctuation that the LV should measure is approximately 0.1% of the freestream velocity, the uncertainty in these measurements is



approximately 10%. Improved accuracy was obtained by subtracting the reading obtained without a spot present to eliminate any bias. The normal velocity measurements were made above the maximum turbulent spot height, at approximately  $y = 3.8\delta_L$ .

### 3.3 SPOT GENERATOR

Turbulent spots were generated by an impulsive jet ejected from a small hole in the test plate. A peristaltic pump driven by a stepper motor produces the jet. The pump was connected by 0.635 cm diameter copper tubing to the disturbance point, a 0.5 mm hole located on the plate centerline 53 cm from the test surface leading edge. The strength of the pulse may be varied by changing the motion that the stepper motor executes in driving the pump to produce the jet. The pulse strength for the experiments was determined by flow visualization, using a near-wall sheet of Fluorescein dye which issued from the most upstream dye slot. The number of motor steps for a disturbance pulse was varied and the resulting turbulent spots observed. The pulse strength was chosen by determining the lowest number of motor steps needed to produce a spot consistently. This was found to be a motor motion of 6 steps, or 0.03 revolutions. The impulsive jet introduced an additional 1.36 cc of water into the flow. An ensemble-averaged time trace of the disturbance signature is shown in Figure 3.11. The disturbance is the large, sharp peak, which is followed by smaller oscillations. These oscillations are typical of an impulsive jet generated by a square-wave pulse travelling through a long tube.

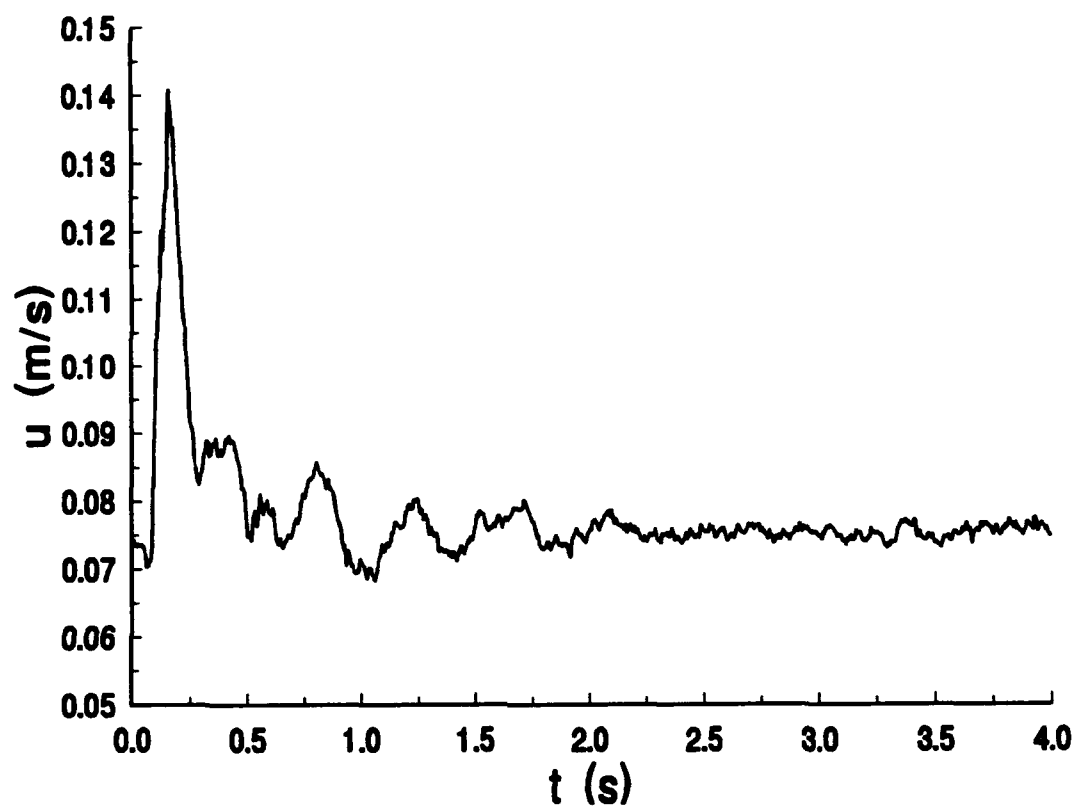


**Figure 3.11** Spot generator disturbance signature,  $x=0.53$  m,  $y=0.5$  mm,  $U=0.406$  m/s.

### **3.4 WATER CHANNEL QUALIFICATION**

#### **3.4.1 Water Quality**

To enable repeatable measurements the water channel must be kept as clean as possible. For LDA measurements it is desirable to minimize the number of particles in the water which are larger than a few microns in diameter. Particulate matter can also foul the honeycomb and any turbulence control screens. A filtration system was installed to remove large particles from the flow. The water was removed from the main flow loop through the boundary layer suction slot and re-injected just downstream, as shown in Figure 3.7. It was passed through a 5-micron filter to remove the undesired material. Despite this measure, a great deal of particulate matter, largely in the form of aluminum corrosion, was always present in the flow. This problem motivated periodic flushing of the entire system.

The corrosion of anodized aluminum surfaces was severe in some cases. Nowhere was this of more concern than the test surface. Small pinholes in the anodized surface allowed the test plate to corrode in small pits. The test surface had to be regularly treated to slow further corrosion. This treatment consisted of filling the pits with Devcon aluminum putty, sanding the putty flush to the surface and then applying two coats of car wax to the aluminum surfaces. The wax coats lasted up to two weeks before another coat was needed. This treatment was found to be effective in protecting the test surface.

### 3.4.2 Baseline Flow

LDA surveys revealed the quality of the baseline flow in the test section. Figure 3.12 shows the centerline laminar boundary layer profile in similarity coordinates compared to the Blasius profile. In addition, the freestream velocity was found to have very good streamwise and spanwise uniformity. An upper bound on the turbulence intensity of the freestream flow was found to be 0.3% by measuring the variance of the analog signal from the counter. In addition, there were regions of wall contamination which spread at approximately  $10^\circ$  from the wall, limiting the area over which a laminar boundary layer existed on the test surface, as seen in Figure 3.13. These regions, first noticed by Charters (1943), consisted of intermittent flow. The intermittency was more pronounced at lower freestream velocities. The apex of the triangle formed by the contamination wedges was located in the vicinity of the centerline. This point, denoted  $x_w$ , is the furthest downstream location for which uncontaminated centerline measurements may be taken. The variation in  $x_w$  with freestream velocity  $U$  is shown in Figure 3.14.  $U$  was found using the LDA and  $x_w$  was found by observing the most upstream location of the disturbance to a sheet of dye adjacent to the wall due to turbulent mixing.

### 3.4.3 Suggested Improvements

The recommended improvements to the water channel facility may be divided into two categories. These are the quality of the water and the quality of the flow.

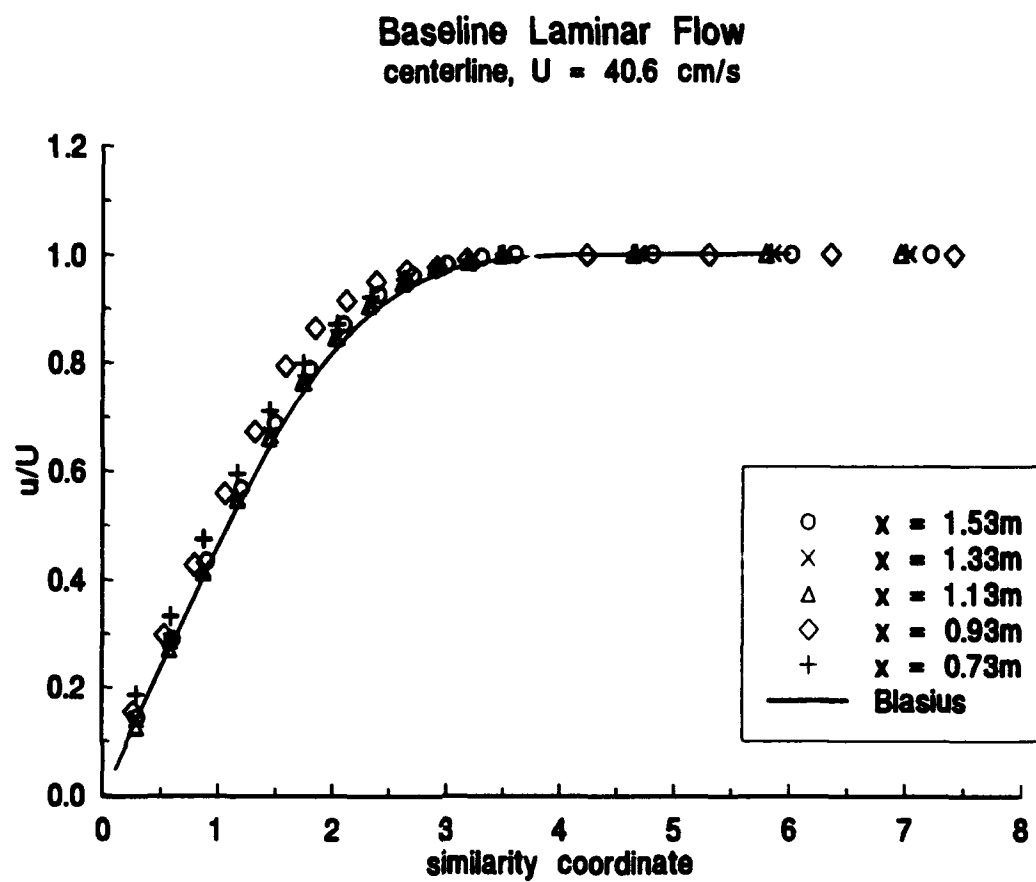


**Figure 3.12** Boundary layer profiles in similarity coordinates at  $x=73, 93, 113, 133$ , and  $153 \text{ cm}$  from the leading edge.

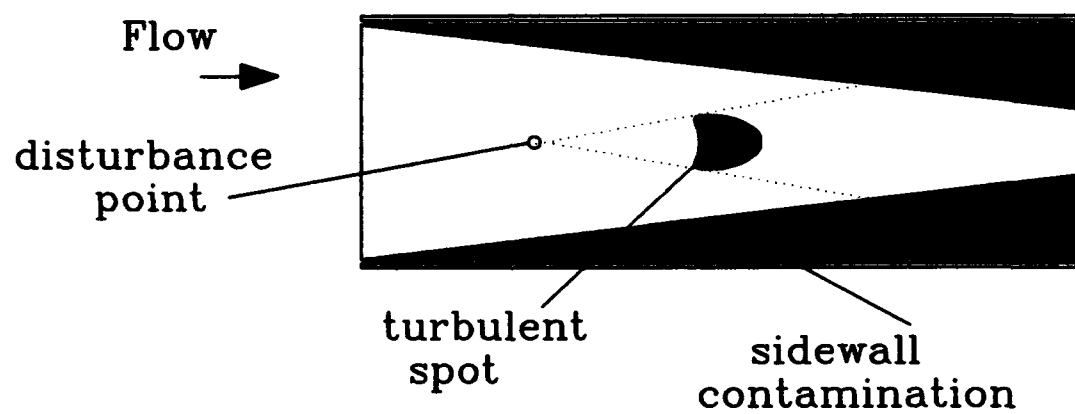


**Figure 3.13** Schematic of test plate flow regimes, showing the sidewall contamination.

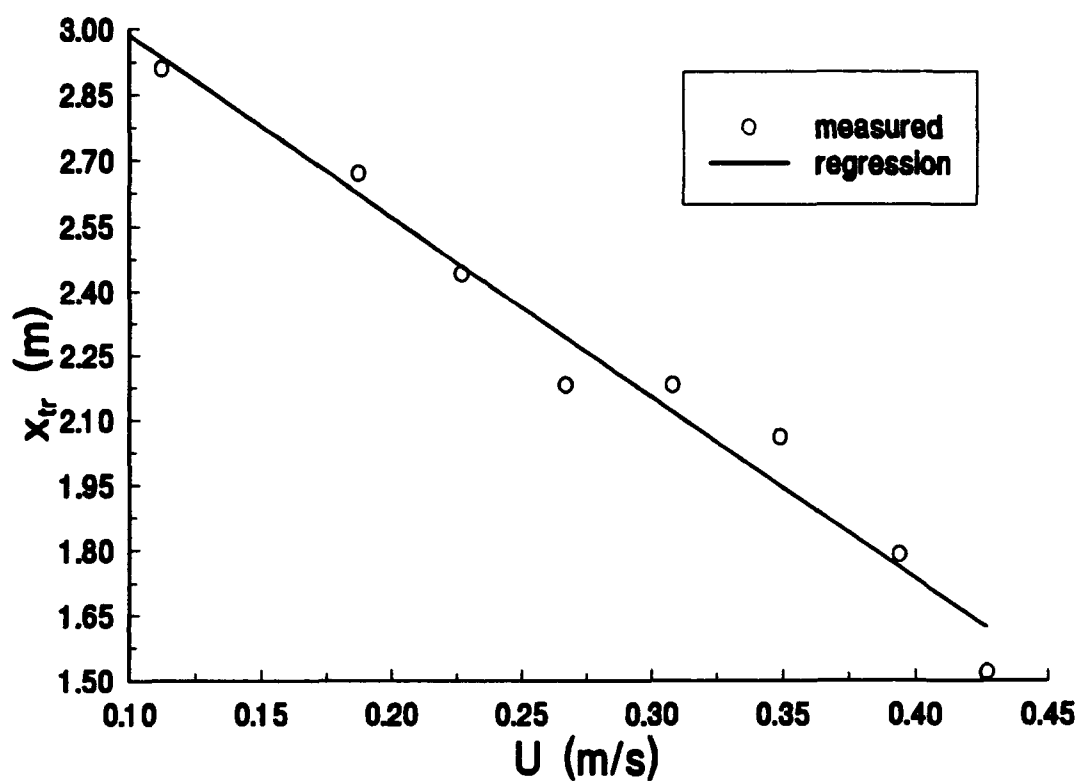


**Figure 3.14** Position of intersection of sidewall contamination wedges,  $x_{tr}$  as a function of  $U$ .

At present, experiments in the water channel are plagued by particulate matter in the flow. Although a filtration system has been installed, it has not been entirely effective. There are two possible reasons for this failure: 1) the filter pump is not powerful enough to produce the needed suction and 2) the access to the particulate matter is limited because the filtration in/outlets are located in the sidewalls rather than the floor of the lower leg diffuser. To remedy the first possibility, a larger pump should be installed. Access to a greater proportion of the flow would be a more ambitious undertaking, since it involves modifications to the flow passage structure. However, a more permanent (and expensive) approach is to replace all the aluminum surfaces in the flow loop with another material such as stainless steel that will not corrode.

Another improvement to flow quality would be the installation of a deaeration system. At present, a delay of two days is required between filling the channel and making measurements in order for the dissolved air to come out of solution. Some of this air becomes trapped in the lower parts of the return leg, where it is very difficult to remove. A deaeration system would reduce greatly this delay and would also make clearer video images possible for quantitative flow visualization using hydrogen bubble timelines (see Bruneau, 1992). It would also make possible the use of hot-film anemometry, which is more accurate for making turbulence measurements than LDV. At this time an effort to install a deaeration system is being undertaken.



The quality of the flow itself may be improved by the final installation of the turbulence control screens. Reduction of the particulates in the flow is absolutely necessary, however, before installation of the turbulence control screens is possible. These screens should reduce the turbulence level in the freestream, although with the present instrumentation, the improvement may not be measurable.

## **CHAPTER 4**

### **EXPERIMENTAL RESULTS AND DISCUSSION**

#### **4.1 EXPERIMENTAL CONDITIONS AND DATA PROCESSING**

##### **4.1.1 Experimental Plan**

To experimentally investigate the structure and development of a turbulent spot, following the objectives set forth in Chapter 1, measurements of the unsteady velocity field both inside and outside of the boundary layer were made during the passage of isolated turbulent spots and an interacting turbulent spot pair. The freestream velocity during all but one of these experiments was  $U=0.406$  m/s. An additional turbulent spot with  $U=0.19$  m/s was also investigated.

Unsteady streamwise velocity profiles were measured in order to calculate the local fluctuations in the mass flux deficit due to the turbulent spot. Five streamwise stations were used and were located at 20 cm intervals, as shown in Figure 4.1. For the isolated spot cases at  $U=0.41$  m/s, off-centerline measurements were made at three spanwise locations for each streamwise station. Unsteady velocity profiles were measured only on the centerline for the interacting spot cases. An additional profile was measured at  $x=1.75$  m on the centerline for  $U=0.19$  m/s. The  $z$ -coordinate for the measurements lay along rays originating from the generation point at angles of  $2.5^\circ$ ,  $5^\circ$ ,  $7.5^\circ$  from the centerline. In addition, the component of the velocity normal to the wall,  $v_n$ , was measured in the potential flow above the boundary layer. These measurements were made at the same  $(x,z)$  locations as the  $u$ -component measurements, at a height of  $3.67\delta_t$ . An extra off-centerline station was added for

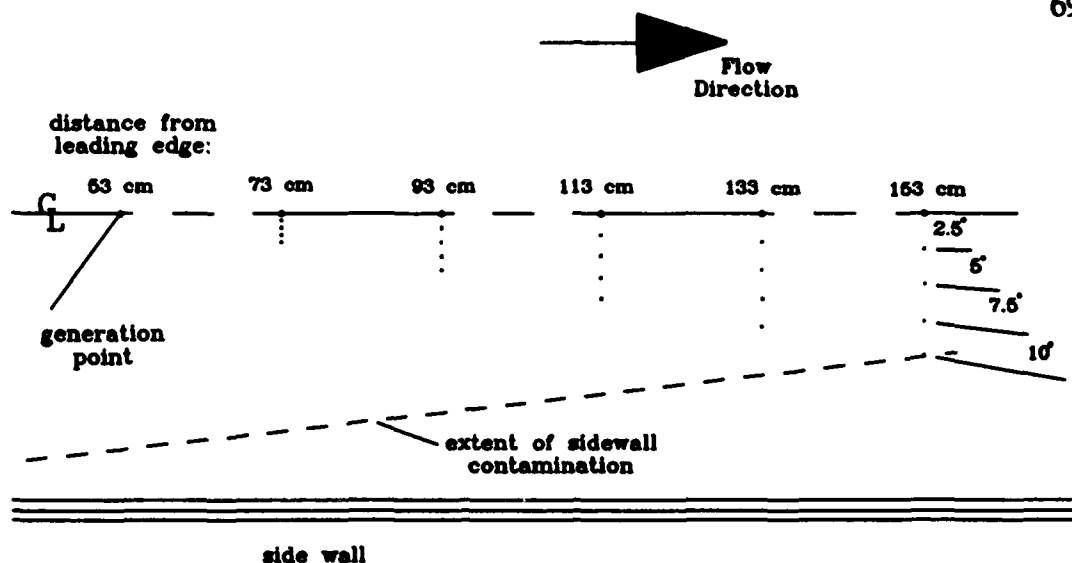


**Figure 4.1** Top view of locations for unsteady velocity measurements. Off-centerline points on rays through generation point at angles shown, measured from the centerline.

the  $v$ -component measurements along the ray through the generation point at an angle of  $10^\circ$  to the centerline. Both the isolated and interacting spot measurements used these locations for measuring  $v_p$ . The locations and type of measurement for all experiments are listed in Tables 4.1 - 4.3.

**Table 4.1** List of isolated spot u-profile experiments.

type of experiment	type of measurement	x m	z cm	U cm/s
isolated spot	u profile	73	0, 0.87, 1.74, 2.63	40.6
isolated spot	u profile	93	0, 1.76, 3.49, 5.27	40.6
isolated spot	u profile	113	0, 2.62, 5.23, 7.83	40.6
isolated spot	u profile	133	0, 3.49, 6.97, 10.53	40.6
isolated spot	u profile	153	0, 4.37, 8.72, 13.17	40.6
isolated spot	u profile	175	0	19.0

**Table 4.2** List of isolated spot direct normal velocity measurements.

type of experiment	type of measurement	x m	z cm	U cm/s
isolated spot	direct $v_p$	73	0, 0.87, 1.74, 2.63, 3.47	40.6
isolated spot	direct $v_p$	93	0, 1.76, 3.49, 5.27, 6.95	40.6
isolated spot	direct $v_p$	113	0, 2.62, 5.23, 7.83, 10.41	40.6
isolated spot	direct $v_p$	133	0, 3.49, 6.97, 10.53, 13.89	40.6
isolated spot	direct $v_p$	153	0, 4.37, 8.72, 13.17, 17.37	40.6

**Table 4.3** List of interacting spot u-profile measurements.

type of experiment	type of measurement	x m	z cm	U cm/s
interacting spots	u profile	93	0, 1.76, 3.49, 5.27	40.6
interacting spots	u profile	113	0, 2.62, 5.23, 7.83	40.6
interacting spot	u profile	133	0, 3.49, 6.97, 10.53	40.6
interacting spots	u profile	153	0, 4.37, 8.72, 13.17	40.6

#### 4.1.2 Data Processing

The event timing for the ensemble averaging was triggered on the spot generator disturbance pulse. The averaged unsteady velocity time series formed the basis for all subsequent calculations. The unsteady streamwise mass flux deficit for a given  $(x,z)$  location was calculated by integrating the ensemble-averaged velocity time series:

$$\frac{\text{MFD}(x,z,t)}{\rho U} = \int_0^H \left(1 - \frac{u(x,y,z,t)}{U}\right) dy \quad (4.1)$$

using the trapezoidal rule. The velocity normal to the plate,  $v_n$ , is related to  $\text{MFD}/\rho U$  according to:

$$\frac{v_n(x,z,t)}{U} = \frac{\partial}{\partial x} \frac{\text{MFD}(x,z,t)}{\rho U} - \frac{\partial}{\partial z} \int_0^H \frac{w(x,y,z,t)}{U} dy \quad (4.2)$$

On the centerline of a spot  $\partial w/\partial z = 0$  by symmetry (also shown by Wygnanski, *et al.*, 1976), so  $v_n$  there is simply the streamwise derivative of  $\text{MFD}/\rho U$ . In these calculations the spatial derivative in Equation 4.2 has been approximated by a temporal derivative according to the Taylor hypothesis:

$$v_n(x,z,t) \approx -\frac{1}{U} \frac{\partial}{\partial t} \left( \frac{\text{MFD}(x,z,t)}{\rho U} \right) \quad (4.3)$$

The derivative was calculated using a 4-point finite-difference scheme. It should be pointed out that another choice for the velocity in Taylor's hypothesis is to use the convection speed of the turbulent spot,  $U_c$ , which is later shown to be 76% of the freestream velocity. Using  $U$  rather than  $U_c$  results in a value for  $v_a$  which is 76% of the value obtained if  $U_c$  was used. However, since the interest is in the growth rate and the arrival times of the zeroes of  $v_a$ , the absolute magnitude is not an issue.

## 4.2 SINGLE SPOT MEASUREMENTS

### 4.2.1 Spot Growth

In order to quantify the growth of the isolated turbulent spot, the edges of the spot were determined based on a perturbation velocity criteria. The perturbation velocity,  $u_p$ , is defined as:

$$u_p(x,y,z,t) = \frac{u(x,y,z,t) - u_l}{U} \quad (4.4)$$

The velocity  $u_l$  corresponds to the velocity in the undisturbed laminar boundary layer which was determined by averaging the values of the first 100 time steps of the velocity trace, before the arrival of the turbulent spot. The perturbation velocity time traces were then low-pass filtered by averaging  $u_p$  at each time step with the values at the neighboring  $\pm 15$  time steps. This averaging window corresponds to a convolution of the velocity time series with a square pulse of unit height and of 0.124 s width. The velocity perturbation information was used solely to determine the gross scaling of the spot growth for comparison with other researchers. The edges



of the spot were located based on both a level and a slope criteria. By following the  $u_p$  time series in the positive time direction, the leading edge of the spot was detected by locating the time step at which:

$$|u_p| > 0.02 \quad \text{and} \quad \left| \frac{du_p}{dt} \right| > 3.0 \left( \frac{du_p}{dt} \right)_{\max} \quad (4.5)$$

where  $(du_p/dt)_{\max}$  is the maximum slope of  $u_p(t)$  in the initial, laminar portion of the time series. The trailing edge was found by the same method, but by following the time series from the last point and moving backwards in time. The spot envelope is formed by the locus of these points.

By plotting the position of the measurement station vs. the time of arrival of a given portion of the turbulent spot envelope at a streamwise station, a curve is constructed relating the feature's position to the time of its arrival. Such a plot is referred to as a celerity diagram. The slope  $dx/dt$  of these curves gives the celerity (convection velocity) of the feature of interest. The celerities for the leading and trailing edges of the turbulent spot were determined at the points nearest the wall. The virtual origin for the spot growth was also found from this information. By rescaling the spot envelope into similarity coordinates (Van Atta and Helland, 1980, and Itsweire and Van Atta, 1983):

$$\eta = \frac{y}{\delta_T}, \quad \delta_T = 0.37 \left( \frac{\nu}{U_\infty} \right)^{\frac{1}{3}} (x - 0.3933m)^{\frac{4}{3}}, \quad \xi = \frac{x - x_0}{U_\infty(t - t_0)}, \quad (4.6)$$

it can be seen in Figure 4.2 that for the last three stations ( $x = 1.13$  m,  $1.33$  m, and  $1.53$  m) the envelope collapses onto one curve, while the envelopes for the first two

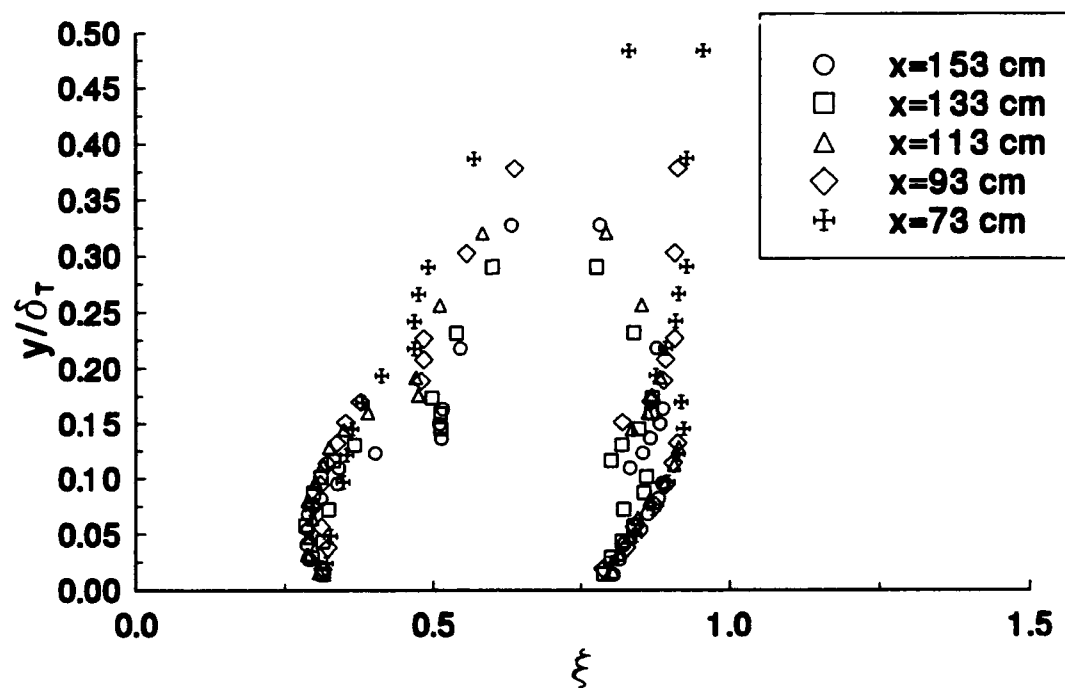


**Figure 4.2** Turbulent spot envelope in similarity coordinates,  $z=0$ ,  $U=40.6$  cm/s.

stations ( $x = 0.73$  m,  $0.93$  m) do not. This result is in agreement with the findings of Schubauer and Klebanoff (1956) and Wygnanski *et al.* (1976) who showed that the spot settles into a self-similar structure some distance downstream of the spot generator. This result also indicates that the present data include portions of the initial growth of the spot upstream of where similarity scaling applies.

#### 4.2.2 Unsteady Mass Flux Deficit, Normal Velocity

Figure 4.3 shows a typical trace of  $\Delta\text{MFD}/\rho U$  and  $v_n/U$  versus time. Superimposed on these traces is the 2% velocity perturbation contour (the locus of points for which the perturbation velocity  $u_p$ , described in Section 4.2.1, is  $\pm 2\%$ ) which shows the outline of the turbulent spot relative to the features of  $\Delta\text{MFD}/\rho U$  and  $v_n$ . At the time of arrival of the spot the value of  $\Delta\text{MFD}/\rho U$  increases rapidly to its highest peak. It then reverses direction and falls below zero to a negative peak. After this peak, the curve slowly approaches the initial state. A comparison of the  $\Delta\text{MFD}/\rho U$  curve and the spot envelope helps to explain this behavior. The maximum peak corresponds to the arrival of the maximum height of the spot, while the minimum peak corresponds to the trailing edge. The slow return to the initial state represents the "calmed region", first identified by Schubauer and Klebanoff (1956). This form is concordant with results shown by Wygnanski *et al.* (1976) and Antonia *et al.* (1981). Measurements taken at off-centerline locations show similar trends, but with a different phase and amplitude (Figure 4.4). At off-centerline locations  $\delta^*$  is not

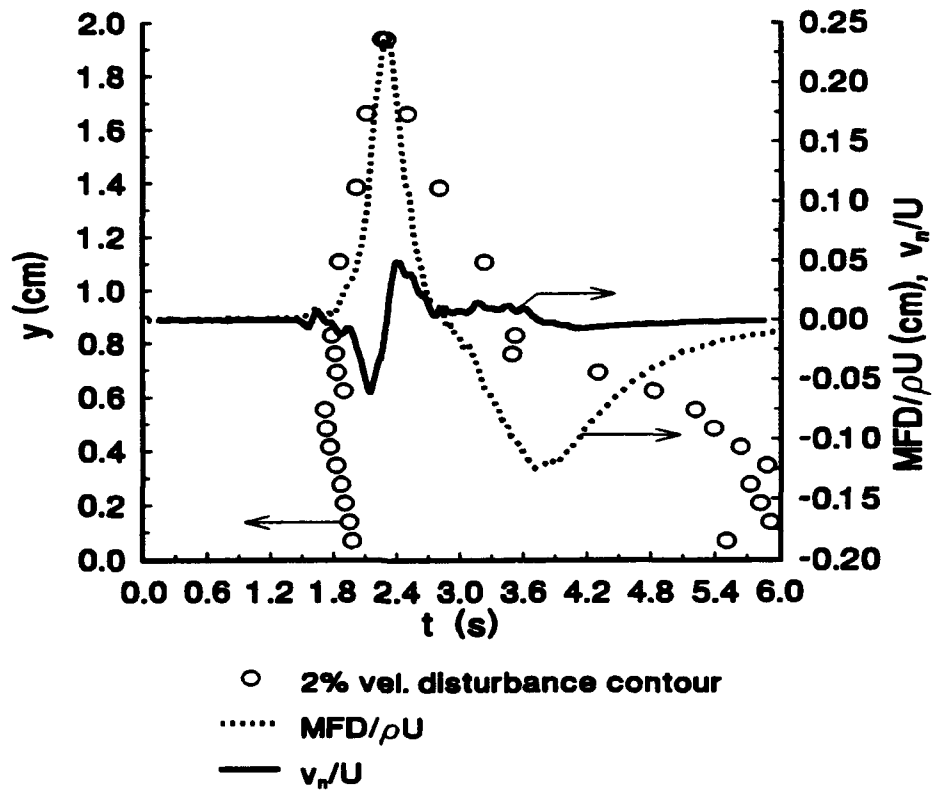


**Figure 4.3** Mass flux deficit and normal velocity fluctuations at  $x=1.13$  m,  $z=0$ ,  $U_\infty=40.6$  cm/s. Spot edge is also shown, denoted by 2% velocity disturbance contour.

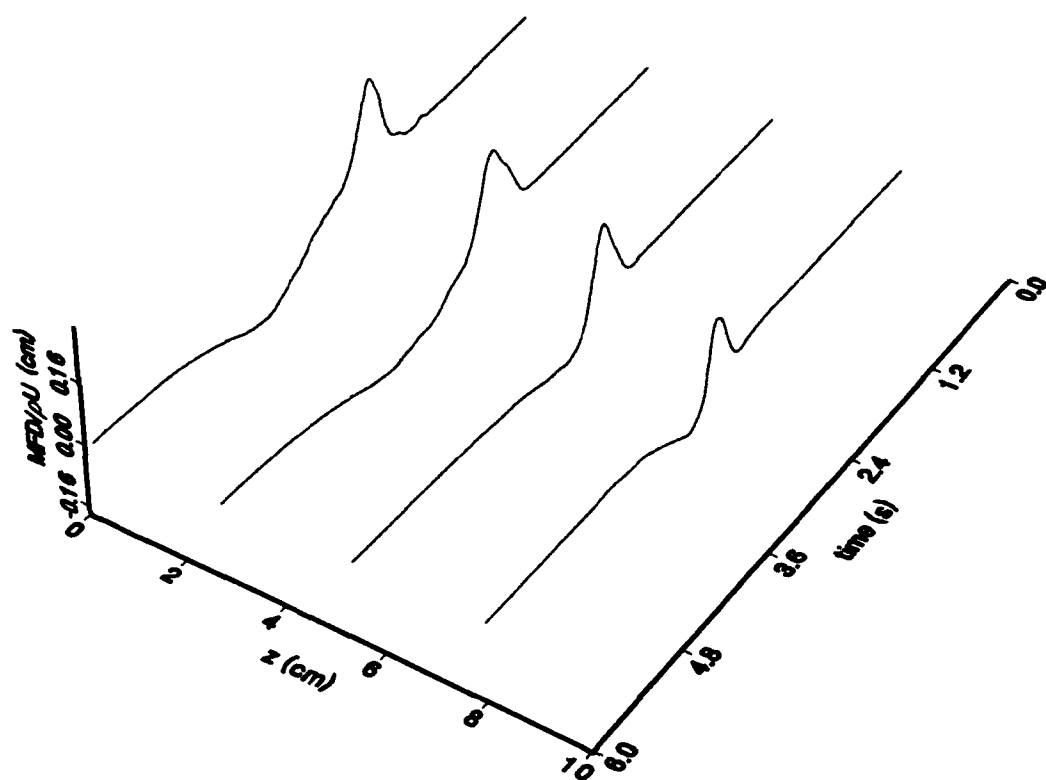


**Figure 4.4** Spanwise distribution of mass flux deficit at  $x = 1.13$  m from the plate leading edge.  $U = 40.6$  cm/s.

well represented by  $MFD/\rho U$  because there is an appreciable spanwise component of velocity of up to  $0.08 U$ , according to Wagnanski *et al.* (1976).

One of the unresolved issues concerning the character of the sound radiation from a transitional flow is the question of whether the flow is a monopole source or not. If it is the net mass flux normal to the wall caused by a turbulent spot should be nonzero for some instant. However, it is easy to argue that the normal mass flux fluctuation due to the spot must always be zero. If we consider two  $y$ - $z$  planes, infinite in the  $z$ -direction, far enough upstream and downstream of a turbulent spot that the flowfield fluctuation due to the spot is not felt, it is clear that the velocity profiles at these stations are those of the undisturbed laminar boundary layer. The amount of mass flux normal to the wall between these stations, which includes the effect of the turbulent spot, should be equal to the amount lost to the streamwise flow between these stations due to the growth of the laminar boundary layer. In other words, the net normal mass flux is the same as if the turbulent spot were not present, or, that the net normal mass flux fluctuation due to the presence of a turbulent spot is zero. Again, this demonstrates conclusively that the monopole strength of a turbulent spot is identically zero. An equivalent statement is that the integral of the mass flux deficit over the spot area at any instant is zero.

Knowing this property of the velocity field, a test of the measurement of the mass flux deficit fluctuation was carried by integrating  $\Delta MFD/\rho U(x, z, t)$  over  $x$  and  $z$  at a single instant. Because the mass flux deficit was measured at four  $(x, z)$  locations as a function of time, it was necessary to make use of a similarity

transformation of the data in order to obtain the mass flux deficit distribution over space for one instant. This was accomplished using the similarity transformation given by Equations 4.6. Data from the four velocity profiles taken at  $x = 1.33$  m were used to calculate the unsteady mass flux deficit. The integral over the  $x$ - $z$  plane was transformed to  $(\xi, \eta)$  coordinates and the integral calculated using the Trapezoid Rule in two dimensions. The result of the integration was 0.8% of the incoming mass flux, indicating that the mass flux deficit calculations based on the velocity measurements are accurate to that degree.

Figure 4.5 shows the mass flux deficit, normal velocity fluctuations, and 2% perturbation velocity contour for the profile taken at  $x = 1.75$  m,  $U = 0.19$  m/s. Note that the amplitudes of the peaks are larger than those for the higher speed case, consistent with the thicker boundary layer present in a lower speed flow. In addition, the total time for a spot passage is much larger. The overall shape of both the mass flux deficit and the normal velocity are similar to the higher speed case, but the peak values of  $v_n/U$  are larger and the decay of the mass flux deficit from the positive maximum to the negative minimum peak is much sharper. In addition, the small negative peak in  $v_n/U$  present in the higher speed case is barely visible in Figure 4.5. More discussion of the differences between these two cases is given in Section 4.2.3.

Further insight into the behavior of the unsteady  $\Delta MFD/\rho U$  may be gained by inspecting Figure 4.6, which shows the time series for  $\Delta MFD/\rho U$  and representative time series for the  $u$ -velocity in the boundary layer. Deep in the boundary layer the velocity undergoes a sudden acceleration upon the arrival of the spot leading edge.

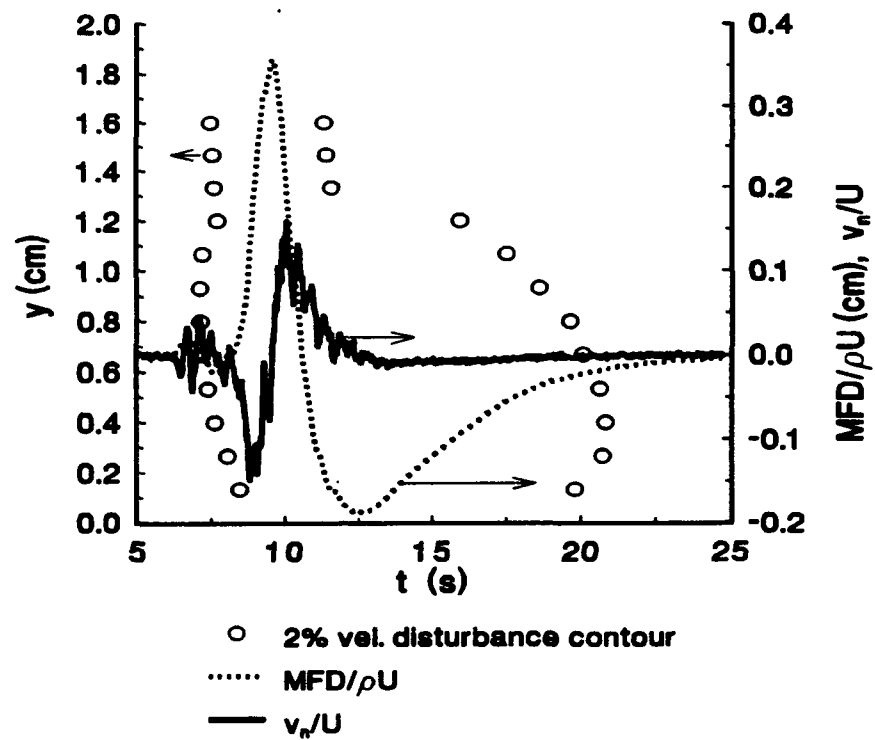


**Figure 4.5** Mass flux deficit and normal velocity ( $v_n$ ) fluctuations for  $x=1.75$  m,  $z=0$  m,  $U=19$  cm/s. Also shown is the spot edge, denoted by the 2% velocity perturbation contour.



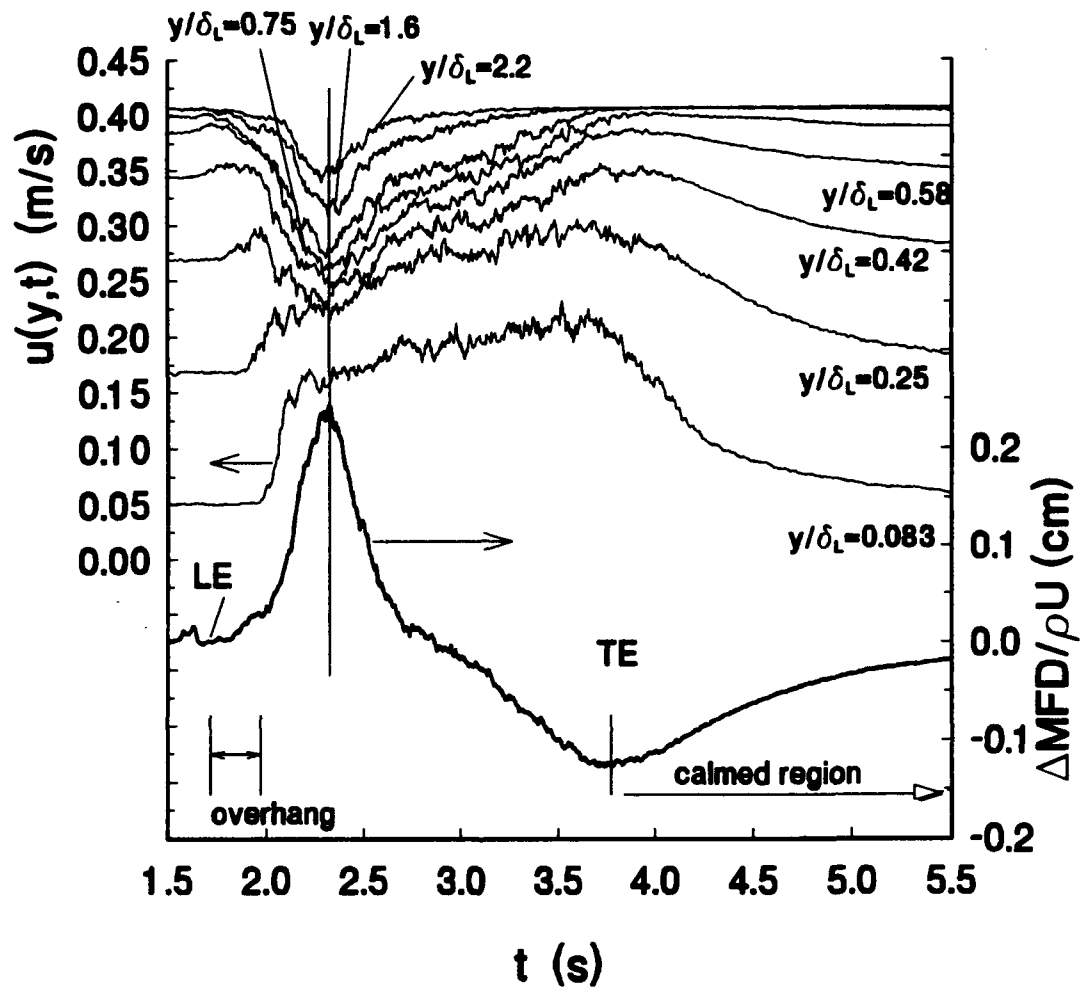


**Figure 4.6** Comparison of velocity perturbation contours with mass flux deficit time series,  $x=1.13$  m.

At greater distances above the wall this acceleration becomes less pronounced and is limited to the arrival of the spot leading edge, after which the flow decelerates. The initial velocity acceleration in the region corresponding to the undisturbed laminar boundary layer arrives at earlier times as the distance from the wall increases. The mass flux deficit increases from the undisturbed value, but only slightly, in this region of the spot which has been called the "overhang" region by Wygnanski *et al.* (1976). The deceleration of the flow following the overhang is related to the increase in the boundary layer height in the central part of the spot. Here the spot actually protrudes above the height of the surrounding laminar boundary layer.

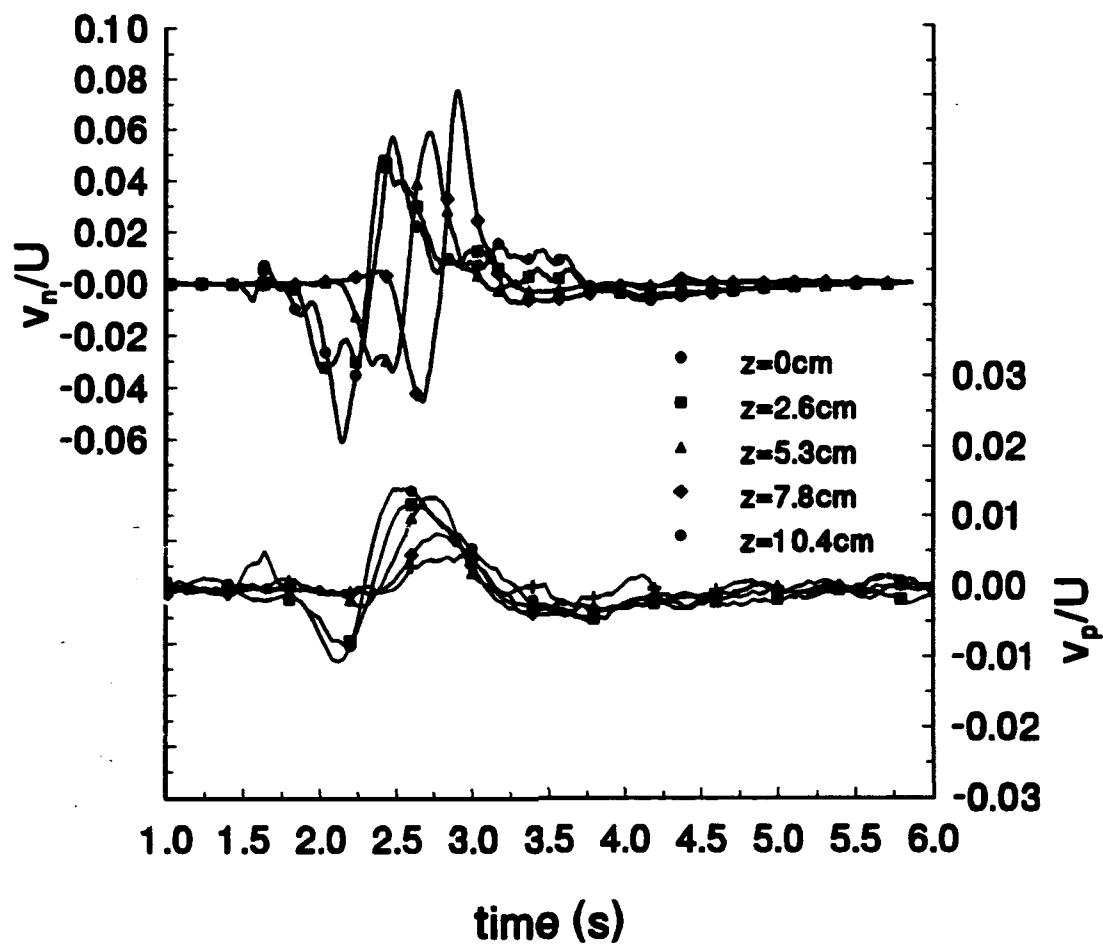
The deceleration of the flow outside the boundary layer corresponds exactly to the sharp, positive peak in the mass flux deficit. This maximum in turn corresponds not only to the minimum in the  $u$ -velocity peaks but also to the maximum spot height. After this maximum, the velocity increases again. The flow which was initially outside the laminar boundary layer quickly accelerates to its undisturbed value. The flow in the boundary layer continues to accelerate to a maximum which corresponds to the trailing edge of the turbulent part of the spot structure. This was also observed by Wygnanski *et al.* (1976). The mass flux deficit reaches its minimum at this point. Following the arrival of the trailing edge of the turbulent region, the flow is again laminar and it slowly decays to its undisturbed level.

The normal velocity on the spot centerline, calculated from the  $\Delta MFD/\rho U$ , is also shown for  $x = 1.13$  m in Figure 4.3. First, note that the normal velocity initially undergoes a rapid, negative fluctuation, followed by a positive peak which is at first

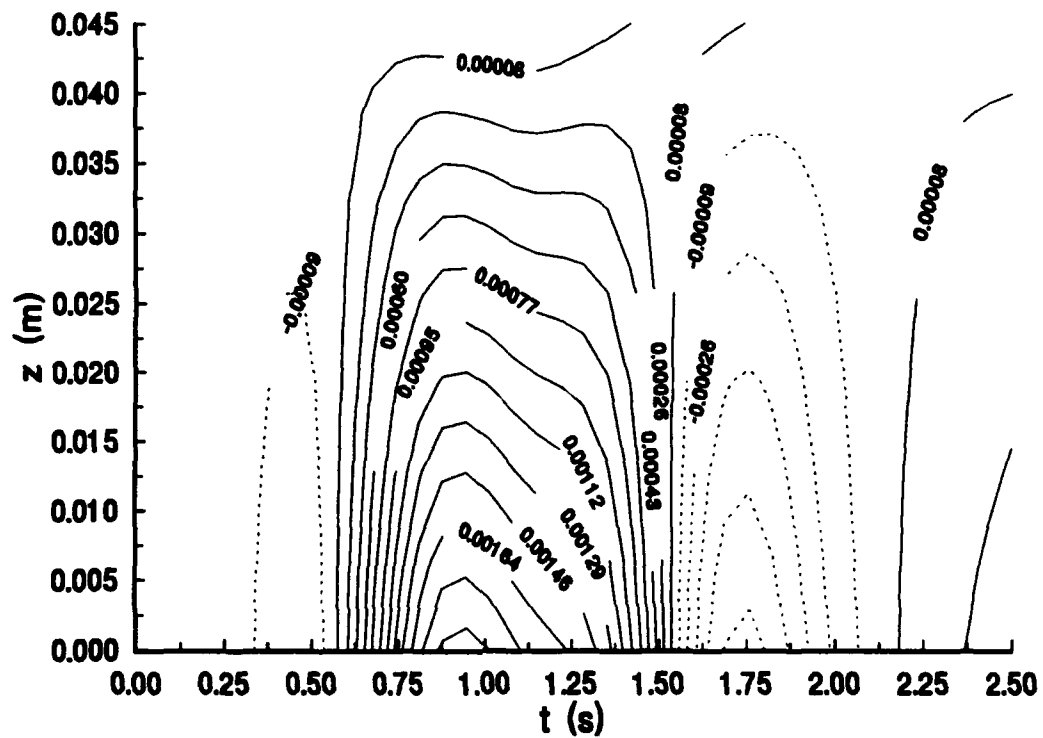
sharp and then more gradual. The positive peak is in turn followed by a shallow negative peak where the velocity slowly returns to its initial value. The two larger leading edge peaks are seen to be associated with the positive peak in  $MFD/\rho U$ , while the normal velocity fluctuations near the spot trailing edge are much smaller.

The spanwise variation in  $v_n$  is shown in Figure 4.7. Note how the negative peak at the spot leading edge occurs at later times as the distance from the centerline increases. For comparison the fluctuating velocity component normal to the wall,  $v_p$ , is also shown in Figure 4.7. It was measured directly at a height of  $3.67\delta_L$  above the wall. It is important to note that  $v_p$  is defined as the velocity normal to the wall minus the steady component of normal velocity due to the growth of the boundary layer. The overall shape of the time traces for  $v_n$  and  $v_p$  are similar. However, the phase of the curves is very different, especially when seen from a comparison of the spanwise distributions. The phase of  $v_p$  is preserved across the span of the spot, while for  $v_n$  it is not. Note that for  $v_p$  the negative leading edge peak disappears as the distance from the centerline increases.

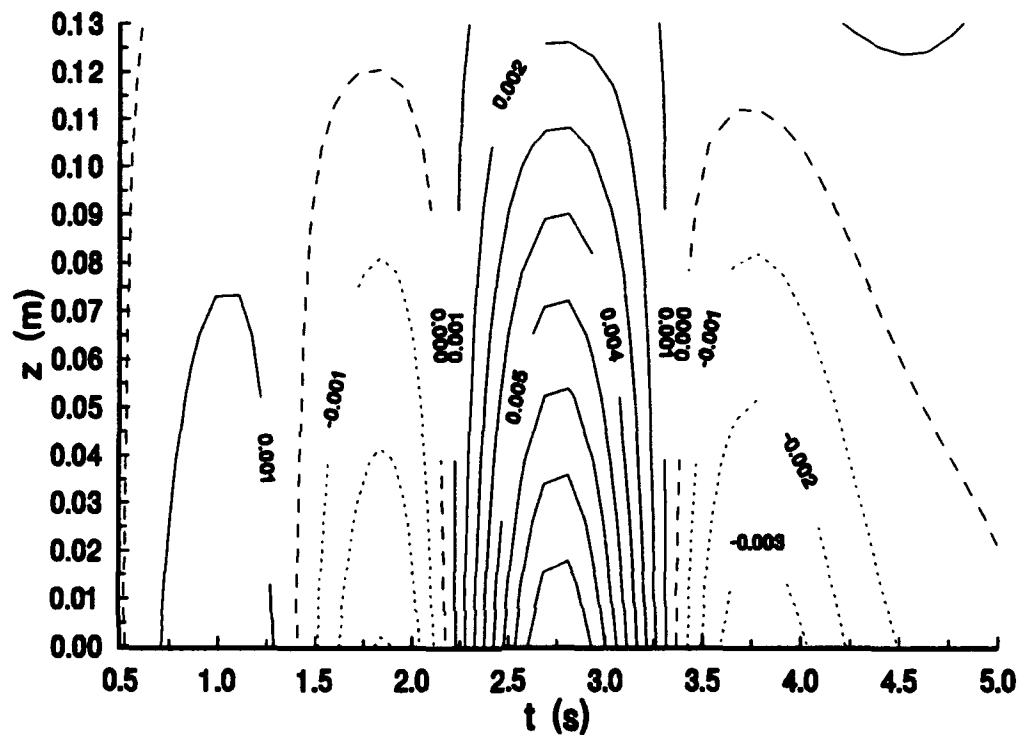
Contour plots of  $v_p$  at  $x=0.73$  m,  $x=1.13$  m, and  $x=1.53$  m are shown in Figures 4.8-4.10. The development of the potential flow disturbance can be seen clearly. Not only do the peaks in velocity grow in amplitude (the negative leading edge peak in particular), but the area covered by each peak also increases with downstream distance. This spatio-temporal behavior is important for the prediction of the radiated sound.



**Figure 4.7** Comparison of normal velocity deduced from mass flux deficit fluctuations to those obtained by direct measurement,  $x=1.13$  m.



**Figure 4.8** Contour plot of perturbation velocity normal to the plate measured at a height of  $3.67\delta_L$  for  $x = 0.73$  m,  $U = 40.6$  cm/s. Dotted lines denote negative velocity, solid lines positive.



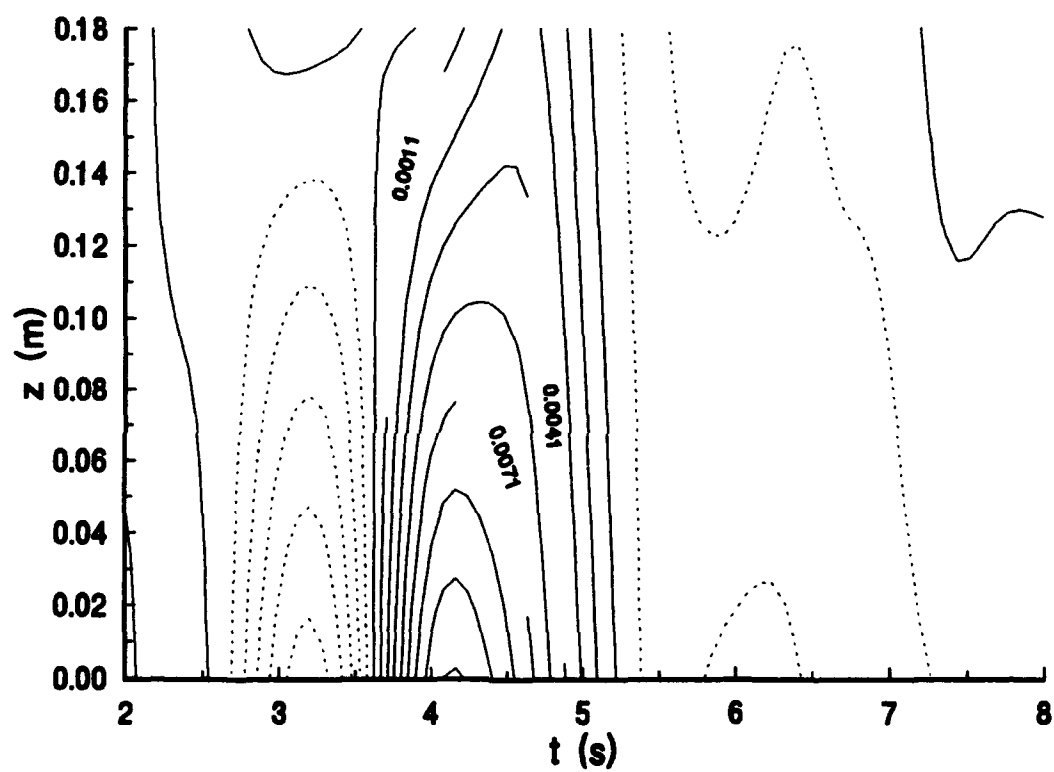


**Figure 4.10** Contour plot of  $v_p$  for  $x=1.53$  m,  $U=40.6$  cm/s. Dotted lines show negative contours, solid lines positive.

The discrepancy in the behavior between  $v_n$  and  $v_p$  can be explained by reference to Equation 2.3, where the freestream velocity potential fluctuations are expressed in terms of the integral of the normal velocity fluctuations due to unsteady displacement thickness fluctuations. The normal derivative of this equation yields the relationship between  $v_n$  and  $v_p$ . For this situation where the observer is in close proximity to the source, the retarded time may be neglected because  $r/c \rightarrow 0$ , resulting in the equation given by Van Atta *et al.* (1982):

$$v_p(x,t) = \frac{\rho}{2\pi} \int \int \frac{v_n(x',z,t) (y' - y)}{|x' - x|^3} dS' \quad (4.7)$$

They showed experimentally that the value of  $v_p$  on the centerline was dependent on the entire boundary layer flowfield through Equation 4.7. From this equation it is apparent that for a given instant the perturbation velocity in the freestream is influenced by the entire boundary layer flowfield at that instant, weighted by the third power of the distance from the "source" point in the boundary layer and the measurement point in the freestream. It is also necessary to recall that the method used here for calculating  $v_n$  does not consider the spanwise component of velocity (see Equation 4.3).

The streamwise variation of the unsteady mass flux deficit, measured at five  $x$  locations, is shown in Figure 4.12. The peak values clearly increase with  $x$ , while the peaks themselves spread apart and become less steep. The streamwise variation in the three parameters of interest, the magnitude of the mass flux deficit fluctuations,



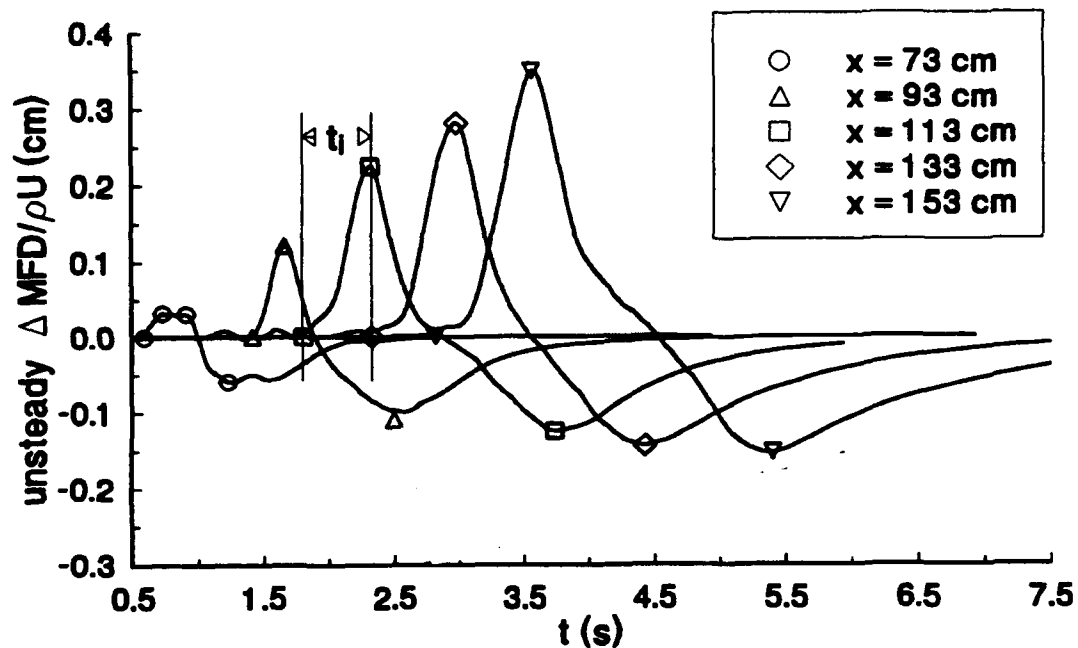


**Figure 4.11** Streamwise variation of unsteady mass flux deficit,  $z=0$ ,  $U_\infty=40.6$  cm/s. Rise time  $t_r$  is defined as the difference in times of arrival of leading edge and first positive peak.

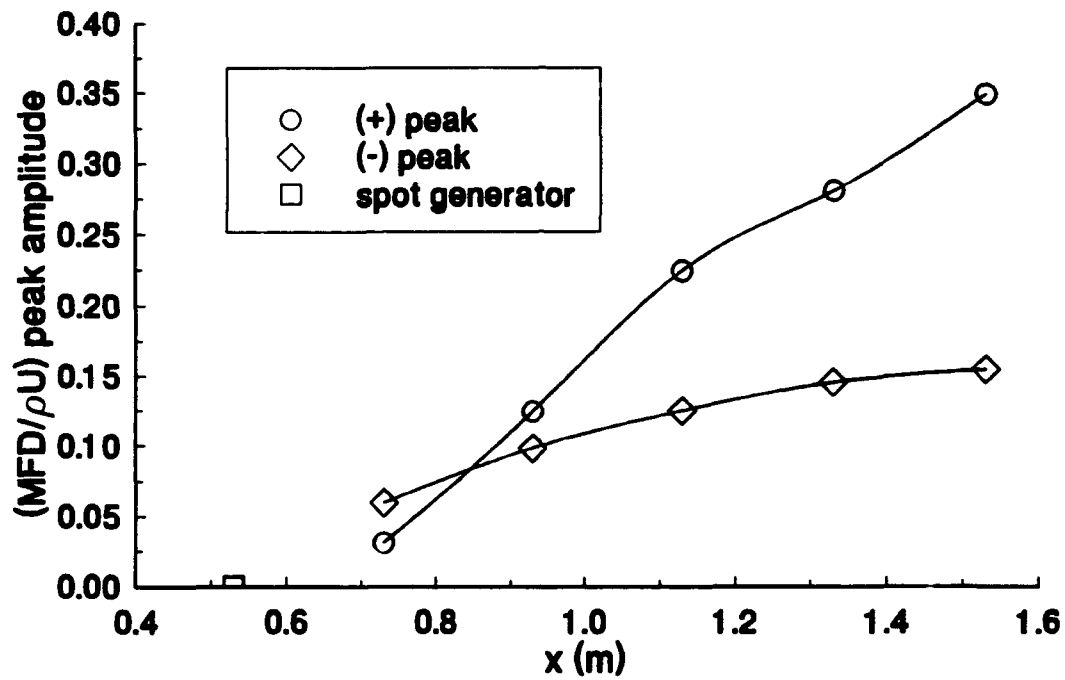


**Figure 4.12** Peak values of  $\Delta MFD/\rho U_\infty$  shown in Fig. 7. The (+) peak is the positive maximum and the (-) peak is the negative minimum shown in Figure 7.

the spot convection velocity, and the rise time may all be deduced from the information in Figure 4.10. Of considerable interest in analyzing the acoustics is the streamwise growth of the magnitude of the fluctuations of  $\Delta MFD/\rho U$  as the spot convects downstream. Figure 4.11 shows both the height of the positive peak and the difference in heights between the maximum and minimum of  $\Delta MFD/\rho U$  vs. streamwise location.

A celerity diagram of the principle features of the local  $\Delta MFD/\rho U$  curve is shown in Figure 4.13. The location of each measurement is plotted against the time of arrival of each of these features. The time of arrival of the leading edge was determined in a manner similar to that previously described which was used to locate the arrival of the edges of the turbulent spot, as described above. The time of arrival of the positive and negative peaks was found by locating the zeroes of the time derivative of the  $\Delta MFD/\rho U$  curve. A straight-line curve was fit to the data from the four downstream stations. These curves are also shown in Figure 4.13. Notice that these curves do not intersect at the spot generation location. This result is similar to the findings of other investigators and can be explained by the initial nonlinear growth of the turbulent spot. The convection speed for the given feature of interest is given by the slope of the straight-line curve. The spot arrival moves with a convection speed of  $U$ , the maximum peak with speed  $0.76 U$ , and the minimum peak with speed  $0.52 U$ . The last two convection speeds correspond well with the overall and trailing edge convection speeds of the isolated spot observed by Cantwell *et al.* (1978).

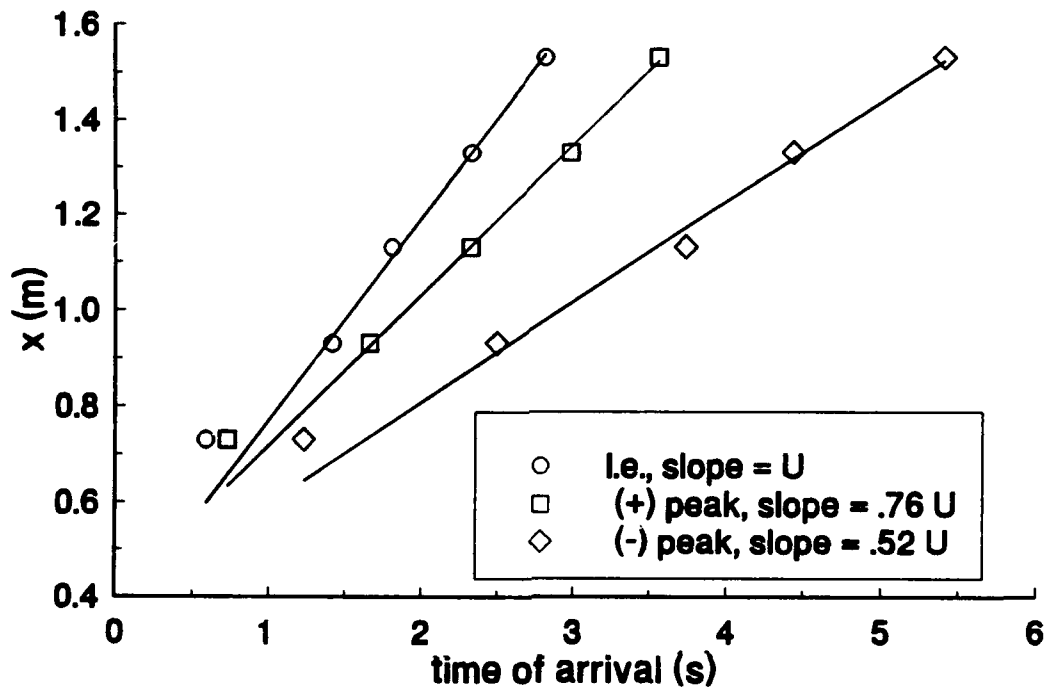


**Figure 4.13** Celerity diagram for  $MFD/\rho U$  shown in Fig. 7. Convection speeds are  $U$  for leading edge,  $0.76 U$  for (+) peak, and  $0.52 U$  for (-) peak.

The streamwise variation in the peak amplitudes of the two large normal velocity peaks are shown in Figure 4.14. Both the positive and negative velocity peaks increase with  $x$ , levelling off at  $x \approx 1.13$  m from the plate leading edge. The most intense normal mass flow fluctuation occurs downstream of this location. The slopes of these curves are greatest in the most upstream portion of the intermittent region, indicating that the rate of change of the normal mass flux is greatest there.

#### 4.2.3 Rise Time Estimates

The  $\Delta MFD/\rho U$  time traces clearly show that the rise and fall times which characterize the large-scale fluctuation in displacement thickness are very different from one another. These two parameters, which we name  $t^+$  (rise) and  $t^-$  (fall), are deduced from the celerity diagrams. The rise time for a given  $(x, z)$  location is considered to be equal to the time at which the maximum peak arrives minus the time at which the spot arrives (Figure 4.10). Similarly, the fall time is defined as the difference in the arrival time of the maximum and minimum peaks. The nondimensional rise time,  $U_c t^+/\Delta x$ , identified by Lauchle (1981) as controlling the high-frequency content of the radiated sound spectrum, may be estimated using these parameters. However, in order to estimate the non-dimensional rise time a transition zone length is needed. An estimate of the transition zone length  $\Delta x$  was obtained using the correlation (Josserand and Lauchle, 1990):

$$Re_{\Delta x} = 17 Re_{x_0}^{0.8} \quad (4.8)$$

with  $x_0 = .53$  m (spot generator location). This correlation predicts  $\Delta x \approx 77$  cm for

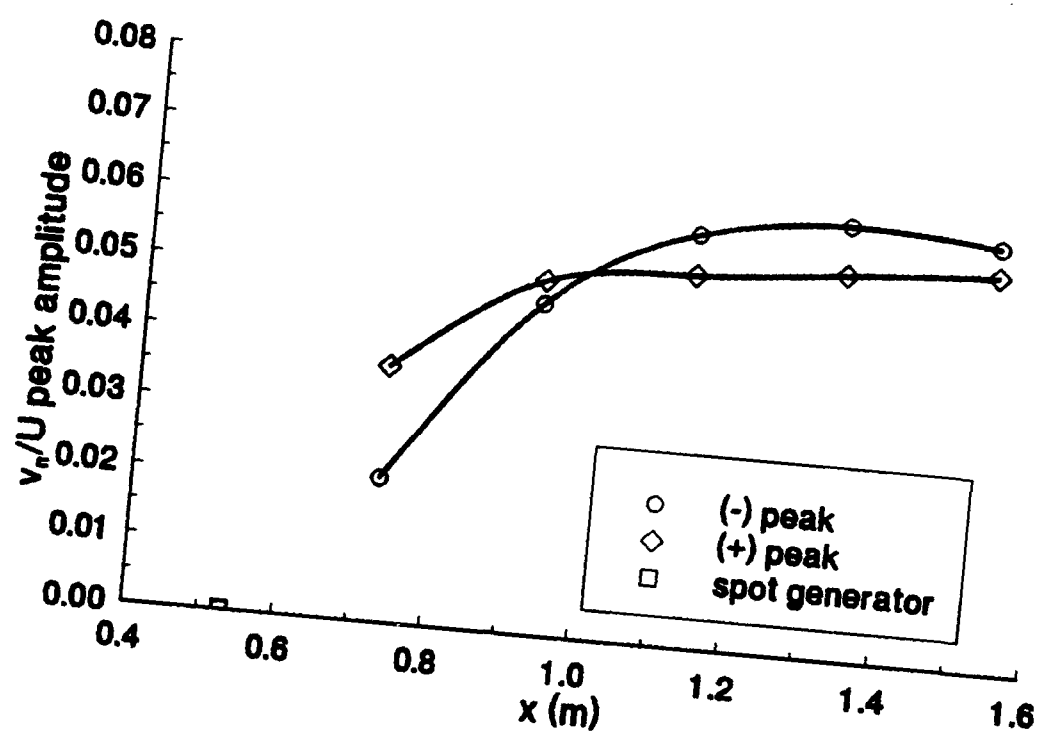


Figure 4.14 Streamwise variation of peak values of  $v_r$  on the spot plane of symmetry,  $U=40.6$  cm/s.

$U=40.6$  cm/s, and  $\Delta x \approx 90$  cm for  $U=19$  cm/s. A corresponding normalized transition zone streamwise coordinate,  $\zeta$ , may be defined by:

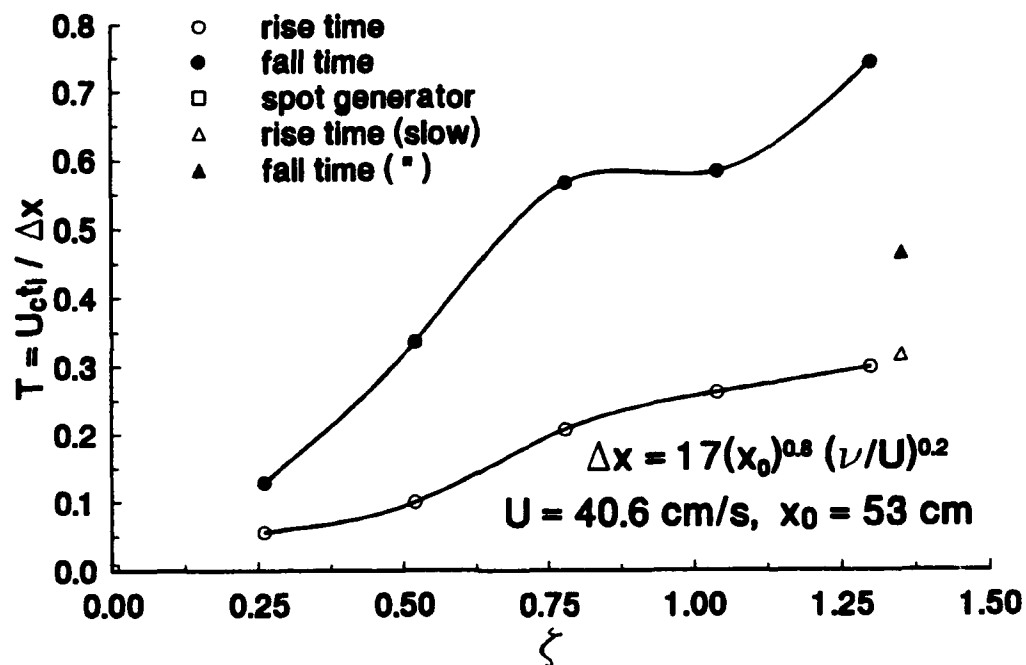
$$\zeta = \frac{(x - x_0)}{\Delta x} \quad (4.9)$$

Figure 4.14 shows how  $U_c t / \Delta x$  increases with  $\zeta$ . The ranges of the normalized rise and fall times for the 40.6 cm/s spot are:

$$0.06 < \frac{U_c t^+}{\Delta x} < 0.30 \quad 0.13 < \frac{U_c t^-}{\Delta x} < 0.74 \quad (4.10)$$

Figure 4.15 shows a clear monotonic increase in the magnitude for both the rise and fall times. From these results it can be seen that, for an isolated turbulent spot, the rise time of the intermittent fluctuation is always less than the time for the spot to traverse the intermittent zone. This is especially true for the upstream portions of the intermittent zone. The increase in the rise/fall times is due to the growth of the streamwise extent of the spot and seems to indicate that the mass flux normal to the plate decreases with  $x$ . As shown in Figure 4.10, the magnitude of the displacement thickness fluctuation *increases* with  $x$ , which implies a more intense local fluctuation in  $v_x$ . The balance between these two effects explains the levelling off of the peak normal velocity shown in Figure 4.13.

Perraud (1989) compared an estimate of the wall pressure spectrum in the laminar portion of the boundary layer upstream of the transition region with measured wall pressure spectra. The only pressure disturbances presumed to be measured in the laminar portion of the boundary layer are those which propagate as sound from



**Figure 4.15** Nondimensional rise time vs. nondimensional position relative to beginning of transition zone.  $\Delta x$  is given by result of Josserand and Lauchle (1990). "Slow" spot result is for  $U=19 \text{ cm/s}$ .



other regions of the flow. The experiments were carried out on a body of revolution in air. The spectral estimates were made using the approach of Lauchle (1981) for  $T=0.05$  and  $T=0.15$ . These estimates were found to bracket the measured spectrum well, except for some low-frequency peaks which were attributed to Tollmien-Schlichting waves. The range of  $T$  from the study of Perraud (1989) agrees well with that found in our measurements of the rise time. This correspondence suggests that the flow measured here should exhibit similar pressure behavior.

Also shown in Figure 4.14 are the rise and fall times for the mass flux deficit of a turbulent spot at  $U=0.19$  m/s,  $x=1.75$  m from the leading edge. Note that  $T^+$  seems to follow the trend for the higher velocity case, while  $T^-$  does not. This result may indicate that  $T^+$  is insensitive to the Reynolds number. Wygnanski *et al.* (1982) showed that the streamwise growth rate of a turbulent spot was sensitive to the Reynolds number based on the undisturbed flow displacement thickness at the generator location,  $(Re_{\delta^*})_{gen}$ . For the two cases given here,  $(Re_{\delta^*})_{gen}$  was equal to 537 and 797 for  $U = 0.19$  m/s and 0.41 m/s, respectively. The ratio of the trailing edge convection speed to the freestream speed was found to decrease with an increase in  $(Re_{\delta^*})_{gen}$ . However, the leading edge and spot maximum heights were found to be insensitive to Reynolds number. The spot leading edge and maximum height correspond to the leading edge and positive maximum of the mass flux deficit, while the spot trailing edge corresponds to the negative mass flux deficit peak, as shown in Figure 4.5. Since the rise and fall times are related to the convection speeds of these features of the mass flux deficit, it follows that the nondimensional rise time should

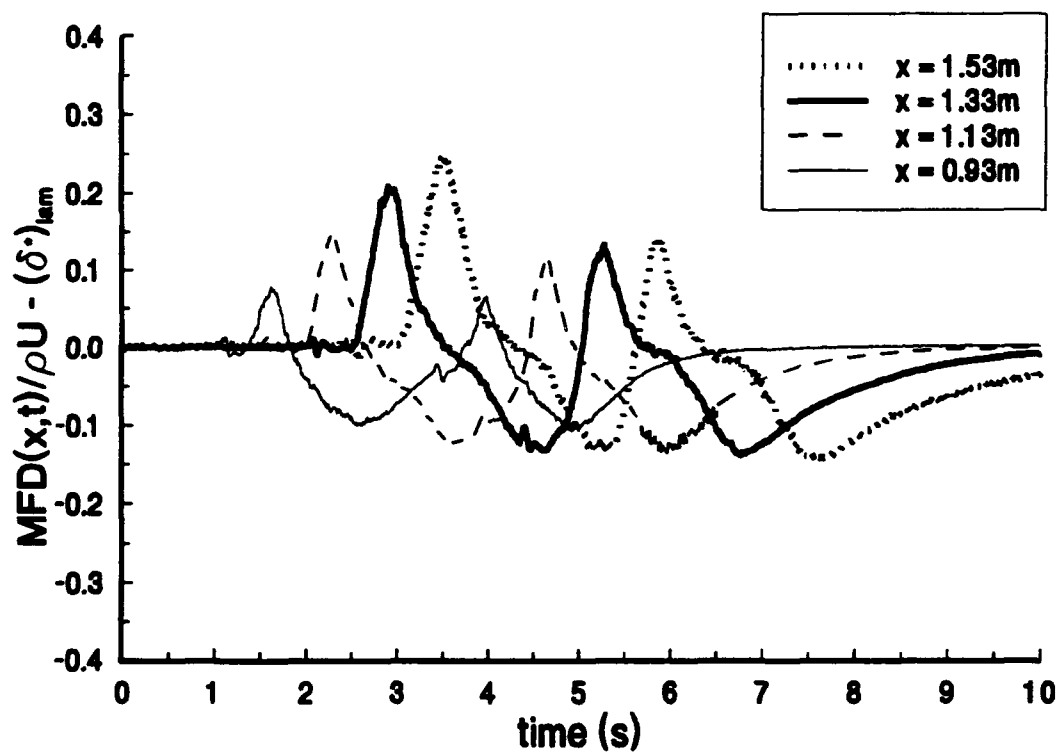
be insensitive to  $(Re_{\delta^*})_{cen}$ , while the nondimensional fall time should decrease with  $(Re_{\delta^*})_{cen}$ , which is agreement with the observations presented here. Further investigation should more strongly substantiate this assertion.

### 4.3 INTERACTING SPOT MEASUREMENTS

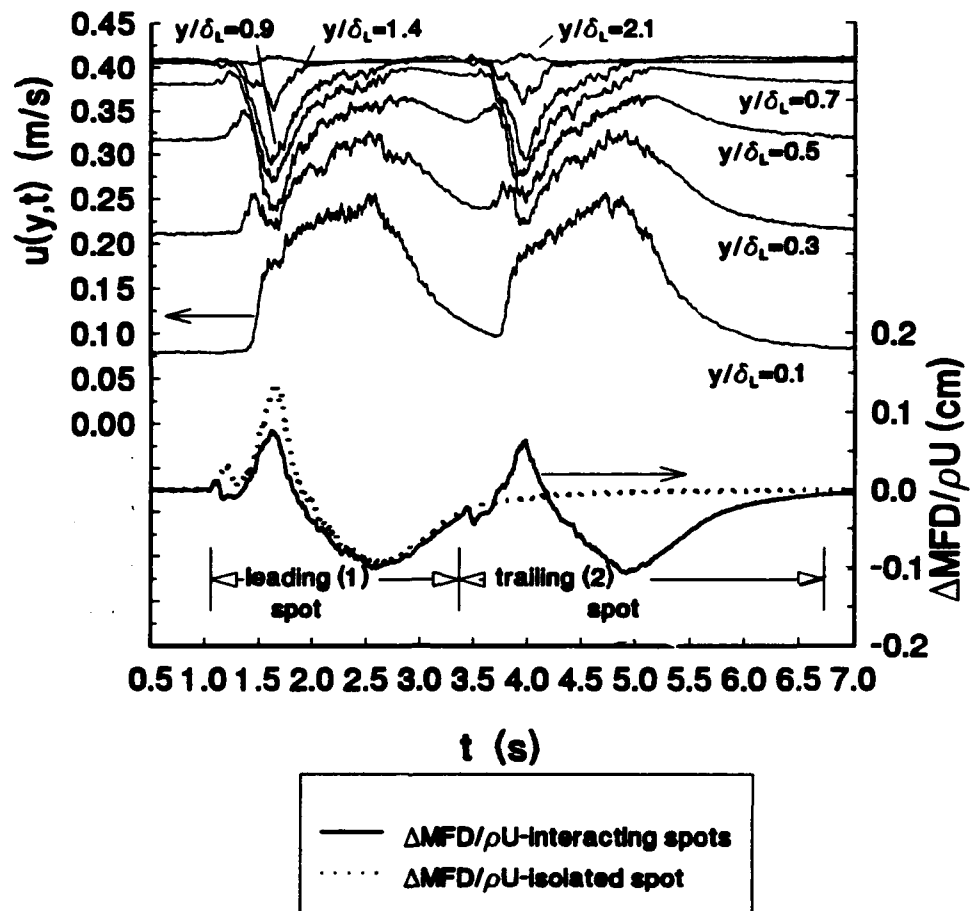
#### 4.3.1 Unsteady Mass Flux Deficit, Normal Velocity

Figure 4.16 shows the streamwise development in the mass flux deficit on the centerline for the interacting spot case. The behavior of each spot at the upstream stations is much the same as for two independent spots, except that the mass flux deficit positive peak for the second spot has a reduced amplitude. As the second spot catches the first, the growth of the mass flux deficit positive peak is attenuated relative to the peak for the first spot. The second spot leading edge and the first spot trailing edge are just meeting at  $x=1.33$  m, and have merged at  $x=1.53$  m.

Figures 4.17 and 4.18 show the relation between the unsteady velocity field and the mass flux deficit for  $x=0.93$  m and  $x=1.53$  m. Recalling the discussion concerning Figure 4.5, these comparisons show how the presence of the first spot affects the development of the velocity field, and hence the mass flux deficit, of the second spot. For the case  $x=0.93$  m, the two spots are seen to be distinct, although the leading edge of spot 2 has encroached on the calming region of spot 1. The  $\Delta MFD/\rho U$  positive peak of spot 2 is attenuated compared to that of spot 1. The corresponding attenuation of the velocity minima in the upper regions of the spot may be seen in Figure 4.16. Another way of stating this result is that the second spot has



**Figure 4.16** Streamwise variation of unsteady  $\Delta MFD/\rho U$  for interacting spots at four  $x$ -locations.



**Figure 4.17** Comparison of the velocity field inside the interacting turbulent spots and the corresponding mass flux deficit for  $x=0.93$  m. The isolated spot mass flux deficit is shown for reference.

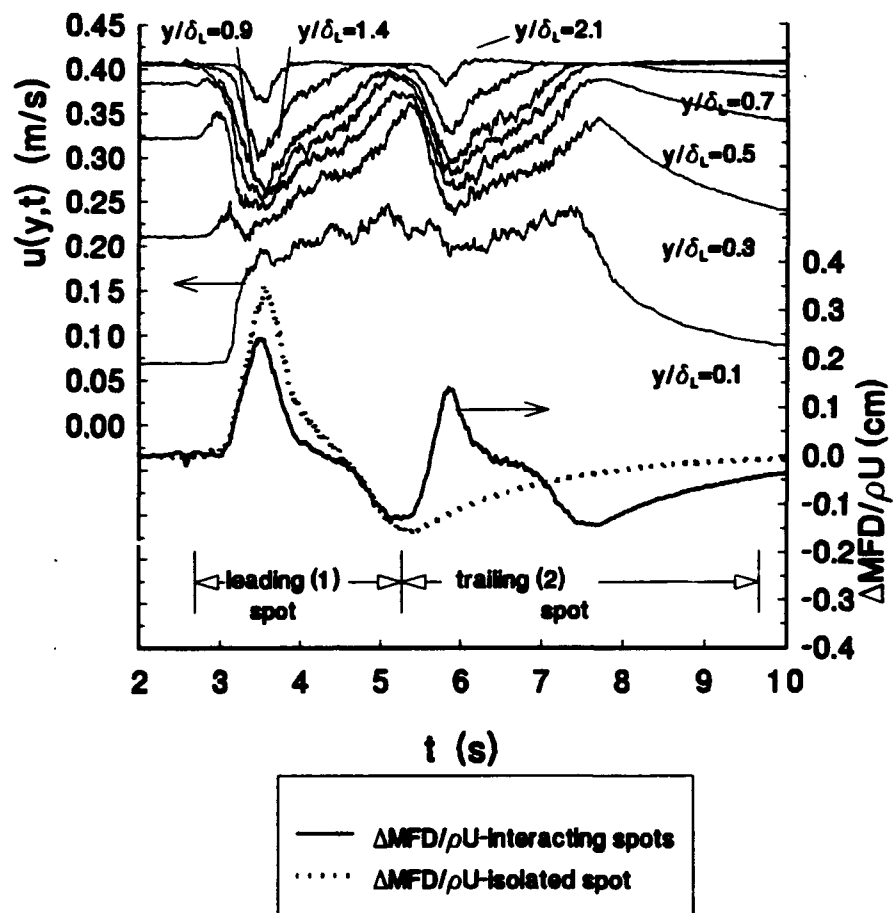


**Figure 4.18** Comparison of velocity traces with mass flux for interacting spots at  $x=1.53$  m. The leading edge of spot 2 has merged with the trailing edge of spot 1, as indicated by the disappearance of the overhang region in spot 2.

a lower maximum height than the first. This situation is even more pronounced in Figure 4.17, which shows the interaction for  $x=1.53$  m. Here it is clear that the initial acceleration of the flow at the spot leading edge, which characterizes the spot overhang region, has vanished in spot 2 due to its merging with spot 1. Although the spots have merged at this location, the two spots still have distinct structure: the velocity minima and maxima are still clearly identifiable, as are the corresponding features of  $\Delta MFD/\rho U$ , albeit with some modification in amplitude. Whether or not the identities of the spots would become blurred further downstream is not clear at this point and motivates further study.

A relevant question is how the spot convection velocity is modified by the interaction. To answer this question celerity diagrams for the interacting spots were constructed using the method described in Section 4.2.2. These are shown in Figure 4.19. The spot convection speed is given by the slope of the curve corresponding to the positive  $\Delta MFD/\rho U$  peak. It is clear that the convection speed has not been altered significantly by the interaction.

#### 4.3.2 Rise Time Estimates

Rise time estimates for the interacting spot case were made as described above in Section 4.1.2. Figure 4.20 shows the results. The same trends and orders of magnitude that held for the isolated spot case are clearly seen. These results are not surprising given that the rise and fall times are defined as the difference between the

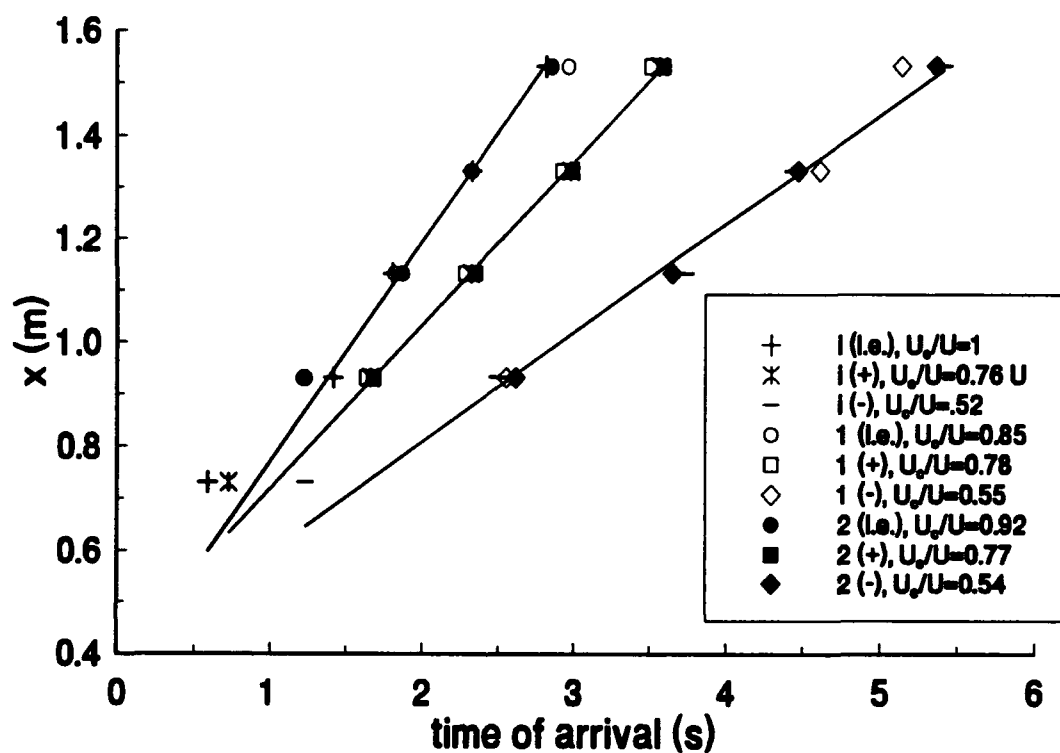


**Figure 4.20** Celerity diagrams for interacting spot cases. Spot 1 is the first generated. 2 denotes second spot and  $i$  denotes isolated spot case. Arrival time defined relative to generation time.

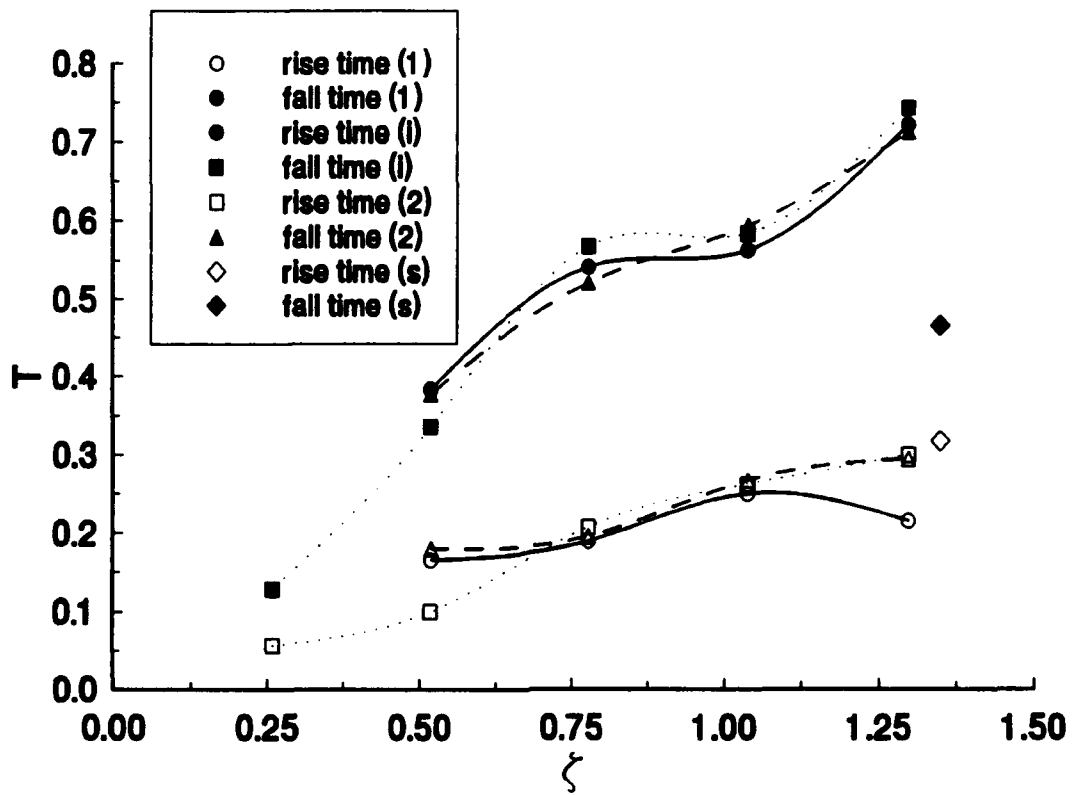


**Figure 4.20** Nondimensionalized rise times for the interacting spot case. The isolated spot case results are shown for reference.



arrival times of the various features of the spot and these have not been seriously modified by the interaction between the two turbulent spots.

## **CHAPTER 5**

### **ESTIMATION OF SOUND RADIATION**

The measurements described in Chapter 4 may be used to estimate the direct acoustic emissions from a single turbulent spot and a weakly interacting spot pair. The results of these cases may also be used to estimate the sound radiation from a naturally occurring transition region after making some simplifying assumptions. The estimation of the sound radiation is carried out in the spirit of the Liepmann analogy, where it is related to the unsteady normal velocity distribution on a surface outside the boundary layer. By observing the effect of a turbulent spot passage on the normal velocity distribution on this surface, some conclusions may be drawn about the nature of the acoustic source. These observations and the experimental data may then be used to provide a quantitative estimate of the sound radiation from a turbulent spot. Finally, the assumption that the displacement thickness is realistically represented by an intermittency-weighted form hypothesized by Lauchle (1981) and others is evaluated.

#### **5.1 SOUND RADIATION FROM AN ISOLATED TURBULENT SPOT**

In considering the sound radiation from a single turbulent spot, two general statements may be made concerning the nature of the acoustic source by inspection of the data presented in Chapter 4. The first is that the source is compact, given the low flow Mach number. For this reason, the retarded time differences  $x'/c$  in the argument of the integrand of Equation 2.6 may be neglected.

The second statement that can be made about the nature of the acoustic source follows from the incompressibility of the source flow. Incompressibility dictates that the net instantaneous mass flux through a surface parallel to the wall must be equal to the amount of mass flux lost to the incoming stream due to steady growth of the laminar boundary layer. In other words, the integral of  $v_p$  over the surface parallel to the wall is zero at all times. At any  $x$ -location the distribution of unsteady mass flux normal to the plate consists of three peaks: a sharp negative peak at the spot leading edge, followed by a large positive peak whose trailing edge decays slowly, and, finally, a weak negative peak at the spot trailing edge. As the spot develops, each of these peaks spreads and the maximum velocity increases. Therefore, the form of the unsteady  $v_p$  vs. time curve, as shown in Figures 4.6-4.9, suggests a multipole source mechanism.

The unsteady mass flux distribution through this surface due to the turbulent spot passage may be modeled as the superposition of four simple time-dependent sources as shown in Figure 5.1. The leading edge consists of two sources of equal strength  $Q_1(t)$  but opposite phase, separated by a distance  $\epsilon = U_\epsilon t_i$ . The trailing edge consists of two weaker sources of strength  $Q_2(t)$  similarly arranged. Thus, the spot appears to be the sum of two unequal dipoles of opposite phase. The leading edge dipole may be further decomposed into two coincident dipoles, one composed of simple sources of strength  $Q_1 - Q_2$  and the other of sources of strength  $Q_2$ . This decomposition allows the spot to be modeled as the sum of a dipole of strength  $\epsilon \partial(Q_1 - Q_2)/\partial t$  and a quadrupole of strength  $\epsilon^2 \partial Q_2/\partial t$ . Because the spot increases in length as

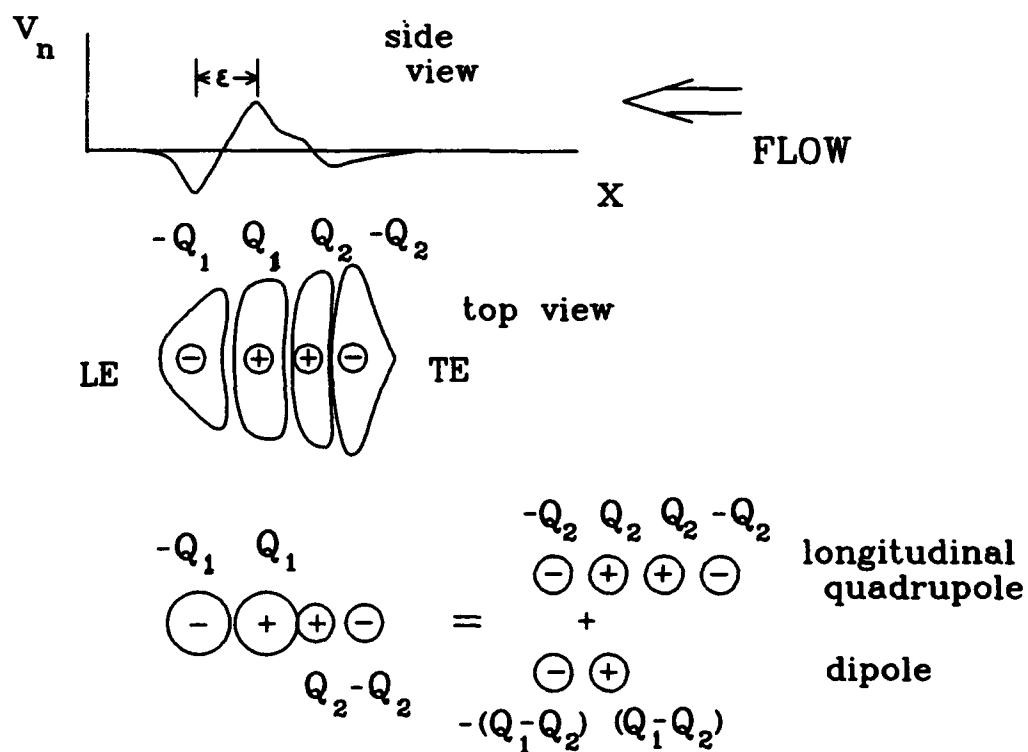


**Figure 5.1** Spatial distribution of instantaneous  $v_n$  due to a turbulent spot on a surface outside the boundary layer and parallel to the wall, and its equivalent multipole source distribution.

it develops, the peaks spread apart. Thus, the source strength will vary not only because  $\partial Q/\partial t$  changes but also because  $\epsilon$  increases.

Having made these qualitative statements about the nature of the acoustic source, the experimental results presented in Chapter 4 may be used in a scaling analysis of Equation 2.6 to give some quantitative estimates of the sound radiation. Before the scaling is carried out, the integral in Equation 2.6 must be rewritten in a way that accounts for the source compactness and for the multipole nature of the source flowfield. If this is not done, a scaling analysis based on the compact form of Equation 2.6 will result in an overestimation of the sound level, since this form of the integral then describes a monopole source, and it has been established that the monopole strength is zero. In order to account for phase differences in the compact source distribution, Equation 2.6 may be expressed as a multipole expansion (see Pierce (1989)):

$$\begin{aligned}
 p(r,t) = \frac{\rho}{2\pi r} \left\{ \int_S \left[ \frac{\partial v}{\partial t} \right] dS' + \frac{\beta_i}{c} \int_S \left[ \frac{\partial}{\partial t} \left( \epsilon \frac{\partial v}{\partial t} \right) \right] dS' + \right. \\
 \left. + \frac{\beta_i \beta_j}{c^2} \int_S \left[ \frac{\partial^2}{\partial t^2} \left( \epsilon^2 \frac{\partial v}{\partial t} \right) \right] dS' \right\} + O(\epsilon^3)
 \end{aligned}
 \tag{5.1}$$

where  $[ ]$  denotes that the argument is evaluated at the retarded time  $t-r/c$  and  $\beta_i$  is a directivity factor. As discussed above, the first term describing monopole-type radiation is zero.

Using the following scaling:

$$v \sim \frac{\Delta \delta}{t_i}, \quad \frac{\partial}{\partial t} \sim \frac{1}{t_i}, \quad \epsilon \sim U_c t_i, \quad \int \int dS' \sim U_c^2 t_i^2 \quad (5.2)$$

the dipole radiation pressure  $p_d$ , source strength  $D$ , and radiated power  $\mathcal{P}_d$  scale as:

$$p_d \sim \frac{\rho U_c^2 \beta_i}{r} M \Delta \delta, \quad D \sim \rho M \frac{\Delta \delta}{t_i^2} \quad (5.3)$$

$$\mathcal{P}_d \sim \rho U_c^3 M^3 \Delta \delta^2$$

The quadrupole radiation  $p_Q$ , source strength  $q$ , and radiated power  $\mathcal{P}_Q$  scale as:

$$p_Q \sim \frac{\rho U_c^2 \beta_i \beta_j}{r} M^2 \Delta \delta^2 \sim \beta_j M p_d, \quad q \sim M D \quad (5.4)$$

$$\mathcal{P}_Q \sim M^2 \mathcal{P}_d$$

The relative powers of Mach number indicate that the quadrupole radiation from a turbulent spot is negligible compared to the dipole radiation at low Mach numbers. From this scaling argument it can be concluded that the sound radiation from the large-scale motion in a turbulent spot is dominated by the dipole associated with the positive peak of the mass flux deficit distribution.

It should be pointed out that using the spot size as a length scale is equivalent to assuming that  $v_p$  is correlated over the spot. This assumption is justified by reference to the ensemble-averaged measurements of  $v_p$ , which show a coherent velocity pattern over the spot. It was previously shown by Van Atta *et al.* (1982) that

the fluctuations in the potential flow velocity are repeatable and nonturbulent, suggesting that the ensemble average merely filters out noise associated with the measurement, rather than averaging out turbulent fluctuations.

Using the experimental results presented above, the streamwise variation of the radiated sound level may be deduced. Figure 5.2 shows the variation of  $D$  and  $p_d$  with  $x$ . Because  $D$  is proportional to  $1/t_i^2$  the dipole source strength per unit area is higher in the early stages of the spot development. The maximum is not at the furthest upstream station, however. This effect is due to the low amplitude of the fluctuation in the mass flux deficit at the upstream stations. Because the source area  $A_{\text{source}}$  is proportional to  $U_c^2 t_i^2$  the dependence of  $p_d$  on  $t_i$  cancels and the streamwise variation in radiated sound depends entirely on the growth in  $\Delta\text{MFD}/\rho U$  with  $x$ . The transition noise calculations of Lauchle (1981) and Audet *et al.* (1989) did not include the streamwise variation in either  $T$  or the peak value of  $\Delta\text{MFD}/\rho U$ .

## 5.2 INTERMITTENCY-WEIGHTING OF DISPLACEMENT THICKNESS

The form of the measured  $\text{MFD}/\rho U$  differs somewhat from that assumed by Lauchle (1981) as indicated by Figure 5.3. First, the measured level within the spot is not constant. Second,  $\Delta\text{MFD}/\rho U$  takes on negative values in the portions of the spot which arrive last at the measurement location. This second difference is the most important, since it reflects the principle of conservation of mass. Because the source flow is incompressible, the net mass flux through  $S_0$  at any instant is identically zero. For the assumed behavior, the growth of the spot will result in the leading and trailing

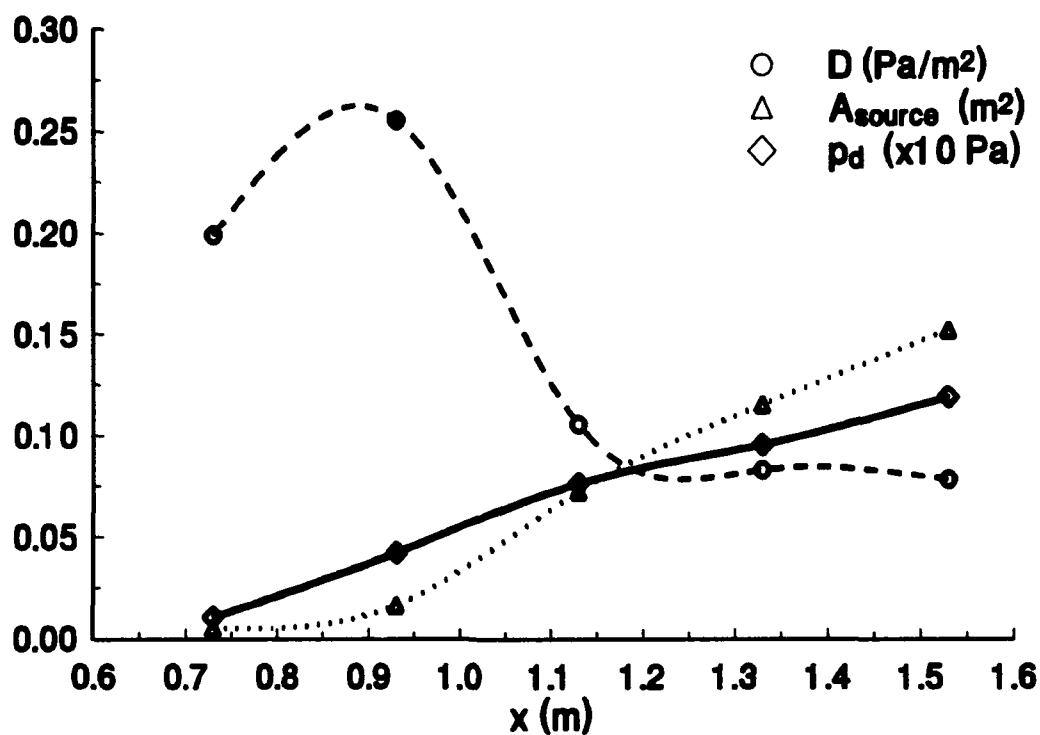


**Figure 5.2** Order of magnitude estimates of the radiated pressure,  $p_d$ , source area,  $A_{\text{source}}$ , and dipole strength per unit area,  $D$ , from an isolated turbulent spot, vs. streamwise coordinate for  $U=0.406$  m/s.



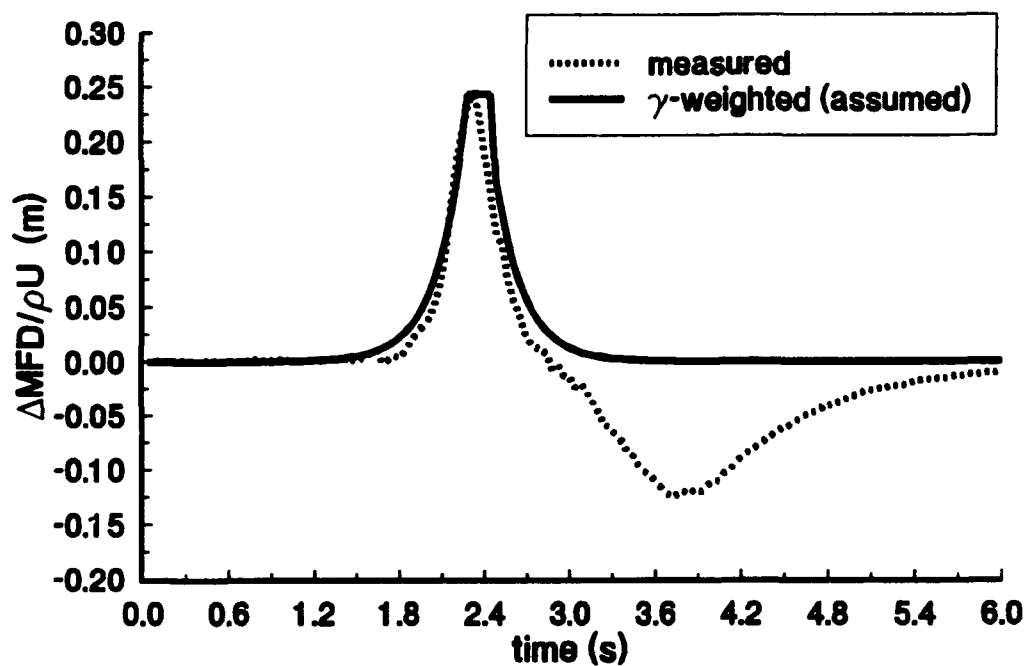


**Figure 5.3** Comparison of measured  $MFD/\rho U_\infty$  and intermittency-weighted  $\delta^*(t)$  assumed by Lauchle (1981). Assumed form models only positive peak associated with dominant dipole source.

edges of the bulge in  $\delta^*(x,t)$  spreading apart. This effect, coupled with the growth in the magnitude in  $\Delta\delta^*$  with  $x$ , which both Lauchle (1981, 1989) and Audet *et al.* (1989a, b) neglected, indicates that the volume bounded by the solid wall and the surface  $y = \delta^*(x,z,t)$  is growing slowly with time. This cannot occur if mass is to be conserved in the flow. If  $\Delta\delta^*(x,z,t)$  and, hence,  $\Delta MFD/\rho U$  has a positive peak at one location, it must also have a negative peak somewhere else, so that the volume bounded by  $y = 0$  and  $y = \delta^*$  is constant. From a hydrodynamic perspective the present measurements do not support using the intermittency-weighted form for the displacement thickness. On the other hand, the assumption that the displacement thickness may be modeled in this way is valid for describing the highest-order acoustic source mechanism. The dominant dipole source is associated with the positive mass flux deficit peak, which is approximated by the intermittency-weighted form. However, the quadrupole source is not modeled under this assumption.

### 5.3 NOISE FROM A NATURAL BOUNDARY LAYER TRANSITION

This study bases its conclusions on the behavior of single artificially generated turbulent spots, both in insolation and in tandem. In a naturally occurring transition region the flow is made up of spots which appear at random at the upstream end of the transition zone, grow as they convect downstream, and eventually merge to form a low Reynolds number turbulent boundary layer. The effects of spot interaction on spot growth have only been partially considered, and the nature of spot formation has been ignored entirely.

It appears that the degree of interaction represented by the experiments described here does not modify the convection speed, the rise time, or the mass flux deficit fluctuation peak amplitudes significantly. This result suggests that these differences do not modify substantially the order of magnitude estimates of the sound level from an isolated turbulent spot. In addition, Zilbermann *et al.* (1977) showed that a turbulent spot retains its identity well past the location where it enters a turbulent environment. The data on interacting spots presented here shows that for a weak interaction, the potential flow fluctuations outside the spot are not notably attenuated from those observed in the isolated spot case. If the statements "the spot retains its identity" and "the potential flow fluctuations are not seriously modified" can be seen as equivalent, then the effect of spot interaction on the level of sound radiated from the mature regions of the transition zone is small indeed. The isolated turbulent spot measurements, interpreted in the light of the acoustic source model, show that the fluid motion responsible for the dipole source corresponds to the portion of the turbulent spot which protrudes above the surrounding laminar boundary layer. The structure which Zilberman *et al.* (1977) showed to persist well into a tripped turbulent boundary layer corresponds exactly to this structure. It may be that the early stages of the fully turbulent layer generate sound according to the mechanism described here, until the point where the large-scale structure of the outer flow which is due to the persistence of turbulent spots has decayed. Further experimentation should clarify the extent to which this statement is correct.

To estimate the sound radiation from a natural transition zone from the radiation characteristics of a single turbulent spot requires 1) the radiation from a spot as a function of location in the transition zone and 2) the local spot density, *i.e.*, how many spots there are per unit area, again as a function of location. The extrapolation of the isolated spot results to natural transition makes use of the following assumptions:

1. The single spot radiation characteristics are well-modeled by the isolated spot estimate given above. The turbulent spot radiation, then, retains its dipole character throughout the transition zone. This assumption alone indicates that the transition region should be a more efficient sound radiator than the fully turbulent boundary layer, which radiates as a quadrupole (Powell, 1960; Hardin, 1991).
2. The longitudinal coordinate in the isolated spot result may be replaced by  $\zeta = (x - x_0)/\Delta x$ , where  $x_0$  is the location of the upstream edge of the transition zone and  $\Delta x$  is the transition zone length given by Equation 4.7. Note that this results in the isolated spot radiation being given for a range of  $0.26 < \zeta < 1.30$ , extending beyond the end of the hypothetical transition zone.
3. The local acoustic source strength is the local single spot radiation weighted by the local spot density, *i.e.*,  $p_r(x) \sim p_d(x) \hat{N}(x)$ , where  $p_d(x)$  is the local dipole strength per spot and  $\hat{N}(x) \sim N/U$  is the local number

of spots per unit length.  $N(x)$  is the local spot rate found by Farabee, *et al.* (1974) and used by Lauchle (1981) and Audet *et al.* (1989a, 1989b) in their calculations:

$$N(\xi) = 1.272 \left( \frac{U}{\Delta x} \right) \xi e^{-(4.185 \xi)} \quad (5.6)$$

As shown in Figure 5.4, the spot rate,  $N$ , rises from zero at the upstream end of the transition zone to a maximum at about 30% of the transition zone length (see Lauchle, 1980), and then back to zero again. The total radiated pressure at any instant is the integral of  $p_d(x) \hat{N}(x)$  over the transition zone. Weighting the radiated pressure from a single spot shown in Figure 5.2 with this distribution will result in a maximum located near of the midpoint of the transition zone, as shown in Figure 5.4. The model of the acoustic contribution to the wall-pressure used by Audet *et al.* (1989a, 1989b) did not consider the streamwise variation in  $\Delta MFD/\rho U$  and predicted the location of the maximum acoustic contribution to be located at  $\xi = 0.5$ . The streamwise distribution of local radiated sound pressure is also shown in Figure 5.4. Here, the estimate is based on the scaling analysis presented above, with  $p_d(x)$  given by the curve shown in Figure 5.2.

Qualitatively, the shape of the streamwise variation of the acoustic pressure fluctuation given by Audet *et al.* (1989a, b) is confirmed by weighting the single spot radiation result with the number of spots per unit length. This statement may be made more precise when the effect of spot interaction upon the streamwise variation in radiated sound pressure is better understood. In any case, this argument based on the

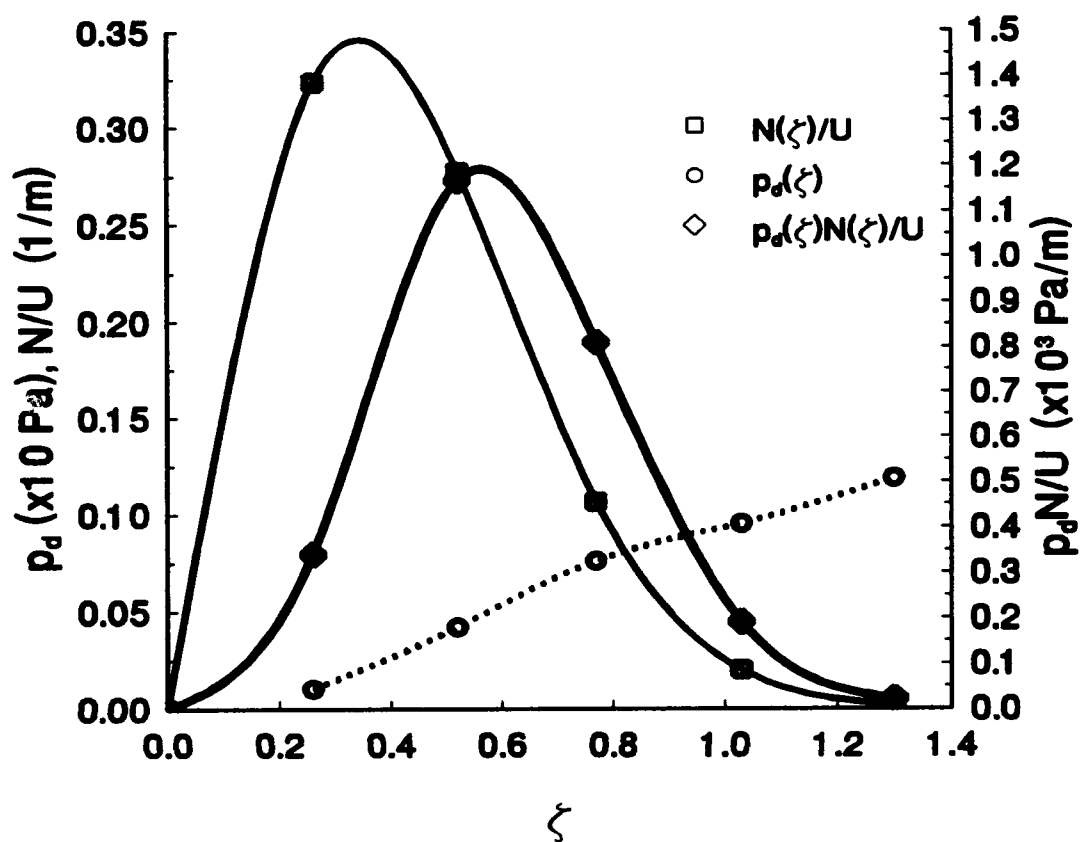


**Figure 5.4** Extrapolation of single spot radiation estimate to natural transition zone. Local acoustic source strength is proportional to the product of the local spot source strength, weighted by the local spot density.

single spot behavior does indicate that the streamwise variation in the rms acoustic pressure shown by Audet *et al.* (1989) is largely due to the spatial distribution of the spot rate. However, this conclusion is tentative at this time because the assumptions which have led to it are still largely unproven, especially the assumption that the local single spot radiation remains dipole-like throughout the transition zone.

## **CHAPTER 6**

### **CONCLUSIONS**

Measurements of the velocity field of a single, isolated turbulent spot were made in order to obtain an estimate of the ensemble-averaged, unsteady local fluctuation in the mass flux deficit, and, in turn, the fluctuation in the mass flux normal to the wall. These fluctuations have been characterized by the times for the mass flux deficit to rise to its maximum, and then fall to its minimum. In addition, the streamwise variations in these fluctuations were also deduced. The measured mass flux deficit was also compared to the form assumed in previous analyses of transition noise. The component of velocity normal to the wall in the freestream, above the maximum turbulent spot height, was also measured to understand the streamwise and spanwise development of this quantity. Similar measurements of turbulent spot pairs were carried out to investigate how their interaction modifies the observed isolated spot results. The behavior of the normal velocity above the turbulent spot was used to construct a simple source acoustic model for the turbulent spot. An estimate of the sound radiation from an isolated turbulent spot was obtained using a scaling analysis employing the simple source model and the scales of motion deduced from the experimental results.

#### **6.1 DISCUSSION**

The mass flux deficit was calculated from measured ensemble-averaged, unsteady velocity profiles. The shape of the unsteady mass flux deficit time series



(see Figure 4.3) may be explained as follows. The positive peak occurs at the same location as the maximum height of the turbulent spot which is greater than the height of the surrounding laminar boundary layer. At this location the averaged velocity profile is identical to a turbulent boundary layer. This structure causes the part of the flow which is initially above the laminar boundary layer to decelerate, then accelerate, as the turbulent spot maximum height passes by, after which the height of the turbulent spot decreases, causing a decrease in the mass flux deficit. The minimum of the mass flux deficit corresponds to the trailing edge of the turbulent portion of the turbulent spot. At this point the height of the turbulent spot is equal to that of the surrounding laminar boundary layer. Because the velocity profile is "fuller" than the undisturbed laminar profile, the mass flux deficit is actually less than that of the undisturbed flow. The integral of the mass flux deficit over the area of the wall at any instant is zero, indicating that the net mass flux normal to the wall is also zero at any instant. The convection speeds of the positive and negative peaks of the mass flux deficit fluctuation were in good agreement with other investigators' measurements of the convection speeds of the spot maximum spot height and trailing edge, respectively. The convection speed of the positive maximum, 76% of the freestream, also corresponds well with other measurements of the overall turbulent spot convection speed. This quantity serves as a velocity scale for the flow and is useful for the acoustic analysis. A length scale for the flow was obtained from the positive peak amplitude of the mass flux deficit.

The time scale characterizing the change between the fully laminar and fully turbulent flow was estimated by the difference either in the times of arrival of the leading edge and positive mass flux deficit peak (the rise time), or in the times of arrival of the positive peak and the negative peak (the fall time). Comparison of the nondimensionalized estimates of this quantity at one velocity (40.6 cm/s) to a single estimate obtained from one velocity profile at a lower velocity (19 cm/s) suggests that the rise time is independent of Reynolds number, while the fall time is not. This conclusion finds support in the results of Wygnanski *et al.* (1982), which states that the leading edge and maximum spot height convection speeds are independent of Reynolds number, while the trailing edge convection speed increases as Reynolds number decreases.

The spatial distribution of the velocity fluctuation normal to the wall in the potential flow, found by direct measurement, shows that the velocity peaks are in phase across the width of the turbulent spot, and that as the spot grows each peak increases in length, width, and height, so that for each peak the mass flux normal to the wall increases with time.

The mass flux through a surface parallel to the wall, above the maximum turbulent spot height, serves as the boundary condition for the acoustic wave equation, according to the Liepmann Analogy. Considering the mass flux through each peak to be an unsteady mass source or sink, the turbulent spot may be described as a distribution of simple sources. Because of the low Mach number of the flow, this distribution of sources may be considered compact since the size of a turbulent spot

is much smaller than the wavelengths of the sound produced by the flow. The relative magnitudes of the mass flux for each of the peaks resulted in a simple source distribution which could be described as the superposition of a longitudinal quadrupole and a dipole. The axes of both these sources are aligned with the freestream. The dipole is associated with the large, positive mass flux deficit peak. The solution to the acoustic equation given by Liepmann (1954) was approximated by a multipole expansion so that the order of magnitude of the contribution of each integral in the expansion to the total radiated sound could be determined. The variation in the source strength with streamwise distance was determined by substituting the scales found experimentally into the multipole expansion. These results show that the dipole contribution dominates. The dipole strength per unit area scales as  $(\Delta MFD/\rho U)/\xi^2$ , while the dipole strength scales as  $\Delta MFD/\rho U$ . The acoustic source is more efficient in the early stages of the turbulent spot's development because of the  $1/\xi^2$  behavior, but the total radiated sound power is less because the size of the turbulent spot is small at this point in its development. The dipole strength per unit area decreases as the spot grows, but the total radiated sound power increases due to the compensating effect of the increased size of the source.

In previous analysis of the sound generated by boundary layer transition, Lauchle (1981) and Lagier and Sornette (1984) assumed that flow quantities could be described by an intermittency-weighted form. Lauchle's treatment of the displacement thickness was evaluated using the measured behavior of the mass flux deficit. It was found that the positive peak was adequately represented by this model but the negative

peak was not, so that the assumed form could not be said to model the hydrodynamic fluctuations accurately. However, the dominant acoustic behavior was associated with the motion which gave rise to the positive mass flux deficit peak, so that the intermittency-weighting assumption could be seen to represent the part of the flow which contributes the dominant part of the sound radiation.

The effect of turbulent spot interaction on these results was studied by measuring velocity profiles of two turbulent spots generated at the same location with a fixed time delay, so that the second spot leading edge passes through the calming region of first spot and overtakes the trailing edge of the first spot. This interaction scenario was studied briefly by Gutmark and Blackwelder (1987), who showed that for a sufficiently small time delay, the convection velocity of the second spot leading edge was reduced. The growth of the leading edge of the second turbulent spot, which occurs by destabilization of the surrounding laminar flow, is attenuated because the velocity profile is fuller, and therefore more stable in the calming region. While the present study shows a significant modification of the overhang region, the convection velocities of the second turbulent spot were not modified to any significant degree. Furthermore, the motions associated with the mass flux deficit positive peak were also not modified. This suggests that up to the level of interaction investigated the turbulent spot may still be modeled as a dipole source. It may be concluded that the intermittent region of the boundary layer generates sound more efficiently than the fully turbulent region when the separation between turbulent spots is large enough that

the large positive mass flux deficit peak at the spot maximum height still exists. The level of interaction for which this behavior persists has yet to be established.

An extension of the isolated turbulent spot results to a natural transition zone was carried out using two simple assumptions: (1) the effect of turbulent spot interaction on the large-scale behavior of individual spots is negligible, and (2) the local dipole source strength is proportional to the product of the isolated turbulent spot source strength and the local turbulent spot density. When the source strength was scaled in this way it exhibited qualitatively the same behavior as that shown by the model of Audet *et al.* (1989), peaking near the midpoint of the transition zone.

## 6.2 SUMMARY

The conclusions of this study are as follows:

1. The range of the nondimensionalized rise time for the isolated turbulent spot was found to be  $0.06 < T < 0.30$  while the nondimensionalized fall time spanned a range  $0.13 < T < 0.74$ . These values confirm the lower range of limits set on this parameter by Lauchle (1981).
2. The time scales describing the local rate of change of the streamwise mass flux deficit increase with distance from the generation point.
3. The streamwise spatial growth rate of the peak amplitudes of the mass flux deficit decreases with distance from the generation point.
4. The peak amplitudes of the normal component of velocity increases with distance from the generation point, but levels off.

5. The results from the isolated spot case were not significantly modified by weak interaction between two turbulent spots in the case observed.
6. The acoustic source due to the large-scale fluctuation in the turbulent spot flowfield may be modeled as the superposition of a dipole associated with the positive mass flux deficit peak and a longitudinal quadrupole.
7. The form of the unsteady displacement thickness assumed by Lauchle (1981) is invalid from a hydrodynamic point of view but adequately models the dominant dipole acoustic source.
8. Extrapolation of the isolated spot sound estimate to a natural transition flow suggests that the sound source strength reaches its maximum near the midpoint of the transition zone and that the entire transition zone radiates as a dipole source. It may be concluded from the last assertion that the natural transition zone is a more efficient radiation source than the fully turbulent boundary layer, which radiates as a quadrupole.

### **6.3 SUGGESTIONS FOR FURTHER WORK**

The present study was motivated by the need to explain how the transition region of a boundary layer generates sound more efficiently than does the fully turbulent region. The focus of the present work was the behavior of an isolated turbulent spot, the cause of the intermittent nature of transitional flow. The results presented are for an isolated turbulent spot and for a weakly interacting turbulent spot pair. Ensuring the generality of these results requires additional information

concerning the effects of further merging on individual turbulent spot structure and how dependent the flow scales deduced from these measurements are on the Reynolds number. In addition, the present results are in some sense limited because they are based on many realizations of point measurements taken over a long period of time. This suggests recourse to more advanced full-field measurement techniques. Finally, there is a need for direct measurement of the sound produced by both isolated turbulent spots and a natural transition flow.

The dominant sound production mechanism in a turbulent spot is the dipole associated with the mass flux deficit positive peak. The extent to which turbulent spot interaction changes this behavior from that observed in an isolated turbulent spot is important for generalizing the single turbulent spot sound source model to a natural transition flow. If the qualitative behavior of the positive mass flux deficit peak is not significantly altered, then it appears that the dominant sound source in a natural transition flow may indeed be seen as a distribution of dipoles. Experiments to test the extent to which this is true should begin by repeating the interacting turbulent spot measurements presented above for shorter time delays between the generation of each spot. The extent to which the identity of a turbulent spot may remain distinct after entering a fully turbulent environment, shown by Zilberman *et al.* (1977), should also be examined with the aim of detecting differences in the unsteady mass flux deficit as the turbulent spot passes by. These measurements would be greatly improved if a single realization of the velocity profile could be obtained simultaneously, rather than one point at a time, as in the present measurements. This requirement should lead to

the use of either rakes of hot wires or hot films, or the use of whole-field imaging techniques such as hydrogen bubble visualization or Particle Image Velocimetry. The apparent weak dependence of the nondimensionalized rise time and the apparent strong dependence of the nondimensionalized fall time on the Reynolds number should be investigated more thoroughly. This may be done by measuring velocity profiles as was done in the present study at different freestream velocities, or with a different generation point location.

An important contribution to the study of transition noise would be the direct measurement of the sound generated by the intermittent flow. This study could start with measurements of acoustic intensity conditioned on the detection of the presence of an isolated turbulent spot. These experiments, carried out over a range of freestream velocities, would provide a test of the results of the scaling analysis presented here. Once the clear relationship between the unit of intermittency (a single turbulent spot) and the radiated sound has been established, then measurements of interacting spots and a naturally occurring transition zone should be carried out. A study along these lines is currently being carried out in an anechoic facility at the Applied Research Laboratory.



## REFERENCES

Antonia, R.A., Chambers, A.J., Sokolov, M., and Van Atta, C. W., 1981, "Simultaneous Temperature and Velocity Measurements in the Plane of Symmetry of a Turbulent Spot," *J. Fluid Mechanics*, Vol. 108, pp. 317-343.

Audet, J. Dufourcq, Ph., and Lagier, M., 1989a, "Pression Parietale Sous Une Couche Limite Lors de la Transition vers la Turbulence," *J. Acoustique*, Vol. 2, pp. 369-378.

Audet, J., Dufourcq, Ph., Lagier, M., and Sornette, D., 1989b, "Wall Pressure Fluctuations in the Intermittent Regime of a Transition Boundary Layer: Comparison Between Theory and Experiment," *Flow-Induced Noise Due to Laminar-Turbulent Transition Process*, Farabee, T.M., Hansen, R.J., and Keltie, R.F. (eds), ASME NCA-5, pp. 25-30.

Bruneau, S.D., 1992, Digital Image Processing of Hydrogen Bubble Lines for Instantaneous Velocity Profiles, M.S. Thesis, Department of Aerospace Engineering, The Pennsylvania State University.

Cantwell, B., Coles, D., and Dimotakis, P., 1978, "Structure and Entrainment in the Plane of Symmetry of a Turbulent Spot," *J. Fluid Mechanics*, Vol. 87, pp. 641-672.

Coles, D., and Barker, S.J., 1975, "Some Remarks on a Synthetic Turbulent Boundary Layer," *Turbulent Mixing in Nonreactive and Reactive Flows*, Murthy, S.N.B. (ed), Plenum, pp. 285-292.

Charters, A.C., 1943, "Transition between Laminar and Turbulent Flow by Transverse Contamination," NACA Tech. Note No. 891.

Crighton, D.G., 1975, "Basic Principles of Aerodynamic Noise Generation," *Prog. Aerospace Sciences*, Vol. 16, pp. 31-96.

Curle, N., 1955, "The influence of solid boundaries upon aerodynamic sound," *Proc. Roy. Soc., A* 231, pp. 505-514.

Dhawan, S., and Narasimha, R., 1958, "Some Properties of Boundary Layer Flow During the Transition from Laminar to Turbulent Motion," *J. Fluid Mechanics*, Vol. 3, pp. 418-436.

Farabee, T.M., Casarella, M.J., DeMetz, F.C., 1974, "Source Distribution of Turbulent Bursts During Natural Transition," David Taylor Naval Ship Research and Development Center Report SAD-89E-1942.

Feil, O.G., 1964, "Vane Systems for Very-Wide-Angle Subsonic Diffusers," *J. Basic Engr.*, Vol. 86, pp. 759-764.

Gad-el-Hak, M., Blackwelder, R.F., and Riley, J.J., 1985, "On the Growth of Turbulent Regions in Laminar Boundary Layers," *J. Fluid Mechanics*, Vol. 110, pp. 73-95.

Gutmark, E., and Blackwelder, R.F., 1987, "On the Structure of a Turbulent Spot in a Heated Boundary Layer," *Experiments in Fluids*, Vol. 5, pp. 217-229.

Hardin, J.C., 1991, "Acoustic Sources in the Low Mach Number Turbulent Boundary Layer," *J. Acoustical Soc. America*, Vol. 90, pp. 1020-1031.

Itsweire, E.C., and Van Atta, C.W., 1983, "The Effects of Different Similarity Transformations on Mean Particle Paths in Turbulent Spots," *J. Physique -- Lettres*, pp. L-917 - L-923.

Japikse, D., 1984, "Turbomachinery Diffuser Design Technology," Report DTS-1, Concepts ETI, Inc., 1984.

Josserand, M.A., and Lauchle, G.C., 1990, "Modeling the Wavevector-Frequency Spectrum of Boundary-Layer Wall Pressure During Transition on a Flat Plate," *ASME J. Vibration and Acoustics*, Vol. 112, pp. 523-534.

Karamcheti, K., 1966, *Principles of Ideal-Fluid Aerodynamics*, John Wiley and Sons, New York, p.496.

Lagier, M., and Sornette, D., 1986, "A Two-Fluids Model of the Acoustic Noise Radiated by Intermittent Flows," *Acustica*, Vol. 61, pp. 116-124.

Lauchle, G.C., 1980, "On the radiated noise due to boundary-layer transition," *J. of Acoustical soc. Am.*, Vol. 67, pp. 158-168.

Lauchle, G.C., 1981, "Transition Noise -- the Role of Fluctuating Displacement Thickness," *J. Acoustical Soc. America*, Vol. 69, pp. 665-671.

Lauchle, G.C., 1989, "Transition as a Source of Radiated Noise and Vibration," *Flow-Induced Noise Due to Laminar-Turbulent Transition Process*, Farabee, T.M., Hansen, R.J., and Keltie, R.F. (eds), ASME NCA-5, pp. 31-38.

Lauchle, G.C., 1991, "Hydroacoustics of transitional boundary layer flow," *Applied Mechanics Rev.*, Vol. 44, No. 12, pp. 517-531.

Laufer, J., Ffowcs-Williams, J.E., Childress, S., 1964, "Mechanism of Noise Generation in the Turbulent Boundary Layer," AGARDograph 90.

Libby, P.A., 1975, "On the Prediction of Intermittent Turbulent Flows," *J. Fluid Mechanics*, Vol. 68, pp. 273-295.

Liepmann, H.W., 1954, "On the Acoustic Radiation From Boundary Layers and Jets," Guggenheim Aeronautics Laboratory, California Institute of Technology, Pasadena, CA.

Liepmann, H.W., Roshko, A., 1957, *Elements of Gas Dynamics*, John Wiley and Sons, New York.

Lighthill, M.J., 1952, "On Sound Generated Aerodynamically. I. General Theory," A211, pp.564-587.

Lighthill, M.J., 1954, "On sound generated aerodynamically, II: Turbulence as a source of sound," *Proc. Roy. Soc. A* 222, pp. 1-32.

Lighthill, M.J., 1958, "On Displacement Thickness," *J. Fluid Mechanics*, Vol. 4, pp. 383-392.

Maestrello, L., 1965, *J. Sound and Vibration*, Vol. 2, pp. 270-292.

Maestrello, L., 1967, *J. Sound and Vibration*, Vol. 5, pp. 407-448.

Matsui, T., 1980, "Visualization of Turbulent Spots in the Boundary Layer along a Flat Plate in a Water Flow," *Laminar-Turbulent Transition*, Eppler, R., and Fasel, H. (eds), Springer, pp. 288-296.

Motohashi, T., Blackwelder, R.F., 1983, "Decreasing the Side Wall Contamination in Wind Tunnels," *ASME J. Fluids Engr.*, Vol. 105, pp. 435-438.

Narasimha, R., Devasia, K.J., Gururani, G., and Badri Narayanan, M.A., 1984, "Transitional Intermittency in Boundary Layers Subjected to Pressure Gradient," *Experiments in Fluids*, Vol. 2, pp. 171-176.

Perraud, J.C., 1989, "Studies of Laminar-Turbulent Transition in Air and Water Wall Pressure Fluctuations and Acoustic Emission From the Turbulent Intermittency," in *Flow-Induced Noise Due to Laminar-Turbulent Transition Process*, Farabee, T.M., Hansen, R.J., and Keltie, R.F. (eds), ASME NCA-5, pp. 17-24.

Perry, A.E., Lim, T.T., and Teh, E.W., 1981, "A Visual Study of Turbulent Spots," *J. Fluid Mechanics*, Vol. 104, pp. 387-405.

Phillips, O.M., 1955, "On the aerodynamic surface sound from a plane turbulent boundary layer," *Proc. Roy. Soc. A* 234, pp. 327-335.

Pierce, A.D., 1989, *Acoustics: An Introduction to Its Physical Principles and Applications*, Acoustical Society of America, pp. 169-171.

Powell, A., 1960, "Aerodynamic Noise and the Plane Boundary," *J. Acoustical Soc. America*, Vol. 32, pp. 982-990.

Powell, A., 1990, "Some Aspects of Aeroacoustics: From Rayleigh Until Today," *ASME J. Vibration and Acoustics*, Vol. 112, pp. 145-159.

Sankaran, R., Antonia, R.A., Bisset, D.K., Sokolov, M., 1991, "Flow Patterns and Organization Within Turbulent Spots," *Phys Fluids A*, pp. 1560.

Schubauer, G.B., and Klebanoff, P.S., 1955, "Contributions to the Mechanics of Boundary Layer Transition," NACA TN 3489.

Sornette, D., Lagier, M., 1984a, "Nature monopolaire du rayonnement acoustique engendré par les écoulements instables," *Acustica*, Vol. 55, pp. 255-267.

Sornette, D., Lagier, M., 1984b, "Acoustic Noise Radiated by Transient Flows," *Acoust. Ltrs.*, Vol. 7, pp.104-108.

Tam, C.K.W., 1975, "Intensity, spectrum, and directivity of turbulent boundary layer noise," *J. Acoustical Soc. America*, Vol. 57, pp. 25-34.

Van Atta, C.W., and Helland, K.N., 1981, "Exploratory Temperature-Tagging Measurements of Turbulent Spots in a Heated Laminar Boundary Layer," *J. Fluid Mechanics*, Vol. 100, pp. 243-255.

Van Atta, C.W., Sokolov, M., Antonia, R.A., and Chambers, A.J., 1982, "Potential Flow Signature of a Turbulent Spot," *Physics of Fluids*, Vol. 25, pp. 424-428.

Wynanski, I., Sokolov, M., and Friedmann, D., 1976, "On a Turbulent 'Spot' in a Laminar Boundary Layer," *J. Fluid Mechanics*, Vol. 78, pp. 785-819.

Wynanski, I., Zilberman, M., and Haritonidis, J.H., 1982, "On the Spreading of a Turbulent Spot in the Absence of a Pressure Gradient," *J. Fluid Mechanics*, Vol. 123, pp. 69-90.

Zilbermann, M., Wynanski, I., Kaplan, R.E., 1977, "Transitional Boundary Layer Spot in a Fully Turbulent Environment," *Phys. Fluids*, Vol. 20, p.S258.